universität wien

DISSERTATION

Titel der Dissertation

Mechanism of asymmetric PIE-1 segregation in *C. elegans* one-cell embryo

angestrebter akademischer Grad

Doktor/in der Naturwissenschaften (Dr. rer.nat.)

Verfasserin / Verfasser:	Anne Göppert
Matrikel-Nummer:	0748788
Dissertationsgebiet (lt. Studienblatt):	Molekulare Biologie
Betreuerin / Betreuer:	Carrie Cowan, PhD

Wien, am 28. April 2010

Acknowledgements

First of all, I would like to thank my supervisor Carrie. This thesis would not have been possible without her support, guidance and encouragement.

I would like to thank Monica Gotta, Jürgen Knoblich and Verena Jantsch for the time and work they put into evaluating my thesis.

I would like to acknowledge Malte Wachsmuth and Katrin Heinze for sharing their expertise, and their assistance on FCS.

A special thanks goes to the past and present members of the Cowan lab for discussions and help. I will miss our laughs.

I am thankful to Becky, Evi, Callum, Harvey and my family for their endless patience, distractions and continuous motivation.

Abstract

The transcriptional repressor PIE-1 is a fate determinant essential for the correct development of germline stem cells in *C. elegans*. During the asymmetric cell divisions of early embryos, PIE-1 must be localised asymmetrically in order to be restricted to the germline lineage. PIE-1 functions in the nucleus and cytoplasmic RNA–protein aggregates called P granules. The localisation of PIE-1 to these compartments is thought to reflect its cytoplasmic localisation. PIE-1 mRNA is reported to be uniformly distributed in early embryos, suggesting that PIE-1 localisation is controlled at the protein level.

Using a combination of time-lapse imaging, optical manipulations and genetics, I have investigated how PIE-1 is segregated to the germline lineage in one-cell embryos. I found that PIE-1 exhibits an exponential concentration gradient with its source at the posterior cortex. PIE-1 stability and/or production depend on the posterior cortical component PAR-1. The PIE-1 gradient is initiated at polarity establishment and stabilises over a period of approximately 6 minutes. Partial depletion of PIE-1 does not affect gradient shape, consistent with a diffusion-based mechanism, but affect P granule association suggesting that PIE-1 concentration may limit its aggregation.

Analysis of the PIE-1 gradient in embryos depleted of other germline fate determinants showed a correlation between gradient shape, diffusion rates, and P-granule association. These results suggest that PIE-1's association with P granules may contribute to gradient stability but this is unlikely to provide the sole mechanism of gradient formation. In contrast to P granules, the nuclear localisation of PIE-1 had only a negligible effect on the gradient. Time-lapse imaging of P granules (PGL-1) and the germline factor MEX-1 in embryos depleted of PIE-1 indicated a hierarchy in P granule localisation, such that MEX-1 is required for PIE-1 localisation to P granules but not vice-versa.

In addition to its P granule localisation, MEX-1 exhibits an exponential concentration gradient from the posterior cortex similar to that of PIE-1, suggesting that using a concentration gradient might be a common mechanism for cytoplasmic asymmetry of germline factors. Thus, PIE-1 appears to be restricted to the future germline lineage by a

diffusion-based gradient from the posterior cortex that is shaped by MEX-1-facilitated association with P granules.

Zusammenfassung

Die Zelldifferenzierungsdeterminante PIE-1 bestimmt die Entwicklung und Identität der Keimbahn-Stammzellen in *C. elegans*, in dem die Transkription der Stammzellen inhibiert wird. PIE-1 akkumuliert in den asymmetrischen Zellteilungen auf einer Seite des frühen Embryos. Dieser Prozeß ermöglicht, daß PIE-1 nur an die Keimbahnzellen weitergegeben wird. PIE-1 ist im Nukleus und in zytoplasmatischen mRNA–Protein–Komplexen – so genannten „P granules“ – zu finden. Das Vorhandensein des Proteins in diesen Zellkompartimenten scheint von seiner zytoplasmatischen Lokalisierung bestimmt zu werden. Das spezifische Lokalisierungsmuster von PIE-1 wird möglicherweise auf Proteinebene reguliert, da die Boten-RNA (mRNA) gleichmäßig in frühen Entwicklungsstadien des Embryos verteilt ist.

Die Frage, wie PIE-1 spezifisch an die Keimbahnlinie weitergegeben wird, versuche ich mit einer Kombination aus Zeitrafferaufnahmen, optischen und genetischen Manipulationen zu beantworten. Ich konnte zeigen, daß PIE-1 einen expotentiellen Konzentrationsgradient bildet, wobei sich höchste Proteinkonzentration – die Gradientenquelle – am posterioren Kortex befindet. Deren Proteinstabilität/-produktion hängt vom posterioren Polaritätsprotein PAR-1 ab. Der PIE-1–Gradient entsteht zum Zeitpunkt der beginnenden Polarisierung des Embryos und stabilisiert sich über die folgenden sechs Minuten. Der PIE-1–Gradient entsteht auch nach Verminderung der Proteinmenge, was auf einen diffusionsbasierenden Mechanismus schließen läßt. Jedoch verändert sich das Assoziationsverhalten von PIE-1 an „P granules“. Möglicherweise ist die cytoplasmatische Konzentration an PIE-1–Protein limitierend für diese Assoziation ist.

Mit Hilfe der Analyse des PIE-1–Gradienten in Embryonen, in denen andere Keimbahn-Differenzierungsdeterminanten entfernt wurden, konnte ich einen Zusammenhang zwischen der Form des Gradienten, der Diffusionsgeschwindigkeit und der Bindung an „P granules“ fest stellen. Allerdings scheint die Assoziation von PIE-1 an „P granules“ nicht der einzige Mechanismus zu sein, der zur Stabilität des Gradienten beiträgt.

Im Gegensatz zu den „P granules“ hat die nukleare Lokalisierung von PIE-1 nur einen geringfügigen Effekt auf die Stabilität des Gradienten. Ich konnte eine Hierarchie in der Binding von PIE-1 und MEX-1 an „P granules“ erkennen: Die Zelldifferenzierungsdeterminante MEX-1 wird für die PIE-1–Bindung an „P granules“ benötigt, was allerdings nicht auf die umgekehrte Situation zutrifft. Zusätzlich zur Lokalisierung an „P granules“ zeigt MEX-1 wie PIE-1 einen exponentiellen Konzentrationsgradient mit der höchsten Proteinkonzentration am posterioren Kortex.

Zusammenfassend deuten meine Daten darauf hin, daß PIE-1 mittels eines vom posterioren Kortex ausgehenden, auf Diffusion basierenden Gradienten, ausschließlich an Zellen der Keimbahnline weitergegeben wird. Die von MEX-1 ermöglichte Bindung von PIE-1 and „P granules“ scheint zur Formierung des Gradienten eine entscheidende Rolle zu spielen.

Table of Contents

Table of Figure

1 Introduction

The life of most organisms starts out with a single cell, or zygote. During development, the zygote divides to give rise to a multi-cellular organism consisting of highly diverse cell types, such as muscles, neurons, glands, and immune and blood cells, which carry out different functions. The creation of this wide range of cell types is facilitated by asymmetric cell division, resulting in two daughter cells that pursuit different cell fates and functions. The self-renewal of stem cells follows the same asymmetric cell division process: one daughter cell maintains its stem cell-like characteristics while the other differentiates.

1.1 Asymmetric Cell Division

It is established that two basic mechanisms result in cellular diversity: extrinsic and intrinsic cell fate determination. Using the extrinsic mechanism, the cell divides symmetrically to give rise to two identical daughter cells. Subsequently, one of the newly formed daughter cells receives an environmental signal that makes the cell take on a different cell fate than the sister. Cells using the intrinsic mechanism establish asymmetry prior to division and divide according to this asymmetry. Cells undergoing asymmetric cell division segregate fate determinants according to an internal polarity axis. The asymmetric inheritance of these determinants dictates the different cell fates of the two daughter cells (Betschinger and Knoblich, 2004).

The nature of asymmetry in cell division is diverse; for example, the size of the daughter cell in the budding yeast *Saccharomyces cervisiae* is significantly smaller than of the mother cell. An even more extreme example of physical asymmetry can be observed during oocyte maturation of *Caenorhabititis elegans*: The reduction of the number of chromosomes in meiosis results in the oocyte and minute polar bodies (Oegema and Hyman, 2006). On the other hand, cells using the intrinsic mechanism demonstrate functional differences in the resulting daughter cells, by inheritance. In neuroblasts, the neuronal stem cell in the *Drosophila melanogaster* larval brain, inheritance of the cell fate determinant Numb, maintains the identity of one of the daughter cells. The other daughter cell, which is the

ganglion mother cell, terminates its differentiation after one additional cell division into neurons and glial cells (Gönczy, 2008).

The polarity, which sets the axis for the asymmetric segregation of the cell fate determinates, is defined by a set of highly conserved proteins; the PAR proteins. These proteins were discovered in a screen for abnormal early development in the roundworm *C. elegans* (Kemphues et al., 1988).

1.2 Caenorhabititis elegans

The soil nematode *C. elegans* is an excellent model system to study asymmetric cell division. In the early embryo, a series of five asymmetric divisions creates the six founder cells: AB, MS, E, C, D, and P_4, which give rise to all the cell lineages of a worm (Sulston et al., 1983). The first asymmetric cell division cleaves the zygote (P_0) into the larger anterior blastomere (AB) and the smaller posterior blastomere (P_1). P_1 asymmetrically divides, resulting in EMS and P_2. Subsequent asymmetric cell division of EMS into MS and E, P_2 into C and P_3, and finally of P_3 into D and P_4 completes the generation of the founder cells (Sulston et al., 1983). The resulting cells differentiate to produce all cell types: the AB lineage produces the hypodermis, neurons, anterior pharynx and a range of cell types; MS gives rise to the somatic gonad, muscles, the majority of the pharynx, neurons, and gland cells; E makes up all intestinal cells; C produces muscle, the hypodermis and neurons; the D lineage differentiates into muscle; while the terminal cell of the P lineage, P_4, is the germline precursor (Gönczy and Rose, 2005).

Sidney Brenner chose the 1 mm long worm as a model organism to investigate mutations that cause behavioural defects. The decision to use *C. elegans* was based on its numerous advantages, such as a short life cycle of only 3 days under optimal conditions, small genome, small cell number in the nervous system, fast generation of mutants, and ease of culture in the laboratory (Brenner, 1974). Following the extended use of *C. elegans* in laboratories more advantages have become apparent: an invariant cell number of approximately 1000, the complete description of all cell lineages, genetically identical progeny caused by self fertilisation, and a well-annotated, fully-sequenced genome. Three recent Noble prizes have

been awarded to researchers for their findings in *C. elegans*: in 2002, for discoveries concerning genetic regulation of organ development and programmed cell death; in 2006, for the discovery of RNA interference – gene silencing by double-stranded RNA; and in 2008, for the discovery and development of the green fluorescent protein (GFP) (www.nobelprize.org).

The body plan of *C. elegans*, like that of other nematodes, is simple: An unsegmented, cylindrical body is divided into an outer and inner tube, which are separated by the pseudocoelom. The body wall, which makes up the outer tube, consists of cuticle, hypodermis, excretory system, neurons and muscles. The inner tube comprises the pharynx, intestines and the gonad (WormAtlas).

The life cycle of *C. elegans* is divided into embryonic stage, four larval stages (L1 to L4) and adulthood. Each larval stage ends with a molt. In the absence of a sufficient food source, L2 larvae enter the dauer stage and can survive up to 4 months of food shortage. While the generation time is only 3 days, the life span reaches about 3 weeks under optimal conditions (WormAtlas, **Figure 1**).

C. elegans has five pairs of autosomes and one pair of sex chromosomes that defines the two genders: hermaphrodites (XX) and males (XO). Self-fertilizing hermaphrodites dominate *C. elegans* populations. Males arise spontaneously by non-disjunction of the X chromosome during meiosis. The frequency of males is very low in laboratory populations (0.1%) but can be increased to 50% through mating. During its life, a hermaphrodite produces sperm in the L4 stage and stores it in the spermatheca. Subsequently, it switches to oocyte production and approximately 300 eggs are fertilised with self-produced sperm. Self-fertilisation of the homozygous hermaphrodite results in identical progeny and, in the laboratory, male mating facilitates isolation and maintenance of mutant strains as well as introduction of new mutations to a strain (WormAtlas).

The early cell divisions proceed in a typical manner and in rapid sequence: the first division is completed approximately 20 minutes after onset of polarity. The embryo itself is 50 µm in

length and 30 µm in diameter, making it easily accessible for imaging and optical manipulations (e.g., for laser ablation) (Oegema and Hyman, 2006).

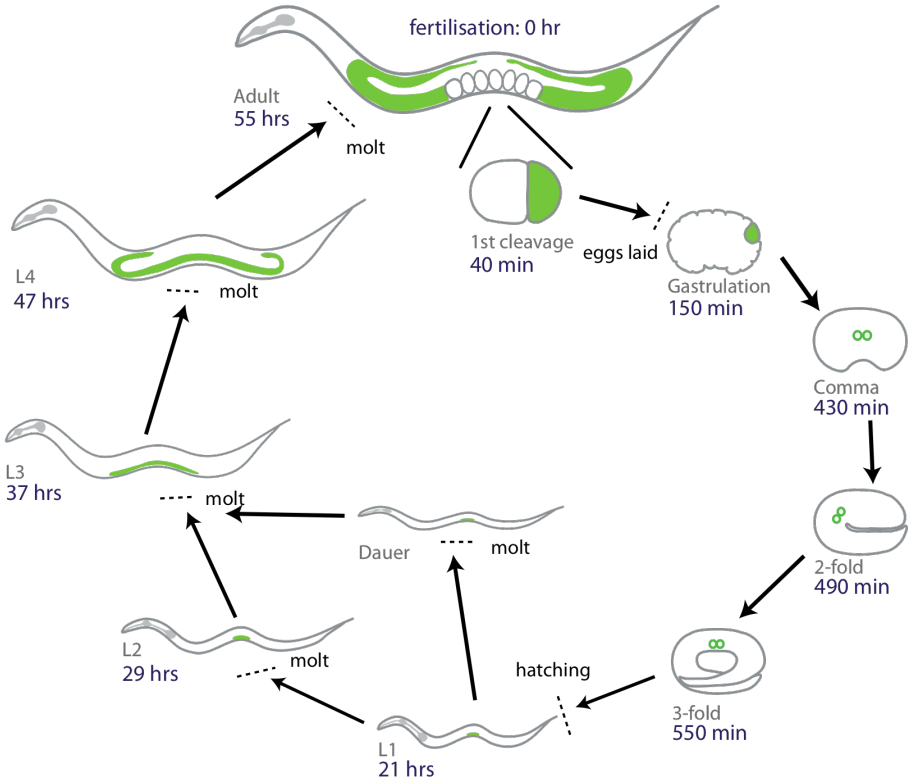

Figure 1: Life cycle of *C. elegans*. The life cycle starts with fertilisation (0 hr). The first few cell divisions of the fertilised egg are *in utero*. The eggs are laid during the gastrulation stage. The embryogenesis takes about 9 hours and ends with the hatching of the worm. With each molt a new developmental stage starts. After 55 hours the worm has grown into an adult. The times given are for a life cycle at 22°C. The cells of the germ lineage are shaded green; the pharynx gray. Adapted from WormAtlas.

1.3 Asymmetric Cell Division in C. elegans

1.3.1 Oogenesis to first cell division in *C. elegans*

In *C. elegans*, the reproductive system consists of the somatic gonad, the germline and the egg-laying apparatus. The two U-shape gonad arms are connected to the shared uterus through the two spermathecae, the sperm-storing compartments. Each ovary (distal gonad arm) is made up of a monolayer of somatic myo-epithelial sheaths cells and a basal membrane, which surrounds the germline (WormAtlas; **Figure 2**).

Oogenesis takes place in each of the two arms of the ovaries. The germline stem cells are positioned at the distal tip of the syncitial gonad arm. In their undifferentiated and mitotic

state, these germline stem cells continually produce new germ cells. Cubical membranes surround the nuclei with the open side facing the lumen of the gonad arm. As the nuclei move away from the distal tip, they lose their mitotic potential, begin meiosis, and become fully surrounded by plasma membrane. While accumulating yolk granules and growing in size, the oocytes move towards the spermatheca where the fertilisation will take place. The unfertilised oocyte arrests in meiotic prophase I. During fertilization, the sperm and the surrounding gonad tissue provide signals to the oocyte to complete its maturation (Greenstein, 2005).

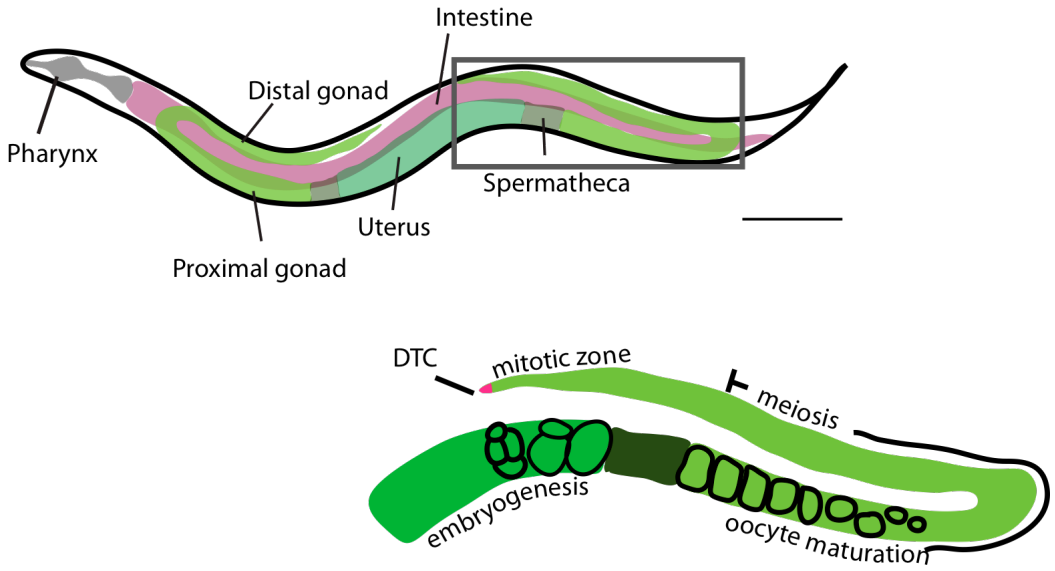

Figure 2: Reproductive system of *C. elegans*. The two arms of the gonad make up most of the adult worm. The distal tip cells (DTC) are the germline stem cells and undergo mitotic divisions to produces germ cells, which gain meiotic potential as they move towards the proximal gonad. Membranes enclose the nuclei and the formed oocytes mature while travelling towards the spermatheca to become fertilised. The first cell division of the embryo happen *in utero*. The enlargement shows one gonad arm. The scale bar represents 0.1 mm. Adapted from WormAtlas.

Ovulation pushes the oocyte into the spermatheca for fertilisation. Prior to sperm entry, the oocyte's pronucleus moves to the side of the egg that is furthest away from the spermatheca (Goldstein and Hird, 1996). Thus the sperm usually, but not always, enters at the opposite site of the maternal pronucleus. The unfertilised oocyte has no developmentally relevant asymmetry: there is no preference as to where polarity will be established. With completion of meiosis, the zygote starts producing the three layers of eggshell: an outer vitilline layer, a

middle chitinous layer and an inner lipid-rich layer (WormAtlas). The production of the eggshell is linked to a successful meiosis; in weak mutants where the separation of the sister chromatids in meiotic anaphase II is affected, the secretion of the eggshell is also impaired (Shakes et al., 2003).

After fertilisation, dramatic changes take place in the zygote. The plasma membrane begins to ruffle, which can be observed as temporary invaginations of the cortex. This causes cytoplasmic streaming, while the nucleus–centrosome complex moves randomly in proximity to the cortex within the embryo. Prior to polarity establishment (-12:00 [min:sec] relative to nuclear envelope breakdown [NEBD]), the pronuclei increase in size because of DNA synthesis. Also, the pair of sperm-provided centrioles starts recruiting pericentriolar material (PCM) and acquires microtubule nucleation potential (O'Connell, 2000; Pelletier et al., 2004). In addition, the random motion of centrosomes changes into a directed movement to the posterior cortex (Cowan and Hyman, 2004b). At the time of publication, the mechanism of action for this movement was not established.

Polarity establishment is initially evident in a small cortical region overlying the centrosomes. Here, the cortical contractions stop, and the plasma membrane shows no invaginations and becomes smooth. At this point, the anterior–posterior axis is set up in the embryo. Both pronuclei continuously increase in size, while the two centrioles separate to form two new centrosomes on opposite sides of the paternal pronucleus (Gönczy et al., 1999b).

The smoothing of the membrane spreads symmetrically from the point of symmetry breaking towards the anterior (Cuenca et al., 2003). The smooth domain reaches its maximum size at pseudocleavage; the embryo is partially divided by a single reversible ingression (-4:00 relative to NEBD). The centrosome–pronucleus complex stays in the proximity of the cortex during polarity establishment.

In mitotic prophase, the chromosomes condense and the centrosomes continue accumulating pericentriolar material and nucleating astral microtubules. The pronuclei migrate towards each other. The initial movement of the maternal pronucleus is slow but speeds up 5- to 10-fold to meet the paternal pronucleus in the posterior half of the embryo (-3:00 relative to

NEBD; 0.6 embryo length [EL]). The favoured model is a "pulling" of the paternal pronucleus towards the cell centre by astral microtubules attached to the force generator dynein, which is anchored to the cortex (Kimura and Onami, 2005). However, slow pronuclear movement is still observed in embryos that are compromised in the microtubule cytoskeleton, lack centrosomes or fail to recruit dynein to the nuclear envelope (Cowan and Hyman, 2004b; Schmidt et al., 2005), in which cytoplasmic flow may contribute to pronuclear movement (Goldstein and Hird, 1996).

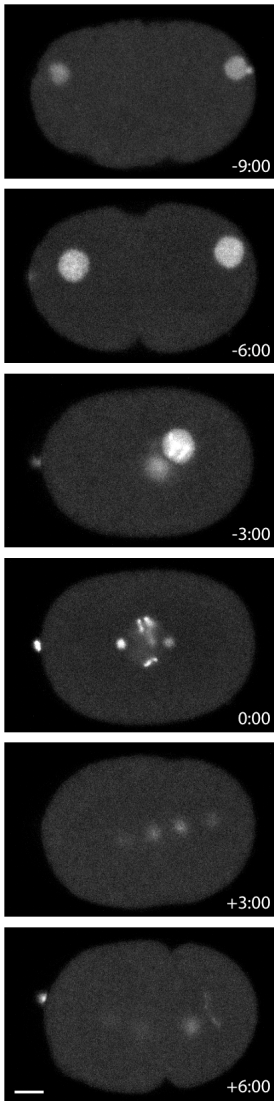

Figure 3: Time-lapse images of the first cell division in *C. elegans*. At -9:00, polarity has established and the posterior smooth domain expands. At -6:00, pronuclei migration begins and the chromosomes start condensation. At -3:00, the pronuclei meet and move to the centre of the embryo. At 0:00 (NEBD) the nuclear envelope completes disassembly while the spindle aligns along the anterior–posterior axis. At +3:00, centrosomes are separated and the spindle is asymmetrically displaced to the posterior. At +6:00, the cell division is finished. The chromosomes are visualised with histon 2B, the centrosomes with γ-tublin. All times are relative to NEBD. The anterior is to the left. The scale bar represents 10 µm.

The pronuclei–spindle complex moves to the centre of the embryo and centrosomes align with the anterior–posterior axis of the egg by performing a 90˚ rotation (Albertson, 1984). Subsequently, at NEBD (0:00), the chromosomes align at the metaphase plate and the two spindle poles face the poles of the embryo (**Figure 3**). Centration and rotation of the pronuclei–spindle complex is dependent on dynein and dynactin as well as long astral microtubules, which are anchored to the plasma membrane (Gönczy et al., 1999a; Skop and White, 1998).

The separation of the chromosomes in anaphase is mediated by unequal forces acting on the two spindle poles, resulting in an asymmetric elongation of the spindle, its posterior displacement and oscillation of the posterior spindle pole (Grill et al., 2001; Labbé et al., 2004). Concurrently, an actin-myosin-based contractile ring assembles on the inner surface of the plasma membrane in preparation for cytokinesis (Schroeder, 1973). The mitotic spindle positions the contractile ring; the upstream signals originate in the central spindle and astral microtubules (Bringmann and Hyman, 2005; Dechant and Glotzer, 2003). The posterior displacement of the spindle causes the cleavage to be likewise displaced slightly to the posterior. The activity of the motor protein myosin drives the sliding of actin filaments to constrict the actin-myosin ring, resulting in ingression of the cleavage furrow and, finally, abscission (Glotzer, 2009). This process results in a two-cell embryo with each blastomere differing in size and cell fate.

For a successful asymmetric cell division, three initial steps are essential: First, a polarity cue breaks the symmetry of the egg and orients the anterior–posterior axis. Second, according to this axis, domains involving PAR proteins are formed at the cortex. Third, the information at the cortex is transduced into the cell and polarises the cytoplasm, leading to the asymmetric segregation of cell fate determinates (Cowan and Hyman, 2004a).

1.3.2 Symmetry breaking and polarity establishment

The fertilising sperm contributes a pronucleus, centrosome and cytoplasm to the oocyte. Approximately 20 min after fertilization, the first signs of polarity are observed; centrosomes

move to the cortex and the posterior cortex smoothes. At the time of publication, the cue that triggers these events was not established; however, evidence supports the sperm-supplied centrosomal signal hypothesis: The site of the sperm entry and the position of the polarity establishment are both in the posterior of the egg (Goldstein and Hird, 1996). Furthermore the paternal pronucleus–centrosome complex moves the site of polarity initiation (Cowan and Hyman, 2004b). Anucleated sperm is sufficient to induce the establishment of the anterior–posterior axis, leaving the centrosome as a potential cue (Sadler and Shakes, 2000). Following up on this evidence, embryos with mutations in the centrosomal proteins *sp*indle *d*efective (SPD)-2 and -5 were analysed. The embryos demonstrate severe defects in the recruitment of PCM, which cause impairment of the function of centrosomes and the establishment of polarity (Hamill et al., 2002; O'Connell et al., 2000).

Additional evidence that the symmetry breaking cue is given by a centrosomal component comes from laser ablation experiments where the physical destruction of centrosomes prevents polarity established (Cowan and Hyman, 2004b). The timing of the ablation is crucial. The removal of the centrosomes can only prevent polarity when performed prior to the establishment of polarity.

The cyclin E (CYE-1)–cyclin dependent kinase (CDK)-2 complex times the recruitment of centrosomal proteins to polarity establishment. Inactivation of this complex interferes with the correct assembly of the centrosomes and consequently with polarity establishment (Cowan and Hyman, 2006).

1.3.3 Contractile polarity

Shortly after the oocyte has completed the cortical rearrangement required to exclude the polar bodies, the ruffling of the entire cortex begins. This involves contraction of the underlying actomyosin network, as demonstrated by the addition of the actin depolymerisation drug cytochalisin, which abolishes all cortical activity (Hill and Strome, 1988, 1990; Strome and Wood, 1983). Additional evidence to support actomyosin-based contractions comes from RNAi depletion experiments targeted against the actin nucleators formin-homology protein CYK-1, *p*ro*f*ili*n*-1 (PFN-1), and the *n*onmuscle *my*osin (NMY)-2

heavy chain and its regulatory *m*yosin *l*ight *c*hain (MLC)-4, which disrupted the integrity of the cortical actomysoin network and prevent ruffling as well as polarity establishment (Guo and Kemphues, 1996; Severson et al., 2002; Shelton et al., 1999).

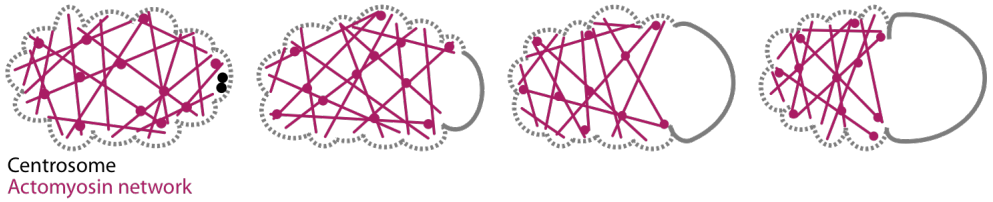

Figure 4: Contractile polarity in *C. elegans* one-cell embryo. Upon the symmetric breaking cue given by a centrosomal component, the cortical ruffling induced by actomyosin-based contractions ease to the anterior; leaving the posterior domain smooth. This domain expands and reaches it maximum dimension at pseudoclevage. The dashed line shows the contracile cortical domain; the solid line indicates the smooth domain. The anterior of the embryo is to the left. Adapted from Cowan and Hyman (2007).

Contractile polarity describes the asymmetry of cortical activity; the anterior cortex ruffles while the posterior cortex is smooth (**Figure 4**). The asymmetry in contractile polarity can be visualised by time-lapse recording of GFP-tagged version of NMY-2: contractions are seen as dense foci of NMY-2 that move from the anterior to the posterior leaving the anterior pole free of cortical NMY-2 (Motegi and Sugimoto, 2006). This depends on the regulated activity of the small GTPase Rho (RHO-1) (Motegi and Sugimoto, 2006; Schonegg and Hyman, 2006). RHO-1 is activated by the activator guanine nucleotide exchange factor (GEF), ECT-2, and inactivated by the GTPase-activating protein (GAP), CYK-4 (Motegi and Sugimoto, 2006; Schonegg and Hyman, 2006). The asymmetry in contractile polarity is initiated by removing ECT-2 from the site of polarity establishment (Motegi and Sugimoto, 2006). Subsequently, the sperm-donated population of CYK-4 localises to the small cortical region in proximity to the pronucleus–centrosome complex (Jenkins et al., 2006), which results in the easing of contractions. The smooth cortical domain expands towards the anterior until approximately half the embryo is occupied: RHO-1 and ECT-2 follow the boundary of the shrinking contractile domain (Motegi and Sugimoto, 2006).

The establishment of cortical polarity dictates, in part, the establishment of PAR polarity: PAR protein complexes localise exclusively to either the anterior or posterior cortex of the

one-cell embryo. The mutant in MLC-4 and NMY-2 disrupt the actomyosin network and are not able to establish polarity – either contractile or PAR polarity (Guo and Kemphues, 1996; Severson et al., 2002; Shelton et al., 1999). The initiation of contractile polarity appears to be PAR-protein independent because the two contractile domains are still formed in PAR null mutants (Kirby et al., 1990; Munro et al., 2004).

1.3.4 PAR polarity

The first PAR proteins were identified in a screen for proteins involved in the early development of *C. elegans* (Kemphues et al., 1988). Mutations in any of these genes revealed a partioning defective (PAR) phenotype resulting in symmetric cell divisions. PAR-1 and PAR-4 are serine/threonine kinases (Guo and Kemphues, 1996; Watts et al., 1996). PAR-5 belongs to the 14-3-3 protein family, which serves as adaptor/scaffold proteins with specific binding to phosphorylated serines and threonines (Morton et al., 2002). The PSD-95/disc-large/ZO-1 (PDZ) domain in PAR-3 and PAR-6 is often found in scaffolding proteins that facilitate protein–protein interactions (Hung and Kemphues, 1999). PAR-2 contains a RING (*r*eally *i*nteresting *n*ew *g*ene) finger: this protein domain is often found in E3 ligases that target proteins for degradation via the ubiquitin–proteasome pathway (Boyd et al., 1996; Levitan et al., 1994). Some of the PAR proteins demonstrate a particular cortical localisation: PAR-3 and PAR-6 are found at the anterior cortex, PAR-1 and PAR-2 at the posterior, while PAR-4 and PAR-5 are symmetrically distributed at the cortex as well as in the cytoplasm (Boyd et al., 1996; Etemad-Moghadam et al., 1995; Guo and Kemphues, 1995; Hung and Kemphues, 1999; Levitan et al., 1994; Morton et al., 2002).

Prior to polarity establishment, the anterior PAR proteins are uniformly distributed at the cell cortex, revealed by imaging of GFP:PAR-6 (Cuenca et al., 2003). With the smoothing of the posterior cortex, the anterior PAR proteins recede and follow the contractile domain towards the anterior. Subsequently, PAR-1 and PAR-2 access the cortex, which lacks the anterior PAR proteins. This posterior PAR domain retracts until it occupies half of the embryo. The contractile polarity domains precisely align with the PAR domains (**Figure 5**).

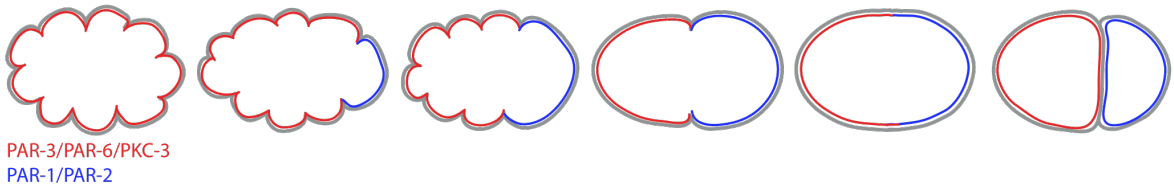

Figure 5: PAR polarity in *C. elegans* one-cell embryo. Upon symmetric breaking, the posterior PARs appear at the cortex. The posterior PAR domain expands and is inherited by the P_1 cell; the anterior PAR domain by the AB blastomere. The anterior of the embryo is to the left. Adapted from Cowan and Hyman (2007).

PAR-6 additionally interacts with the atypical protein kinase C (PKC)-3 and the actin nucleator CDC-42, forming the functional anterior PAR protein complex (Gotta and Ahringer, 2001a; Li et al., 2010; Tabuse et al., 1998). PAR-1 requires the presence of PAR-2 for proper cortical localisation (Boyd et al., 1996). The association to the cortex does not appear to be of a constant nature but rather follows a continuous on and off process; fluorescence recovery after photobleach (FRAP) experiments demonstrated that PAR-2 and PAR-6 dynamically associate with the cortex (Cheeks et al., 2004).

Reciprocal inhibitory interactions are thought to keep the anterior and posterior PAR domains separate. Downregulation or depletion of PAR-5 leads to mislocalisation of other PAR proteins; the anterior and posterior domains mix (Morton et al., 2002). The *p*rotein *k*inase *C* (PKC)-3 associates with the anterior PAR complex and phosphorylates PAR-2, which cannot bind to the cortex in its phosphorylated state. Thus, PKC-3 restricts PAR-2 from entering the anterior cortex (Hao et al., 2006).

PAR polarity can be divided into two distinct phases: establishment and maintenance (Cuenca et al., 2003). In PAR-2 mutants, the actomyosin network and the anterior PAR complex retracts to the anterior pole. The distinct domains are not maintained, and the PAR-3/PAR-6/PKC-3 complex uniformly redistributes along the cortex (Cuenca et al., 2003). The small GTPase CDC-42 contributes to the maintenance of PAR polarity by restricting NMY-2 to the anterior (Schonegg and Hyman, 2006). No PAR polarity is established if any of the anterior components are missing. The posterior PAR proteins are uniformly distributed along the cortex (Cowan and Hyman, 2007). The anterior PAR

proteins are involved in the establishment, while PAR-2 is essential for the maintenance of polarity.

1.3.5 Cytoplasmic polarity

The anterior–posterior axis of the embryo is set up by cortical polarity. Proteins downstream of the PAR proteins transduce the cortical signals to generate physical and functional asymmetry in the embryo. Physical asymmetry leads to two differently sized daughter cells, while functional asymmetry results in daughter cells with different fates.

PAR proteins orient spindle displacement according to the embryo's polarity axis. Downstream effectors organise the unequal force generation that causes the displacement of the cleavage furrow to the posterior (**Figure 6**). Together with the GoLoco-motiv proteins GPR-1/GPR-2 and the coiled-coil protein LIN-5, the redundant receptor independent G_{α} proteins GOA-1 and GPA-16 are largely responsible for the generation of the asymmetric force (Afshar et al., 2010; Afshar et al., 2004; Colombo et al., 2003; Gotta and Ahringer, 2001b; Grill et al., 2003; Srinivasan et al., 2003; Tsou et al., 2003). The PAR proteins are important for the asymmetric localisation of GPR-1/GPR-2 (Tsou et al., 2003). Upon depletion any PAR protein, no asymmetric forces at the spindle cannot be detected (Grill et al., 2003).

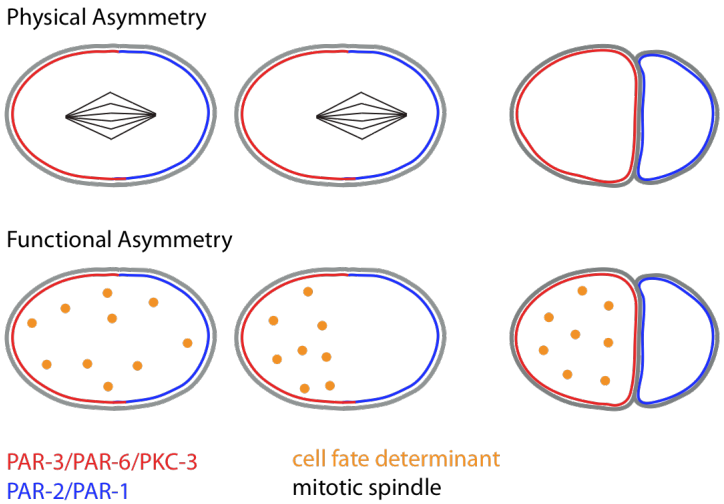

Figure 6: Cytoplasmic polarity in *C. elegans* one-cell embryo. The PAR proteins at the cell cortex organise the polarisation of the cytoplasm. The signals coming from the cortex induce the posterior displacement of the mitotic spindle during the first cell division, which results in asymmetric cell division. Furthermore cytoplasmic cell fate determinants localise asymmetrically according to the cortical polarity and are inherited by only one of the daughter cells, which will adopt a different cell fate than the other daughter.

The G_α proteins are symmetrically localised at the cortex (Afshar et al., 2004; Gotta and Ahringer, 2001b; Srinivasan et al., 2003) while LIN-5 and the GPR proteins are posteriorly enriched in the embryo from metaphase to anaphase in a PAR protein-dependent manner (Colombo et al., 2003; Gotta et al., 2003; Tsou et al., 2003). Depletion of either both G_α proteins, GPR-1/GPR-2, or of LIN-5 leads to symmetric cell division because no unequal force separates the spindles in anaphase (Gotta and Ahringer, 2001b; Gotta et al., 2003).

It is thought that a ternary complex is formed that is anchored by G_α proteins to the membrane. The GPR-1/GPR-2 act as a bridge between the G_α proteins and LIN-5, which in turn interacts with dynein (Nguyen-Ngoc et al., 2007). This builds a force generator that can interact with astral microtubules (Couwenbergs et al., 2007; Grill et al., 2003). It is most likely that a combination of shrinking microtubules and dynein motor function generates the required force for the spindle displacement. The asymmetric localisation of the GPR proteins could lead to asymmetric G_α signalling and consequently to unequal force generation on the spindle.

PAR proteins not only dictate the displacement of the spindle, but also the localisation of cell fate determinants, molecules that change the fate of a cell upon their inheritance (**Figure 6**). Three principal mechanisms could facilitate the asymmetric localisation of fate determinants: directed transport, localised degradation and translational control.

Large ribonucleoprotein complexes called P granules segregate to the posterior of the cell (Hird et al., 1996; Strome and Wood, 1983). Embryos expressing mutant PAR proteins have mislocalised P granules (Kemphues et al., 1988).

The following are examples of cell fate determinates that become asymmetrically segregated:

The CCCH zinc-finger protein *po*sterior *s*egregation (POS)-1 and its mRNA become asymmetrically enriched in the posterior cytoplasm during the first rounds of asymmetric cell divisions (Ogura et al., 2003; Tabara et al., 1999). POS-1 is essential for proper fate specification of germ cells (Tabara et al., 1999). *P* granule abnorma*l*ity (PGL)-1 interacts with the P granules and shows a similar asymmetric segregation pattern (Kawasaki et al.,

1998). *Spin*dle orientation defective (SPN)-4 localises to the P_1 cell where it is required for the rotation of the spindle in the P_1 cell (Gomes et al., 2001).

The cell fate determinant *p*osterior *al*ae in males (PAL)-1 is required for the specification of the C and D founder cells and functions in the P lineage, exclusively (Edgar et al., 2001; Hunter and Kenyon, 1996).

*M*uscle *ex*cess (MEX)-1 regulates the somatic cell differentiation in the early embryo and is expressed in P lineage blastomeres. In the two-cell stage of the embryo, it is required to restrict PIE-1 localisation to the P lineage (Guedes and Priess, 1997). *P*harynx and *i*ntestine *e*xcess (PIE)-1 regulates the specification of cells of the P lineage, and it is only found to localise to these cells (Mello et al., 1992).

1.4 P granules

The presence of membrane-free RNA-protein granules in a germline is a common feature throughout the animal kingdom; germ granules are found in *Drosophila*, *C. elegans*, *Xenopus levis*, *Mus musculus* and *Homo sapiens*, where they are called polar bodies, P granules, germinal granules and perinuclear nuage, respectively (Eddy, 1975; Strome and Lehmann, 2007). These germ granules are thought to contribute to the unique qualities of germ cells: pluripotency and immortality.

In *C. elegans*, the germ granules acquired their name from their specific segregation pattern; they are only inherited by cells of the P lineage: P_1 to P_4 (Strome and Wood, 1982, 1983). P granules are maternally produced and are found at high concentration in the gonads and in developing oocytes (Strome, 2005). At the time of fertilisation, approximately 200 small P granules are uniformly distributed in the egg. In the subsequent two rounds of cell division, the number of P granules decreases as the P_0 cell segregates into the germline blastomeres P_1 and P_2 (Ogura et al., 2003; Tabara et al., 1999). In P_2 cells and in cells that are further differentiated, the P granules attach to the nuclear envelope and appear to aggregate (DeRenzo et al., 2003; Spike et al., 2008b; Zhang et al., 2003).

Little is known about the mechanism that maintains the P granules in the germline. It was thought that a combination of posteriograde cytoplasmic flow, nuclear envelope association

and degradation contributed to their posterior enrichment and asymmetric segregation (Cheeks et al., 2004; DeRenzo et al., 2003; Hird et al., 1996; Strome, 2005). A more recent study analysed P granule dynamics using a biophysical approach (Brangwynne et al., 2009). They observed that P granules resemble liquid droplets in that they can undergo fusion, dripping and wetting, which gives rise to condensation and decondensation of the droplets. The reported contribution of cytoplasmic flow to the posterior enrichment of P granules seems to be negligible; instead an increase of P granule condensation in the posterior causes the accumulation of larger granules.

The list of proteins associated with P granules is increasing. To date, most of proteins were involved in RNA metabolism: Sm ribonuclease proteins facilitate mRNA splicing (Barbee et al., 2002), The eIF4E homologue IFE-1 regulates translation initiation (Amiri et al., 2001), GLD family proteins perform poly(A) polymerization (Barbee et al., 2002; Jones et al., 1996; Li et al., 2010; Li et al., 2009; Wang et al., 2002), and the novel protein DEPS-1 controls the content of mRNAi in P granules (Spike et al., 2008b). Several proteins associated with P granules contain predicted RNA-binding motifs: RGG in PGL proteins (Kawasaki et al., 2004; Kawasaki et al., 1998), DEAD box in GLH family (Kuznicki et al., 2000), KH motif in MEX-3 (Draper et al., 1996), CCCH zinc-fingers in PIE-1 (Mello et al., 1992), POS-1 (Tabara et al., 1999), MEX-1 (Guedes and Priess, 1997) and OMA-1 and -2 (Shimada et al., 2006), and PUF repeats in PUF (Pumilio and FBF) protein family (Zhang et al., 1997).

In addition to proteins, P granules also contain mRNAs. The proteins encoded by these mRNAs control a range of functions, including oocyte maturation (OMA-1, OMA-2), germline development (POS-1, MEX-1, NOS-2 and GLD-1), somatic development (SKN-1) and polarity (PAR-3) (Bowerman et al., 1993; Etemad-Moghadam et al., 1995; Guedes and Priess, 1997; Jones et al., 1996; Schisa et al., 2001; Tabara et al., 1999). The protein–RNA interactions may contribute to the structure of P granules.

The composition of P granules varies with the developmental stage of *C. elegans*. For example, members of the PUF protein family associate with P granules only in the germ cells in the distal arm of gonad where they regulate mRNA translation, providing the signal

to continue with the mitotic divisions and maintain the stem cell properties (Ariz et al., 2009; Wickens et al., 2002). In addition, the CCCH zinc-finger protein PIE-1 is only present in the early embryo where it functions as a germline cell fate determinant (Mello et al., 1992; Mello et al., 1996).

The experimental depletion of the constitutive P granule components PGL-1, GLD-1 and DEPS-1 cause altered P granule structure (Schisa et al., 2001; Spike et al., 2008b), and sterility of the adult hermaphrodite because of underproliferation of the germline (Kawasaki et al., 2004; Kawasaki et al., 1998; Kuznicki et al., 2000; Spike et al., 2008a). At present, no known component completely depletes the pool of P granules.

P granules may regulate the associated mRNAs on the post-transcriptional level, by 'sorting' newly transcribed mRNAs as they leave the nucleus and segregating bound mRNA and proteins to the P lineage, thus contributing to the germline fate of the P lineage (Guedes and Priess, 1997). In summary, P granules are essential for germline specification and consequently for the fertility of the worm.

1.5 The germline cell fate determinant PIE-1

PIE-1 was identified in a screen for maternal-effect mutant embryos with altered pharynx cell fate; its phenotype caused it to be named *p*harynx and *i*ntestines in *e*xcess (Mello et al., 1992). Loss-of-function mutations in *pie-1* results overproliferation of intestinal and pharynxal in cells of the embryo, which is caused by a loss of cell identity in the P lineage (Mello et al., 1992); these cells obtain a somatic fate instead of maintaining their germline identity. PIE-1 exclusively segregates to the cells of the P lineage and determines the fate of theses cells by acting as a transcriptional repressor. The transcriptional potential of cells destined to the P lineage is kept low. Thus protecting the germline stem cell from differentiation signals (Mello et al., 1996). Consequently, PIE-1 was reasoned to be a germline-specific cell fate determinant (Mello et al., 1996; Seydoux et al., 1996).

PIE-1 has a dynamic localisation pattern in the early embryo: uniform distribution in the newly fertilised egg and posterior enrichment before the first cell division, as well as association with centrosomes and P granules and nucleoplasmic localisation; its site of action

as a transcriptional repressor (Mello et al., 1996; Reese et al., 2000; Tenenhaus et al., 1998). In the following series of asymmetric cell divisions, PIE-1 is passed on to the cells destined to the P lineage (Gönczy and Rose, 2005). The segregation pattern of PIE-1 is shown in **Figure 7**. P_4 – the germ cell founder cell – divides into Z2 and Z3, where the inhibition of transcription is lifted by degradation of PIE-1 (Mello et al., 1992). The degradation is mediated by the *zi*nc-finger interacting *f*actor (ZIF)-1, which is involved in the clearance of PIE-1 from the somatic blastomeres via the ubiquitin–proteasome pathway (Checchi and Kelly, 2006; DeRenzo et al., 2003). The germline identity of these cells is thereafter maintained by modifications in the chromatin architecture (Schaner et al., 2003).

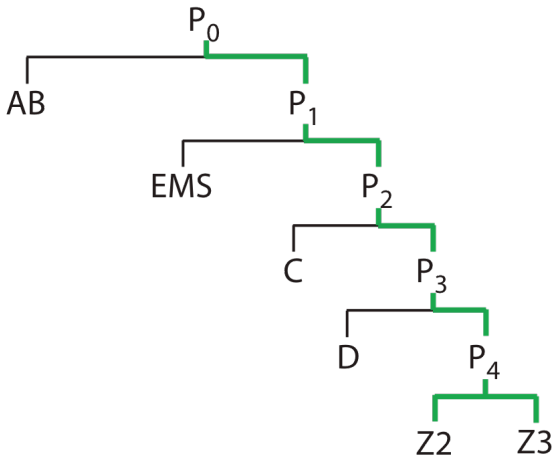

Figure 7: P lineage diagram of *C. elegans* embryo. The P lineage is established by a series of asymmetric cell divisions; represented by the horizontal bars. Each division gives rise to a somatic blastomere (AB, EMS, C, D) and a P lineage blastomere (P_1, P_2, P_3 and P_4). P_4 divides into the two germline precursors. The inheritance of PIE-1 is highlighted in green. Adapted from (Gönczy and Rose, 2005)

In a series of studies, the molecular mechanism of the transcriptional repression maintained by PIE-1 has been identified. In eukaryotes, the *p*ositive *t*ranscription *e*longation *f*actor *b* (P-TEFb) promotes gene expression. Shortly after the initiation of the mRNA transcription by RNA polymerase II (RNAPII), the polymerase stalls until its carboxy-terminal domain (CTD) is phosphorylated. P-TEFb is the active complex of Cyclin T1 and CDK-9, which binds to a heptapeptide repeat in the CTD of RNAPII and phosphorylates the signal epitopes within these repeats to continue mRNA transcription. PIE-1 has a non-phosphorylatable variation of the heptapeptide repeats, which can still be bound by CDK-9 (**Figure 8**). By

competing with RNAPII's CTD repeat for the binding to CDK-9, PIE-1 can repress the elongation of transcription (Batchelder et al., 1999; Ghosh and Seydoux, 2008; Tenenhaus et al., 1998; Tenenhaus et al., 2001; Zhang et al., 2003). However, there may be additional regions in PIE-1 required for proper transcriptional repression (Ghosh and Seydoux, 2008).

Several groups have investigated the mechanism of PIE-1's asymmetric localisation. *In situ* hybridisation studies demonstrated that PIE-1 mRNA is uniformly distributed from oocytes to the 4-cell stage of the embryo; degradation of PIE-1 mRNA is initiated in somatic blastomeres after this time point (Tenenhaus et al., 1998). In *in vivo* localisation studies, the GFP-tagged open reading frame (ORF) of *pie-1* was fused to the untranslated regions (UTRs) of a ubiquitously expressed gene and the expression of GFP scored. Additionally, GFP was fused to the *pie-1* UTRs and the segregation of GFP determined (DeRenzo et al., 2003; Reese et al., 2000). The coding sequence of *pie-1* was necessary and sufficient for the localisation of PIE-1 to the posterior of P_0 and segregation to the P lineage; this indicated that the information required for PIE-1 localisation is encoded in the protein itself (Reese et al., 2000).

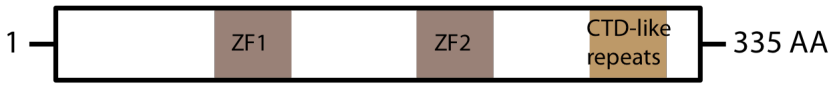

Figure 8: Schematic diagram of the protein domains in PIE-1. PIE-1 contains two zinc-finger (ZF) domains, which are established mRNA binding motifs. The CTD-like repeats are important for PIE-1's function as a transcriptional repressor. Adapted from Batchelder et al., (1999) and Mello et al. (1992)

Stepwise depletion and mutation of the *pie-1* gene demonstrated which domains are important for correct PIE-1 localisation (Reese et al., 2000). In addition to the previously described CTD-like motif, PIE-1 contains two CCCH zinc-fingers, which are established mRNA binding motifs (Blackshear, 2002; Mello et al., 1992). Elimination of the first zinc-finger domain (ZF1) efficiently abolishes the degradation of PIE-1 in the somatic cells after cell division. The second zinc-finger domain (ZF2), together with an unknown C' terminal region of PIE-1, is involved in the exclusive localisation of PIE-1 in the P lineage. ZF2 could

target GFP to the P granules but could not produce the typical segregation pattern, suggesting that P granule association alone is not sufficient for PIE-1's asymmetric segregation (Reese et al., 2000); leaving the localisation mechanism unknown.

The degradation of PIE-1 in the somatic lineages depends on the interaction of the ZF1 domain with the *z*inc-*f*inger *i*nteracting factor (ZIF)-1. ZIF-1 serves as a substrate-recruitment subunit for an *e*longinC-*c*ul2-*S*OCS box (ECS) ligase complex (DeRenzo et al., 2003); Therefore indicating that PIE-1 is degraded via the ubiquitin–proteasome pathway. The involvement of CUL-2 as the E3 ligase was established by partial CUL-2 depletion with RNAi experiments, in which PIE-1 was not degraded in the somatic cells (DeRenzo et al., 2003).

1.6 Aim of the project

The PAR proteins set up the anterior–posterior axis in the one-cell embryo. PIE-1's cytoplasmic asymmetry depends on the cortical polarity, defined by the PAR proteins and their associated partners. The cortical PAR polarity must be translated into cytoplasmic PIE-1 polarity to restrict PIE-1 segregation to cells of the P lineage during embryogenesis.

How does the spatial information provided at the cortex produce asymmetry inside the cell?

The regulation of PIE-1 asymmetry does not occur on mRNA level but is known to happen on protein level (Reese et al., 2000). The aim of my PhD project is to investigate the molecular mechanisms controlling the asymmetric segregation of PIE-1 and to gain insight into how the information from the cortex is transferred to the cytoplasm to create PIE-1 asymmetry.

2 Results

2.1 PIE-1 forms an exponential protein gradient

To gain detailed information about the cytoplasmic changes of PIE-1, I performed quantitative time-lapse recording of the PIE-1::GFP expressing worm strain JH1327 during the first cell division.

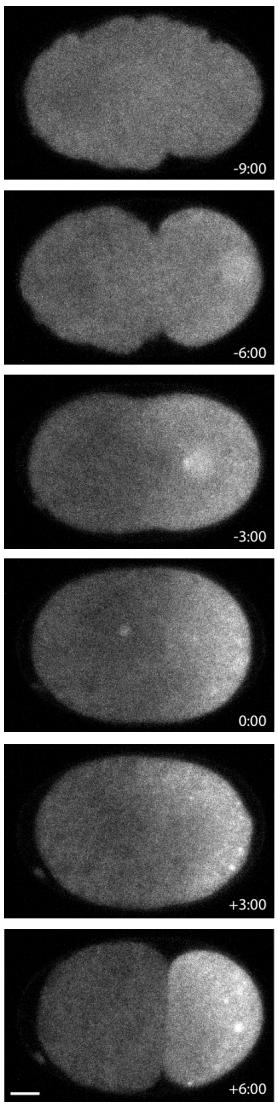

Figure 9: Time-lapse images of a one-cell embryo expressing PIE::GFP. The first cell division is shown. The scale bar represents 10 µm. The anterior is to the left.

I could observe the previously reported localisations of PIE-1 to the centrosomes, pronuclei and P granules (Mello et al., 1992; Mello et al., 1996; Seydoux et al., 1996). Before and at polarity establishment, PIE-1::GFP was evenly distributed in the cytoplasm of the zygote

(-12:00 [min:sec] relative to NEBD). After the onset of polarity and expansion of the smooth domain, PIE-1::GFP intensity increased near the posterior cortex. The cytoplasmic PIE-1::GFP formed a posterior crescent under the cortex, which followed the expanding smooth domain and spread until the posterior half of the embryo was occupied at 0:00 (NEBD). This asymmetry in PIE-1 localisation persisted through cell division. PIE-1 was only segregated to the P_1 cell (see **Figure 9**).

With different methods of intensity measurements, various aspects of the PIE-1::GFP asymmetry were addressed: The linescan intensity measurement showed the PIE-1::GFP profile along the anterior–posterior axis of a one-cell embryo (**Figure 10 A**). At 0:00 (NEBD), PIE-1::GFP intensities were highest at the posterior pole and decreased along the posterior–anterior axis. PIE-1::GFP intensities reached background levels around embryo length (EL) 0.4. An exponential decay function could be fit to the PIE-1::GFP profile. The decay constant λ describes an exponential gradient and gives a measure of its shape. In wildtype embryos, the determined decay constant λ of the PIE-1 gradient was 0.17 ± 0.01 EL (**Figure 11 C**).

The posterior–anterior ratio of PIE-1::GFP intensity described the posterior enrichment of PIE-1 during the first asymmetric cell division (**Figure 10 B**). The posterior enrichment of PIE-1::GFP increased steadily until -3:00 relative to NEBD and reached a final enrichment of 2.5-fold. I also measured the PIE-1::GFP intensities of the anterior and posterior cytoplasm during the first cell division (**Figure 10 C**). The PIE-1::GFP intensities measured in the anterior did not change while the posterior increased by 2-fold.

Thus, the increase of PIE-1::GFP intensity at the posterior pole of the embryo did not appear to involve a significant redistribution of protein from the anterior but instead might rely on new protein synthesis. PIE-1::GFP intensities were highest near the posterior cortex, the source of the exponential decay gradient.

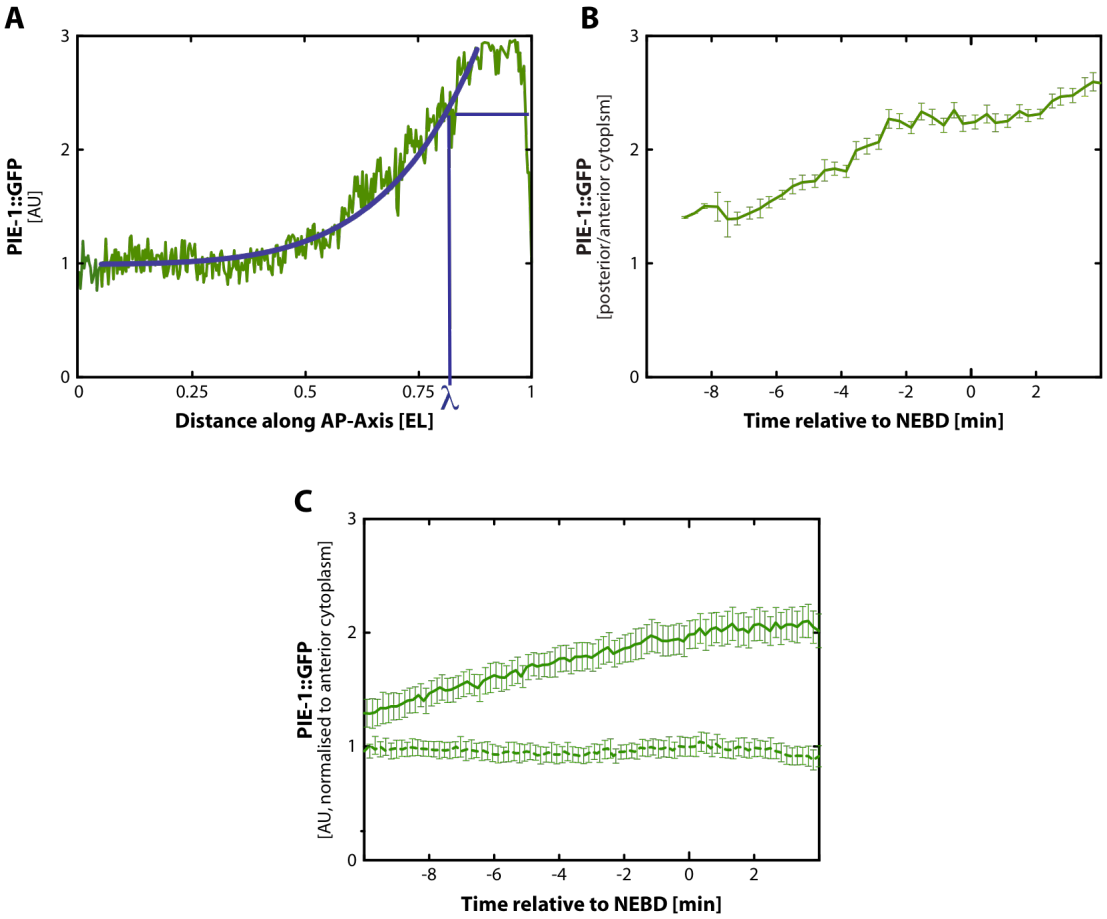

Figure 10: PIE-1::GFP forms an exponential gradient. A) Intensity profile along the anterior–posterior axis of a one-cell embryo at NEBD. The blue line shows the fit exponential curve. The decay constant λ is calculated in EL from the source of the gradient. **B)** Posterior enrichment of cytoplasmic PIE-1::GFP during the first cell division (n=7). **C)** Region measurements of cytoplasmic PIE-1::GFP near the anterior (dashed line) and posterior pole of the embryo (n=7). AU: arbitrary units, EL: embryo length, AP-Axis: anterior–posterior axis.

2.2 PIE-1 gradient formation

Next I wondered how this PIE-1 gradient could be formed. There are the possibilities of diffusion or active transport, for instance along microtubules.

2.2.1 The PIE-1 gradient appears to be shaped by diffusion

If diffusion generates the gradient, lowering the amount of protein should not change the decay constant λ. The maximum source intensity would be lower and the spread of PIE-1 would be less but the shape of the gradient remained the same. This hypothesis was tested by partial depletion of PIE-1 by RNAi followed by determination of the decay constant λ (**Figure 11 A**).

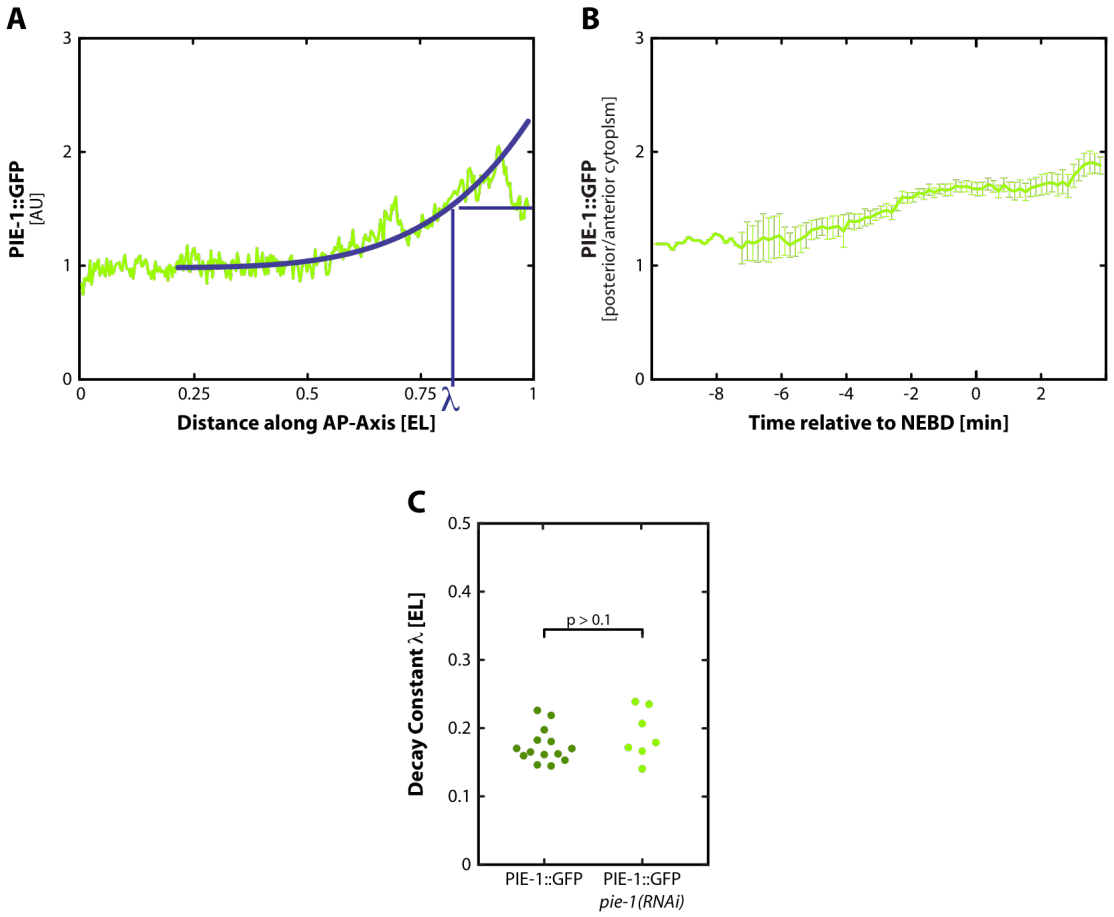

Figure 11: PIE-1 gradient is formed by diffusion. Analysis of *pie-1(partial RNAi)* embryos expressing PIE-1::GFP are shown. **A)** Intensity profile along the anterior–posterior axis of a single one-cell embryo at NEBD. The blue line shows the fit exponential curve. **B)** Posterior enrichment of cytoplasmic PIE1::GFP during the first cell division (n=7). **C)** Calculation of the decay constant λ. The average decay constant is 0.17 ± 0.01 EL in control (n=15) and 0.19 ± 0.01 EL in *pie-1(partial RNAi)* embryos (n=7). For statistical analysis an unpaired two-tailed student's t-test is used. AU: arbitrary units, EL: embryo length, AP-Axis: anterior–posterior axis.

The kinetics of the posterior enrichment and the formation of the exponential PIE-1 gradient were similar to the control. The partial depletion of PIE-1 resulted in a decrease of the posterior enrichment as well as the maximum PIE-1::GFP intensity at the cortex relative to control embryos. The decay constant λ did not change significantly upon partial depletion of PIE-1 (*pie-1(partial RNAi)*: 0.19 ± 0.01 EL, control: 0.17 ± 0.01 EL, p>0.1; **Figure 11 C**).

2.2.2 The PIE-1 gradient is not formed by microtubule-based transport

To rule out contribution of transport along the microtubules to the PIE-1 gradient formation, I inhibited microtubule polymerisation by nocodazole. The embryos were soaked in nocodazole solution and recorded by time-lapse microscopy during the first cell division. The migration of the pronuclei did not occur; indicating that the drug had reached the

embryo. The PIE-1 gradient was still formed at 0:00 (NEBD). The shape of the gradient after nocodazole treatment was not different from the control as determined by the decay constant λ (nocodazole: 0.15 ± 0.01 EL control: 0.18 ± 0.01 EL, p>0.1; **Figure 12**).

The exponential concentration gradient is formed rather by diffusion of PIE-1::GFP from the posterior source than by microtubule-based transport.

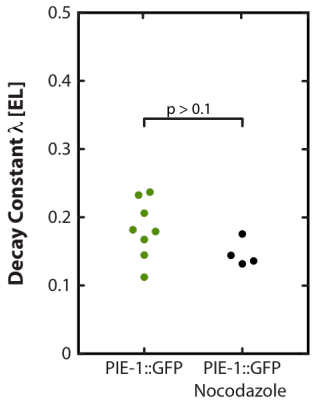

Figure 12: Microtubule-based transport does not contribute to PIE-1 gradient. The average decay constant λ in nocodazole-treated embryos is 0.15 ± 0.01 EL (n=4) and 0.18 ± 0.01 EL in untreated embryos (n=7). For statistical analysis an unpaired two-tailed student's t-test is used. EL: embryo length.

2.2.3 The PIE-1 gradient forms independent from cytoplasmic flow

With the onset of polarity, the cytoplasm begins streaming to the posterior, which redistributes e.g. yolk granules (Cheeks et al., 2004). These flows could mediate redistribution of existing PIE-1 protein from the anterior half of the embryo to the posterior and contribute to the PIE-1 gradient formation. To test this idea, I compromised the cytoplasmic flows with the allele *nop-1(it142)* (Rose et al., 1995). I performed time-lapse microscopy of UE12 embryos, which express PIE-1::GFP in the *nop-1(it142)* background during the first cell division. The PIE-1 gradient formation was analysed by the shape of the PIE-1 gradient (decay constant λ) and the goodness of the exponential fit to the PIE-1::GFP intensity profile along the anterior–posterior axis (R^2 value) in 30 sec intervals. I used the R^2 value to assign the time at which the PIE-1 gradient became statistically exponential, using the cut-off values of $R^2 \geq 0.75$.

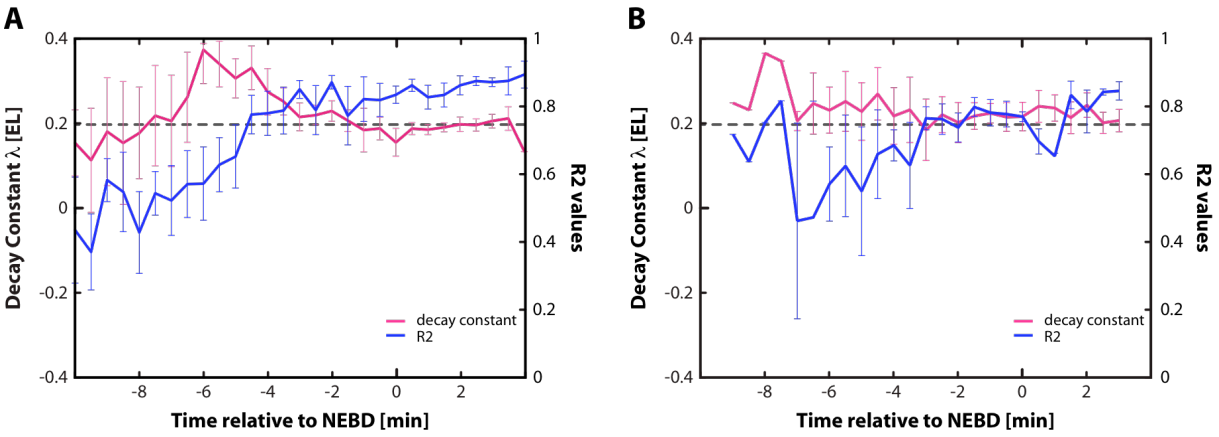

Figure 13: Cyotplasmic flows do not contribute to the PIE-1 gradient formation. Analysis of PIE-1 gradient formation by the shape of the gradient (decay constant λ, pink) and the goodness of the exponential fit to the PIE-1::GFP intensity profile along the anterior–posterior axis (R^2 value, blue) in control (**A**, n=10) and *nop-1(it142)* embryos expressing PIE-1::GFP (**B**, n=6). The dashed line indicates the cut-off value for exponential gradient formation ($R^2 \geq 0.75$). EL: embryo length.

In PIE-1 wildtype, the R^2 values increased during the first cell division, meaning that the exponential PIE-1 gradient was formed. The exponential gradient was established at -5:00 relative to NEBD (R^2=0.75). The shape of the PIE-1 gradient had a maximum spread of 0.38 EL at -6:00 relative to NEBD, which decreased to 0.17 EL at 0:00 (NEBD). The shape of the PIE-1 gradient remained stable after -3:00 relative to NEBD (**Figure 13 A**). This increase of the decay constant λ was likely due to the pseudocleavage furrow.

Compromising cytoplasmic flow only minorly changed the timing of PIE-1 gradient formation. The stabilization of the gradient shape occurred at the same time as in wildtype. The increase of the decay constant λ was lost as the pseudocleavage furrow did not form in *nop-1(it142)* embryos (**Figure 13 B**).

Cytoplasmic flows appear to have only a small contribution to PIE-1::GFP gradient formation.

2.2.4 The PIE-1 gradient is built by newly synthesised protein

PIE-1::GFP showed a dramatic increase in posterior enrichment, which seems to be largely independent of redistribution of present protein. I reasoned that newly synthesised protein in the posterior could explain the change in cytoplasmic PIE-1::GFP levels. To follow up on this idea, I imaged the first cell division of PIE-1::GFP expressing embryos and determined the increase of total integrated PIE-1 intensity. The integrated intensity increased from the

initial value at -9:00 relative to NEBD by 8% until the end of the measurement (-2:00 relative to NEBD, **Figure 14**).

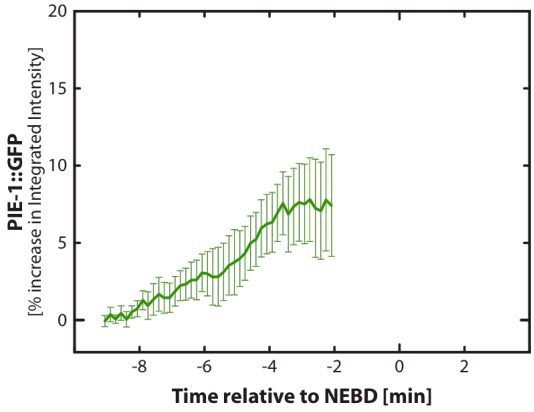

Figure 14: Newly synthesized protein forms the PIE-1 gradient. The increase of PIE-1 protein is determined by integrated intensity measurements between -9:00 and -2:00 relative to NEBD (n=5).

There was a total increase in PIE-1::GFP protein levels, which was most likely due to synthesis of new protein.

2.2.5 The PIE-1 gradient may be shaped by degradation in the anterior

Possible degradation of PIE-1 in the anterior might be detected by following the fate of posterior cytoplasm displaced into the anterior. Therefore I centrifuged embryos at high speed prior to time-lapse microscopy and measured the PIE-1::GFP intensity in the anterior and posterior cytoplasm.

Initially after centrifugation, PIE-1 was distributed uniformly throughout the cytoplasm, with roughly equal intensities at the anterior and posterior poles even though the embryos had progressed into the cell cycle and were about to undergo NEBD. Almost immediately however, cytoplasmic PIE-1::GFP levels decreased in the anterior while, at the posterior pole, the intensity levels increased (**Figure 15 A**). The PIE-1 gradient re-established within 3 minutes after recording start but with a slightly altered shape; most likely caused by the centrifugation (**Figure 15 B**). After approximately 2 minutes, PIE-1 stopped increasing in the posterior but PIE-1 continued to disappear from the anterior.

This could imply that the mislocalised PIE-1 in the anterior was degraded, although I could not eliminate the possibility of PIE-1 redistribution within the cytoplasm.

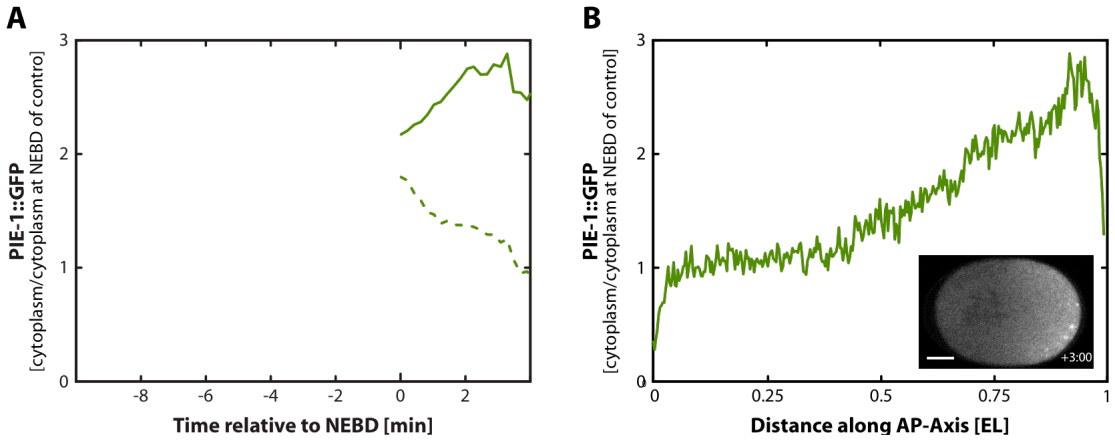

Figure 15: PIE-1 degradation in the anterior shapes the PIE-1 gradient. An embryo after cytoplasmic displacement by centrifugation is analysed for cytoplasmic levels of PIE-1::GFP near the anterior (dashed line) and posterior pole (**A**) and the PIE-1::GFP intensity profile along the anterior–posterior axis at +3:00 relative to NEBD (**B**). The still image shows the embryo at +3:00 relative to NEBD. The scale bar represents 10 µm. the anterior of the embryo is to the left. AU: arbitrary units, EL: embryo length, AP-Axis: anterior–posterior axis.

2.2.6 The PIE-1 gradient is not maintained by active processes

Next I wanted to address the question if active processes were involved in maintaining the PIE-1 gradient. Embryos were soaked in sodium azide solution for 30 to 40 minutes and analysed by time-lapse microscopy. The recording was started at pronuclei meeting (-3:00 relative to NEBD).

The embryos showed a very slow cell cycle: cytokinesis was never observed during the recording; indicating that the drug had reached the embryo. To detect possible changes in the shape of the PIE-1 gradient, the decay constant λ was calculated at the beginning of the recording and 6 minutes later, at +3:00 relative to NEBD. The decay constant λ was 0.25 ± 0.02 EL and 0.20 ± 0.02 EL at -3:00 and + 3:00 relative to NEBD, respectively. For both time points the decay constant λ was not significantly change from control values (0.22 ± 0.03 EL, $p>0.3$; 0.21 ± 0.01 EL, $p>0.5$, respectively; **Figure 16 A**).

Sodium azide treatment should inhibit the ATP-dependent processes in the embryo. To test the hypothesis that a diffusion-based mechanism was sufficient to form the PIE-1 gradient, I analysed the PIE-1::GFP mobility by fluorescence recovery after photobleach (FRAP). Embryos were soaked in sodium azide solution for 30 to 40 minutes and subjected to FRAP analysis. The bleach was performed near the posterior pole at the cortex. The measured half-time recoveries in control and sodium azide treatment were 2.69 ± 0.09 sec and 3.33 ± 0.30 sec, respectively. The difference was not significant ($p>0.3$; **Figure 16 B**). As a control I

used embryos of the worm strain WH508, which expresses cytoplasmic GFP. The mobility of cytoplasmic GFP should be based purely on diffusion and therefore unaffected by sodium azide inhibition of active processes. I could not detect a difference in the half-time recovery in treated and untreated embryos expressing cytoplasmic GFP (**Figure 16 B**).

The inhibition of active processes showed only a mild effect on the mobility of PIE-1::GFP. It seemed that passive processes, which I suggest to be diffusion, maintained the shape of the gradient.

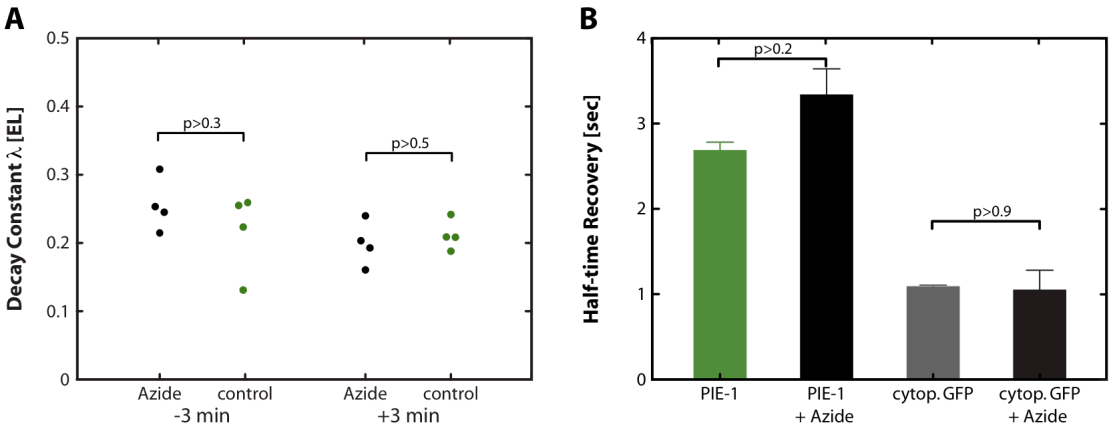

Figure 16: Active processes do not maintain the PIE-1 gradient. Embryos treated with sodium azide are analysed for the shape of the PIE-1 gradient (A) and by FRAP (B). **A)** In azide treated embryos, the average decay constant is 0.25 ± 0.02 EL (n=4) and 0.20 ± 0.02 EL (n=4) at -3:00 and at +3:00 relative to NEBD, respectively. In PIE-1 control embryos, the average decay constant is 0.22 ± 0.03 EL (n=4) and 0.21 ± 0.01 EL (n=4) at -3:00 and at +3:00 relative to NEBD, respectively. **B)** Half-time recoveries of FRAP experiments in embryos expressing PIE-1::GFP and cytoplasmic GFP. For statistical analysis an unpaired two-tailed student's t-test is used. EL: embryo length.

2.3 PIE-1 source formation

In the embryo, the position of the highest cytoplasmic PIE-1::GFP level was defined as the source of the PIE-1 gradient, which extended along the posterior cortex from the posterior pole in one-cell embryos.

2.3.1 The source of the gradient is positioned by PAR proteins

PAR proteins are known to organise the asymmetry of events in the cytoplasm. In order to determine whether they might direct the PIE-1 source to the posterior cortex, I performed time-lapse microscopy of embryos expressing GFP-tagged versions of PAR-2, PAR-6 and

PIE-1 and analysed their cortical distribution. The GFP intensities were measured cortically (PAR-2 and PAR-6) and sub-cortically (PIE-1) along the cortex of the embryo.

The plotted intensity profiles of PAR-2:GFP and PIE-1::GFP overlapped. The GFP intensities were highest at the posterior pole and decreased to background levels at the middle of the embryo, indicating that posterior PAR proteins share a similar localisation with the PIE-1 source (**Figure 17**).

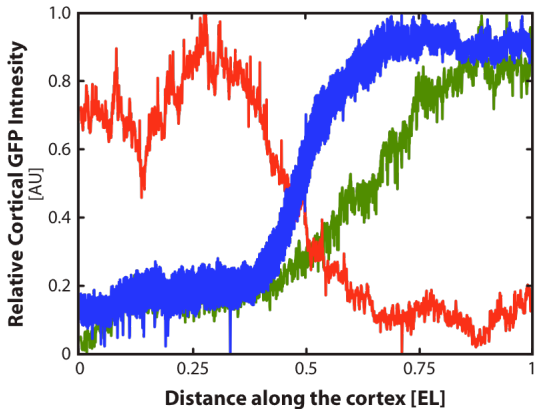

Figure 17: Posterior PAR proteins position PIE-1 source. The subcortical intensity profile of PIE-1 (green) and the cortical intensity profiles of PAR-2 (blue) and PAR-6 (red) are shown at NEBD (n=5).

2.3.2 PAR-3, PAR-6, PKC-3 and CDC-42 position the PIE-1 source

To address the question of whether the PAR proteins are essential for the position of the PIE-1 source, I depleted proteins of the anterior PAR polarity complex by RNAi in embryos expressing PIE-1::GFP and imaged the first cell division with time-lapse microscopy.

The depletion of PAR-3 resulted in uniform PIE-1::GFP segregation and symmetric cell division. The posterior enrichment as well as the exponential PIE-1 gradient were lost during the first cell division (**Figure 18 B**). Around -8:00 relative to NEBD, a rim of high PIE-1::GFP intensity was formed locally at the cortex, which disappeared by 0:00 (NEBD, **Figure 18 C**). After NEBD, the PIE-1::GFP intensities along the anterior–posterior axis were higher in the centre of the embryo than at the poles (**Figure 18 A**).

I confirmed the effects of loss of PAR-3 on the PIE-1 source by analysing *par-3(it71)* embryos expressing PIE-1::GFP. I could confirm the loss of posterior enrichment of

cytoplasmic PIE-1, uniformly distribution of cytoplasmic PIE-1 and rim formation in embryos depleted of PKC-3, CDC-42 or PAR-6.

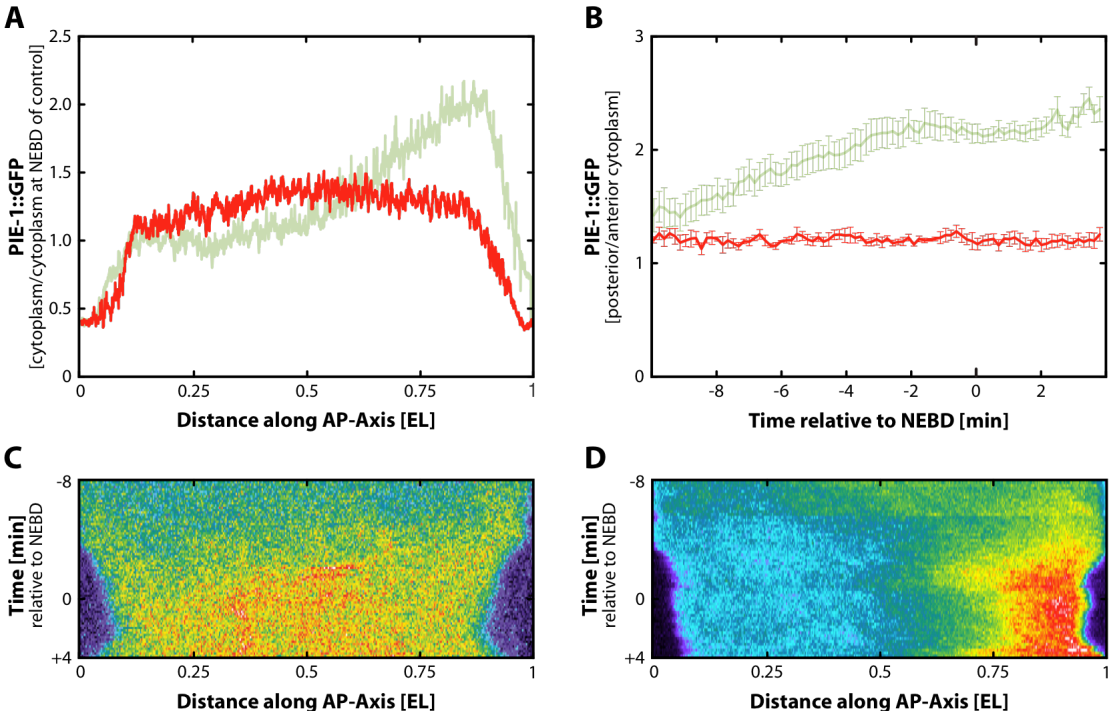

Figure 18: PIE-1 source position depends on PAR-3. A) Analysis of *par-3(RNAi)* embryos expressing PIE-1::GFP by linescan measurement along the anterior–posterior axis (n=5). **B)** Posterior enrichment of cytoplasmic PIE-1::GFP in *par-3(RNAi)* embryos (n=5). **C)** Pseudocoloured kymograph of PIE-1::GFP in one *par-3(RNAi)* embryo. **D)** Kymograph of a wildtype embryo. The pseudocolours indicate red as the highest intensity and blue the lowest. The measurements of wildtype embryos are shown in green. EL: embryo length, AP-Axis: anterior–posterior axis.

2.3.3 PAR-2 restricts the anterior PAR proteins to maintain the PIE-1 source

I next looked at PAR-2 depleted embryos expressing PIE-1::GFP. Until -4:00 relative to NEBD, cytoplasmic PIE-1::GFP was asymmetrically localised and showed posterior enrichment (**Figure 19 B**), consistent with previous data demonstrating that par-2(-) embryos initially established an asymmetric distribution of PAR-3/PAR-6/PKC-3 (Cuenca et al., 2003). Afterwards, the PIE-1 asymmetry was lost and the cytoplasmic levels were evenly distributed (**Figure 19 A** and **C)**, again consistent with regression of anterior PAR complex into the posterior half of the embryo in par-2(-) embryos (Cuenca et al., 2003). The depletion of PAR-2 resulted in uniform segregation of PIE-1::GFP to both daughter cells and symmetric cell division.

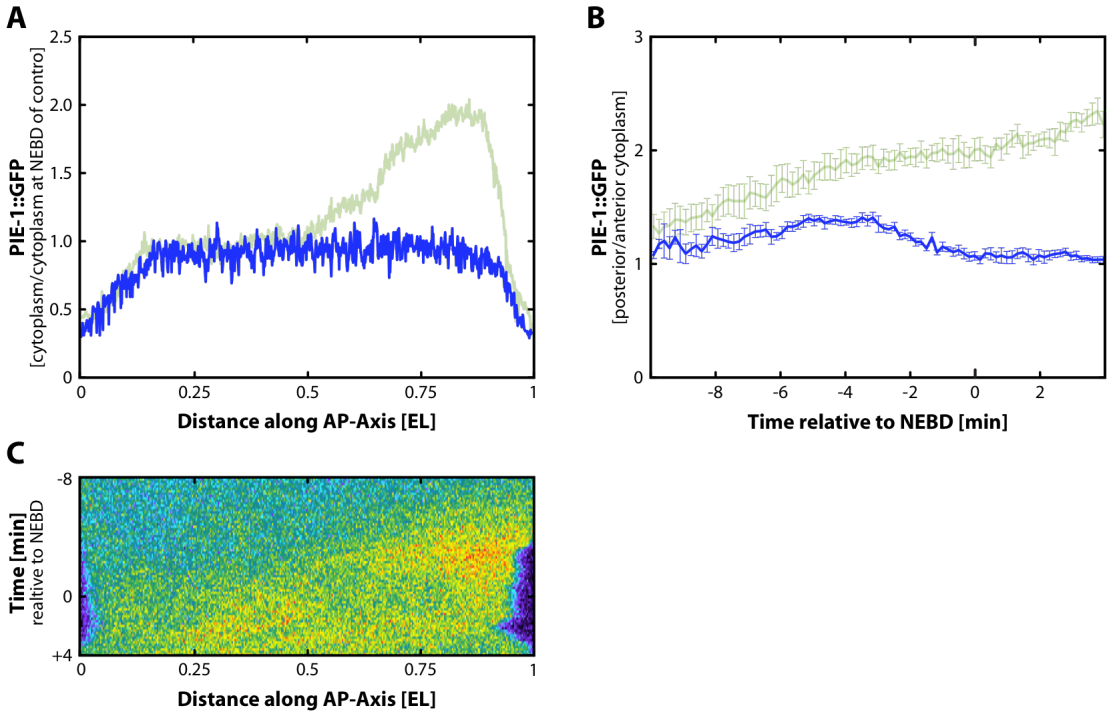

Figure 19: Maintenance of the PIE-1 source depends on PAR-2. Analysis of *par-2(RNAi)* embryos expressing PIE-1::GFP by linescan measurement along the anterior–posterior axis (**A**; n=5), posterior enrichment of cytoplasmic PIE-1::GFP (**B**; n=8) and kymograph (**C**). The pseudocolours indicate red as the highest intensity and blue the lowest. The measurements of wildtype embryos are shown in green. EL: embryo length, AP-Axis: anterior–posterior axis.

Thus PAR-2 appeared to be indirectly required for PIE-1 asymmetry by preventing localisation of the anterior PAR complex to the posterior cortex. PAR-3 and the other anterior PAR complex proteins localised the PIE-1 source but were not required for formation of the PIE-1 source near the cortex.

2.3.4 PAR-1 is required for formation of the PIE-1 source

Finally I analysed PIE-1 in embryos depleted of the posterior PAR domain component PAR-1.

The depletion of PAR-1 resulted in uniform segregation of cytoplasmic PIE-1::GFP and symmetric cell division. Throughout the first cell division, there was no evidence of posterior enrichment or gradient formation (**Figure 20**).

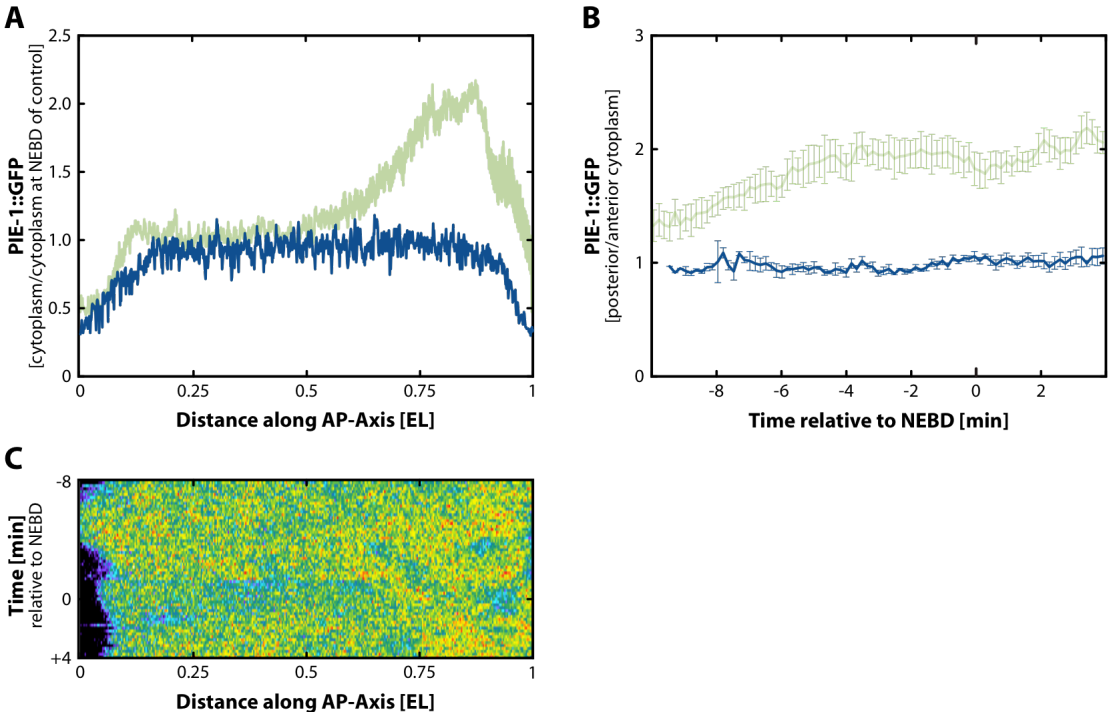

Figure 20: PIE-1 source position depends on PAR-1. Analysis of *par-1(RNAi)* embryos expressing PIE-1::GFP by linescan measurement along the anterior–posterior axis (**A**; n=5), posterior enrichment of cytoplasmic PIE-1::GFP (**B**; n=6) and kymograph (**C**). The pseudocolours indicate red as the highest intensity and blue the lowest. The measurements of wildtype embryos are shown in green. EL: embryo length, AP-Axis: anterior–posterior axis.

2.3.5 PAR-1 is required for PIE-1 production

While analysing the PIE-1 *par-1(RNAi)* movies, I observed a difference in total cytoplasmic PIE-1::GFP levels compared to control embryos. To investigate this further, I compared the increase of integrated intensity in *par-1(RNAi)*, *par-2(RNAi)* and *par-3(RNAi)* embryos during the first cell division. Indeed in embryos depleted of PAR-1, the increase in total PIE-1::GFP levels was negligible, while PIE-1 accumulation in *par-2(RNAi)* embryos was like wildtype. The depletion of PAR-3 resulted in an even greater increase in total PIE-1::GFP levels over time than the control (**Figure 21 A**).

To show that there was indeed less PIE-1::GFP protein present in *par-1(RNAi)* embryos, I analysed the protein levels by Western Blot. As expected, the depletion of PAR-2 and PAR-3 did not reduce the level of PIE-1::GFP relative to controls. The loss of PAR-1 lowered the amount of PIE-1::GFP protein by at least 10-fold (**Figure 21 B**).

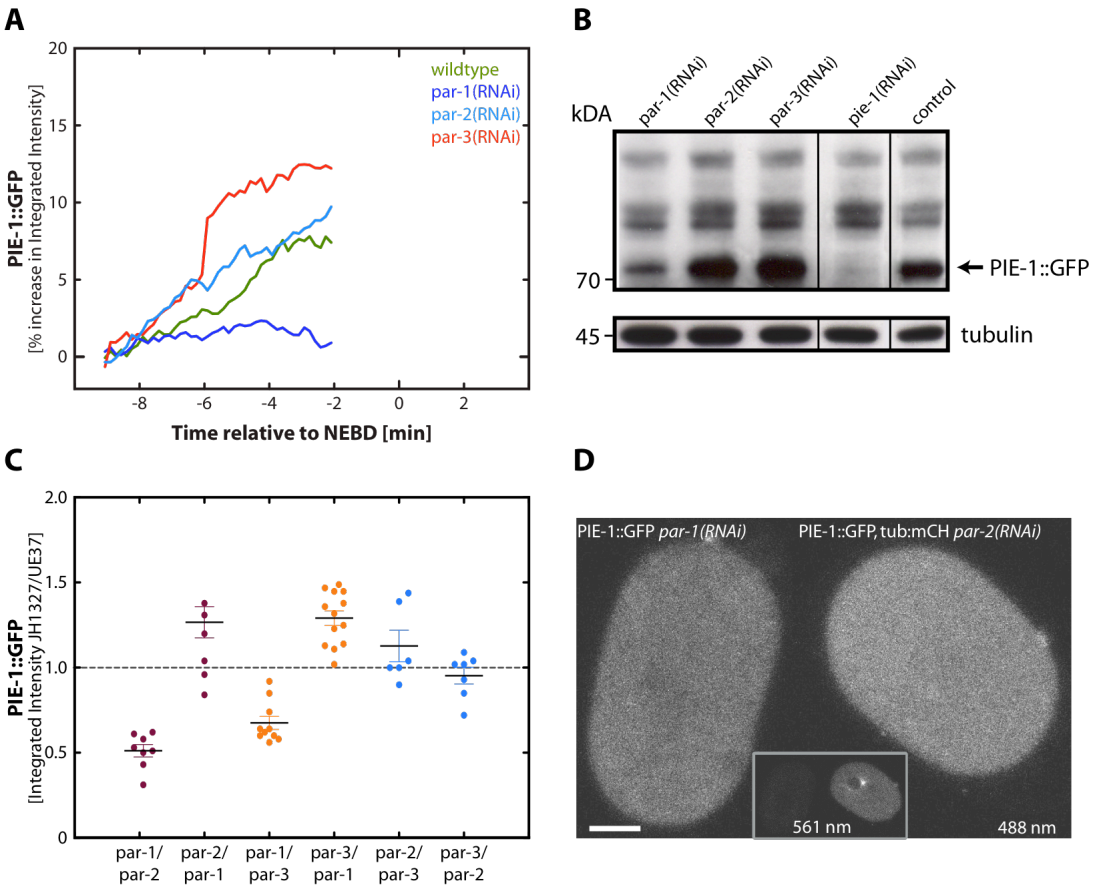

Figure 21: PAR-1 depletion inhibits PIE-1 source. A) Increase of total PIE-1 protein in embryos depleted of PAR-1 (n=3), PAR-2 (n=4), PAR-3 (n=4). **B)** Western Blot analysis of hermaphrodites fed with RNAis against PAR-1, PAR-2, PAR-3 and PIE-1. **C)** Ratios of measured integrated PIE-1::GFP intensities in JH1327 over UE37. **D)** Still image of an *par-1(RNAi)* embryo expressing PIE-1::GFP (left) and *par-2(RNAi)* embryo expressing PIE-1::GFP;mCH::β-tubulin. The insert shows the mCH signal. The scale bar represents 10 µm.

Next I wanted to compare the differences in PIE-1::GFP levels directly in embryos. I performed simultaneous time-lapse microscopy on embryos depleted of different PAR proteins. One embryo expressed PIE-1::GFP (JH1327) and the other PIE-1::GFP;mCH::β-tubulin (UE37), which allowed the genotypes to be distinguished. The ratio of integrated intensities of PIE-1::GFP in JH1327 to PIE-1::GFP in UE37 embryos was calculated at 0:00 (NEBD). The ratios were normalised to the control ratio. To avoid any genotypic difference, the reciprocal RNAi experiments were carried out.

In all cases, embryos depleted of PAR-1 had the lowest PIE-1::GFP intensities, reflected by ratios reflected by ratios approximately 50% higher or lower than the baseline. In contrast, ratios of PIE-1::GFP intensity in embryos depleted of PAR- 2 and PAR-3 were close to the baseline (**Figure 21 C**). The depletion of PAR-1 resulted in a reduction of cytoplasmic

PIE-1::GFP levels while depletion of PAR-2 and PAR-3 did not change the cytoplasmic PIE-1::GFP levels.

With these three independent experiments, I could confirm that PAR-1 was needed for formation of PIE-1 source while the other component of the PAR polarity were mainly involved in positioning the PIE-1 source.

2.3.6 Inhibition of polarity establishment does not eliminate the PIE-1 source

To answer the question if polarity establishment was needed for the formation of the PIE-1 source, I analysed embryos lacking functional centrosomes, which are required for polarity establishment in one-cell embryos. Therefore I performed quantitative time-lapse microscopy of *spd-5(RNAi)* embryos (Hamill et al., 2002) expressing PIE-1::GFP during the first cell division.

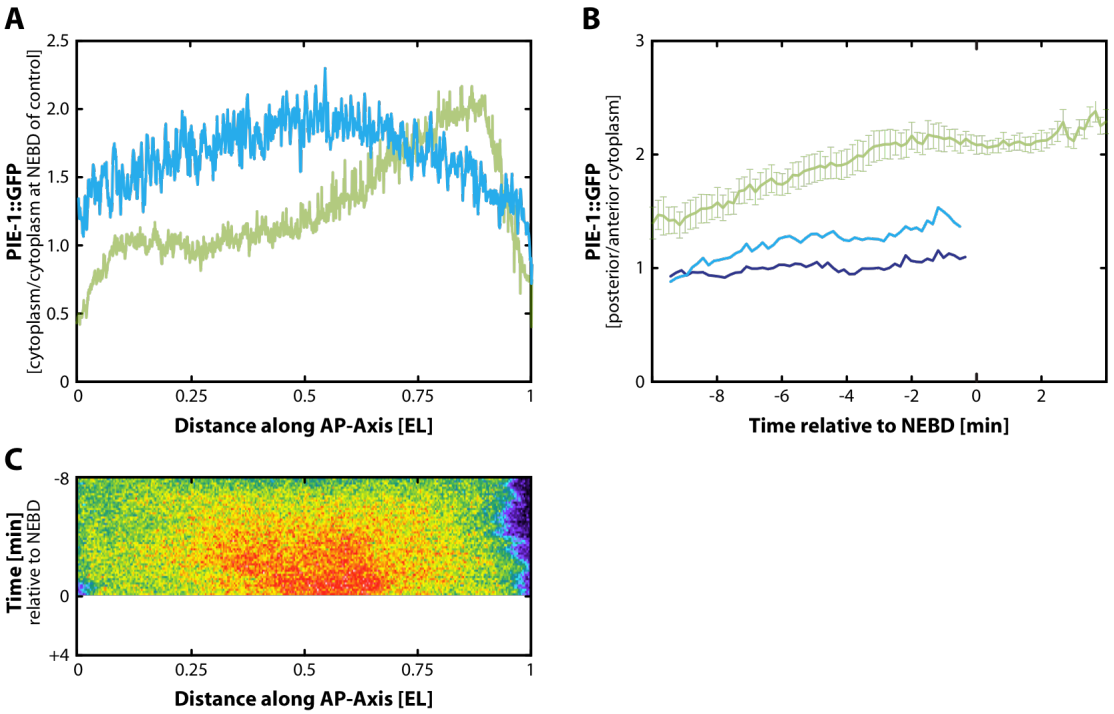

Figure 22: PIE-1 source forms without polarity establishment in *spd-5(RNAi)* embryos. Intensity profile of PIE-1::GFP at 0:00 (equivalent to control NEBD) (**A**; n=3), posterior–anterior ratio (dark blue) and centre–anterior ratio (light blue) of cytoplasmic PIE-1::GFP (**B**) and kymograph (**C**) of cytoplasmic PIE-1::GFP in embryos depleted of SPD-5 by RNAi. The pseudocolours indicate red as the highest intensity and blue the lowest. The measurements of wildtype embryos are shown in green. EL: embryo length, AP-Axis: anterior–posterior axis.

The embryos showed uniform cortical ruffling but no polarity. I used the size of the pronuclei to assign 0:00. In all embryos recorded, polarity establishment was rescued between -2:00 and 0:00. I focused on the time before the polarity rescue. Cytoplasmic PIE-1 and PIE-1 positive P granules, hereafter referred to as PIE granules, accumulated in the centre of the embryo before 0:00 (equivalent to NEBD, **Figure 22 A** and **C**). The posterior–anterior ratio showed no enrichment of cytoplasmic PIE-1::GFP; however, the ratio of PIE-1 in the centre of the embryo over the anterior showed a 1.5-fold increase (**Figure 22 B**).

The prevention of polarity establishment by loss of functional centrosomes did not inhibit PIE-1 source formation, although the correct position of the PIE-1 source was impaired.

2.3.6.1 Cytochalisin D treatment does not eliminate the PIE-1 source

To confirm that polarity establishment was not required for PIE-1 source formation, I used cytochalisin D to inhibit polarity establishment. This actin depolymerising agent interferes with contractile polarity and prevented any PAR polarity (Hill and Strome, 1988). The embryos were soaked in cytochalisin D solution and analysed by time-lapse microscopy.

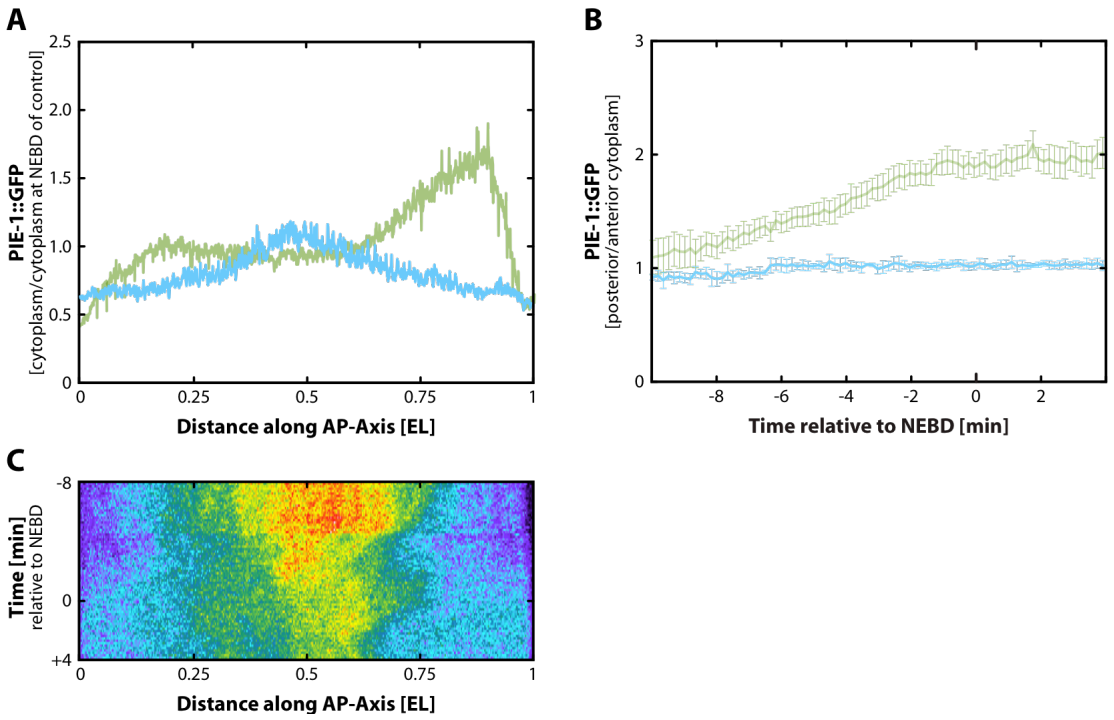

Figure 23: PIE-1 source forms after cytochalisin D treatment. Linescan measurements at 0:00 (NEBD) (**A**; n=3), posterior–anterior ratio (**B**; n=5) and kymograph (**C**) of cytoplasmic PIE-1::GFP in embryos treated with cytochalisin D. The pseudocolours indicate red as the highest intensity and blue the lowest. The measurements of wildtype embryos are shown in green. EL: embryo length, AP-Axis: anterior–posterior axis.

The cytochalasin D-treated embryos showed no sign of contractile polarity, indicating that the drug had reached the embryo. Cytoplasmic PIE-1 and PIE granules accumulated in the centre of the embryos, similar to embryos depleted of SPD-5 (**Figure 23**). The embryos were arrested in the cell cycle after NEBD.

The presence of a PIE-1 gradient in cytochalisin D treated embryos confirmed the *spd-5(RANi)* results, showing that polarity was not needed for the PIE-1 source formation but for its correct positioning.

2.4 PIE-1 nuclear localisation

2.4.1 Nuclear accumulation can occur equally in both pronuclei

PIE-1 showed strong nuclear localisation to the paternal pronucleus during most of the first cell division, whereas the maternal pronucleus showed weaker accumulation and only late in the cell cycle. First, I wondered if the nuclear accumulation of PIE-1 was specific to some molecular property of the paternal pronucleus, or rather whether the concentration of PIE-1 in the posterior cytoplasm biased nuclear accumulation to the nucleus in that compartment. Displacement of the maternal pronucleus to the posterior should address this question.

Therefore I centrifuged PIE-1::GFP expressing embryos to displace the maternal pronucleus and analysed the nuclear accumulation of PIE-1::GFP by time-lapse microscopy. The nuclear accumulation described the enrichment of nuclear PIE-1::GFP signal over the anterior cytoplasm.

In wildtype, the paternal pronucleus constantly accumulated PIE-1 and reached a peak enrichment of 2.3 fold at -3:30 relative to NEBD. From this time, the nuclear envelope started disassembling, and the nuclear concentration was not maintained. The maternal pronucleus accumulated its maximal PIE-1::GFP intensity about 1 minute later and only had a maximal enrichment of 1.5 fold. At 0:00 (NEBD), the nuclear PIE-1::GFP levels were equal to the anterior cytoplasm; the enrichment was lost (**Figure 24**).

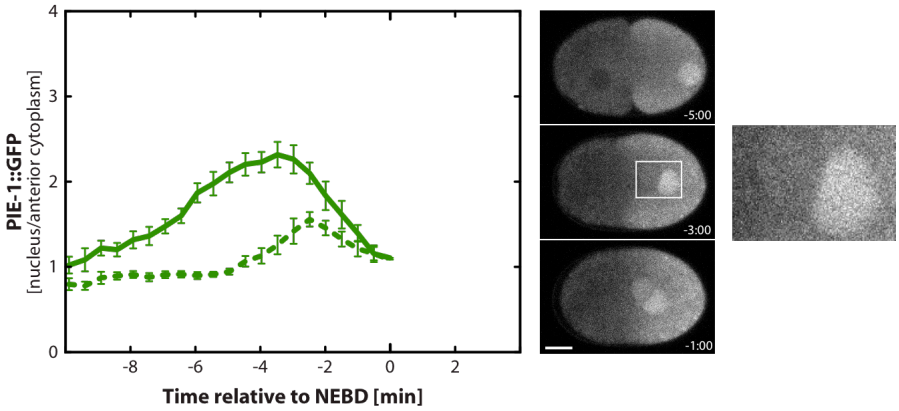

Figure 24: Nuclear accumulation of PIE-1 in wildtype embryos. The solid line represents the nuclear accumulation of PIE-1 in the paternal pronucleus, the dashed line in the maternal pronucleus (n=9). The time-lapse images show the nuclear accumulation. The nuclei at pronuclear meeting are magnified, at right. The scale bar represents 10 µm. Anterior is to the left.

The repositioning of the maternal pronucleus into the posterior cytoplasm by centrifugation resulted in similar timing and intensity of the nuclear accumulation of PIE-1::GFP in both pronuclei (**Figure 25**).

The nuclear accumulation of PIE-1::GFP seems to be controlled by cytoplasmic PIE-1::GFP.

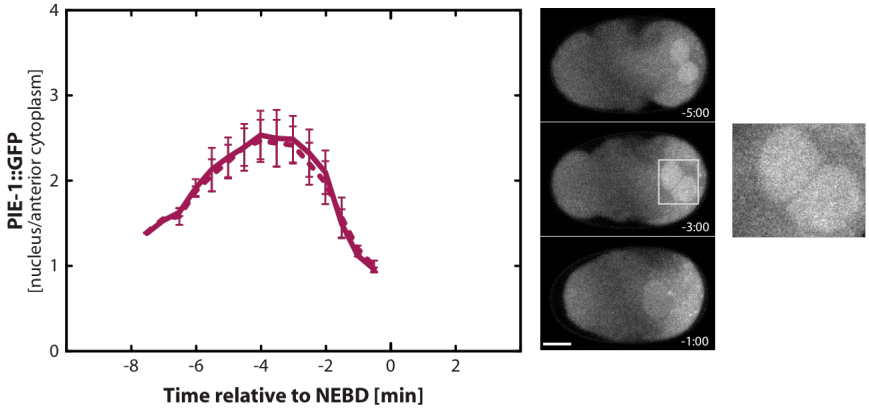

Figure 25: Nuclear accumulation of PIE-1 embryos after repositioning of the maternal pronucleus. The solid line represents the nuclear accumulation of PIE-1 in the paternal pronucleus, the dashed line in the maternal pronucleus (n=3). The time-lapse images show the nuclear accumulation. The nuclei at pronuclear meeting are magnified, at right. The scale bar represents 10 µm. Anterior is to the left.

2.4.2 Cytoplasmic PIE-1 level regulates the nuclear accumulation

Next I wanted to know what determined PIE-1's nuclear enrichment. To address this question, I lowered the protein amount of PIE-1 in *C. elegans* embryos by partial depletion of PIE-1, performed time-lapse microscopy and analysed the nuclear accumulation. The timing of the nuclear accumulation of PIE-1::GFP was similar to the control, but the

maximum nuclear enrichment was reduced in both pronculei. The maximal nuclear enrichment in the paternal pronucleus was 1.3-fold at -3:00 relative to NEBD (**Figure 26**). Less cytoplasmic PIE-1::GFP resulted in less PIE-1 accumulation in the pronuclei.

The cytoplasmic level and the time the pronuclei spent in the posterior cytoplasm appeared to determine the accumulation of PIE-1 in the pronuclei.

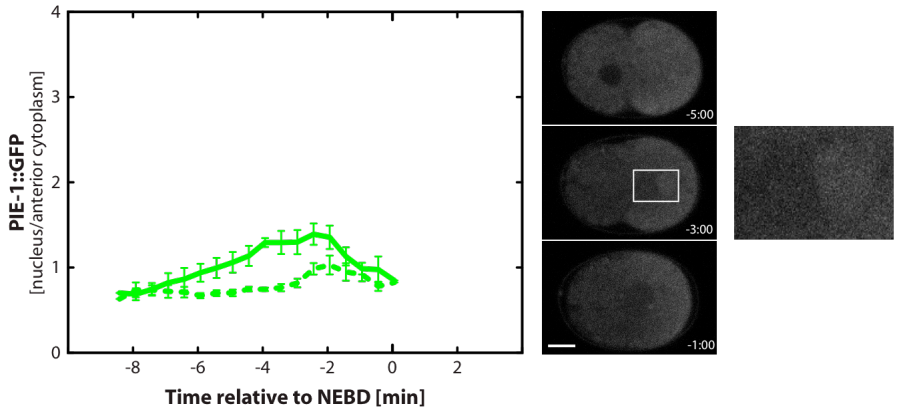

Figure 26: Nuclear accumulation of PIE-1 in *pie-1(partial RNAi)* embryos. The solid line represents the nuclear accumulation of PIE-1 in the paternal pronucleus, the dashed line in the maternal pronucleus (n=6). The time-lapse images show the nuclear accumulation. The nuclei at pronuclear meeting are magnified, at right. The scale bar represents 10 µm. Anterior is to the left.

2.4.3 Shape of the PIE-1 gradient does not depend on nuclear trapping

2.4.3.1 Nuclear import/export does not contribute to shape of gradient

In the fruit fly embryo, nuclear trapping might play a role in formation of the Bicoid morphogen gradient (Coppey et al., 2007). To investigate if a similar mechanism contributed to the PIE-1 gradient formation in *C. elegans* one-cell embryos, I impaired nuclear import and export and assessed the PIE-1 gradient shape. Specifically, I performed time-lapse microscopy of *imb-5(RNAi)* – import – and *ima-2(RNAi)* – export – embryos expressing PIE-1::GFP during the first cell division, and calculated the nuclear accumulation throughout the cell cycle and the decay constant λ at 0:00 (NEBD).

In *imb-5(RNAi)* embryos, the peak nuclear enrichment of PIE-1::GFP in the paternal and maternal pronuclei were much higher than in control embryos. The maximal nuclear enrichment in the control of 2.3-fold was reached at -10:00 relative to NEBD; more than 6 minutes earlier than in the control (-3:30 relative to NEBD).

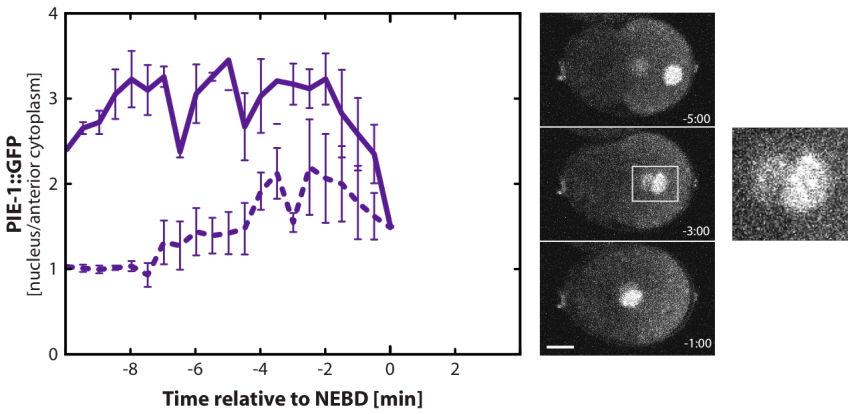

Figure 27: Nuclear accumulation of PIE-1 in *imb-5(RNAi)* embryos. The solid line represents the nuclear accumulation of PIE-1 in the paternal pronucleus, the dashed line in the maternal pronucleus (n=3). The time-lapse images show the nuclear accumulation. The nuclei at pronuclear meeting are magnified, at right. The scale bar represents 10 µm. Anterior is to the left.

I observed PIE-1::GFP puncta within the paternal pronucleus in *imb-5(RNAi)* embryos (**Figure 27**).

The calculated decay constant λ after IMB-5 depletion was not significantly different from the respective control (*imb-5(RNAi)*: 0.19 ± 0.01 EL, control: 0.18 ± 0.01 EL, p>0.83; **Figure 28 A**).

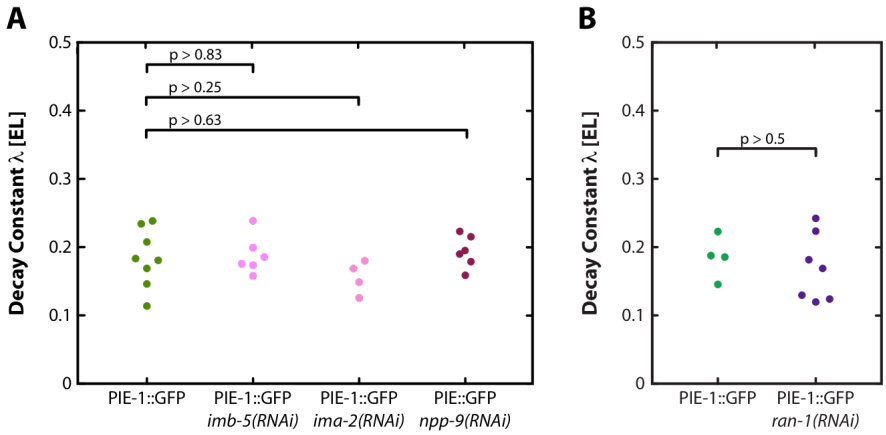

Figure 28: Shape of PIE-1 gradient is independent of nuclear accumulation. A) The average decay constant is 0.19 ± 0.01 EL in *imb-5(RNAi)* (n=6), 0.17 ± 0.02 EL in *ima-2(RNAi)* (n=4), 0.19 ± 0.01 EL in *npp-9(RNAi)* (n=6) and 0.18 ± 0.01 EL in the PIE-1 control embryos at 0:00 (NEBD) (n=6). **B)** The average decay constant for *ran-1(RNAi)* embryos at the equivalent cell cycle time of NEBD is 0.17 ± 0.02 EL (n=7); PIE-1 control 0.18 ± 0.02 EL (n=4). For statistical analysis an unpaired two-tailed student's t-test is used. EL: embryo length.

In *ima-2(RNAi)* embryos, the peak nuclear accumulation of PIE-1 in the paternal pronucleus was 2.8-fold enriched over the anterior cytoplasm at -3:00 relative to NEBD, compared to

2.3-fold in control embryos. The maximum accumulation of PIE-1 in the maternal pronucleus was similar to control levels. As in the IMB-5 depleted embryos, *ima-2(RNAi)* embryos showed altered temporal dynamics of nuclear PIE-1::GFP enrichment (**Figure 29**). The calculated decay constant λ of 0.16 ± 0.01 EL was not significantly different from the respective control (0.18 ± 0.01 EL, p>0.25; **Figure 28 A**).

Interfering with nuclear import and export altered the PIE-1 levels in both paternal and maternal pronuclei as well as the temporal dynamics of nuclear accumulation. However, the shape of the PIE-1 gradient at 0:00 (NEBD) was not changed after altering the PIE-1 nuclear accumulation by interfering with nuclear import and export.

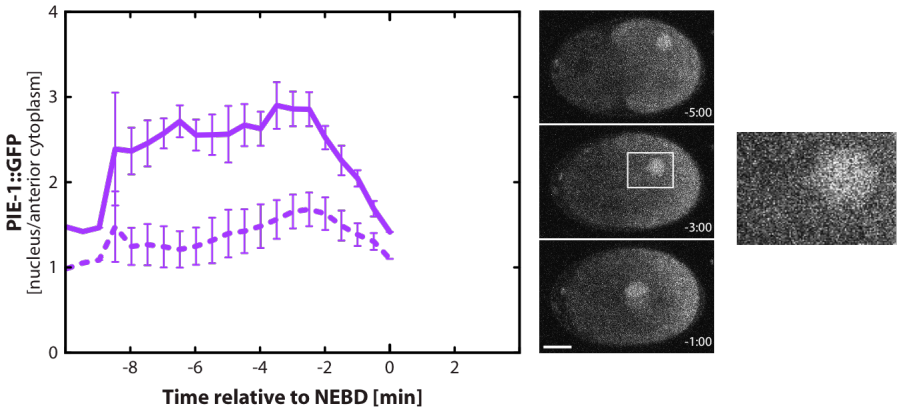

Figure 29: Nuclear accumulation of PIE-1 in *ima-2(RNAi)* embryos. The solid line represents the nuclear accumulation of PIE-1 in the paternal pronucleus, the dashed line in the maternal pronucleus (n=6). The time-lapse images show the nuclear accumulation. The nuclei at pronuclear meeting are magnified, at right. The scale bar represents 10 µm. Anterior is to the left.

2.4.3.2 The nuclear envelope is not necessary for gradient formation

In *imb-5(RNAi)* and *ima-2(RNAi)* embryos, the nucleus was still present and accumulated PIE-1. To try to further rule out any possible contribution of the nucleus to the PIE-1 gradient shape, I depleted embryos of the nuclear envelope component NPP-9, which resulted in a complete failure in nuclear envelope assembly (Askjaer et al., 2002). PIE-1::GFP expressing *npp-9(RNAi)* embryos were followed by time-lapse microscopy and analysed for the shape of the PIE-1 gradient. The calculated decay constant λ at 0:00 (NEBD) in *npp-9(RNAi)* embryos was not significantly different from the respective control (*npp-9(RNAi)*: 0.19 ± 0.01 EL, control: 0.18 ± 0.01 EL, p>0.63; **Figure 28 A**). Similar

results were obtained following RAN-1 depletion, where nuclear envelope formation was also prevented (Askjaer et al., 2002) (**Figure 28 B**).

The nuclear accumulation of PIE-1 seemed to be dispensable for shaping the PIE-1 gradient.

2.4.4 Nocodazole treatment abolishes nuclear accumulation

When I analysed the nocodazole-treated embryos (see 2.2.2), I observed no nuclear accumulation of PIE-1 in the paternal pronucleus although the cytoplasmic levels were similar to untreated control embryos. Only when the nuclear envelope became permeable (-3:30 relative to NEBD), PIE-1 entered the nucleus (**Figure 30**).

Depolymerising microtubules by nocodazole treatment prevented nuclear accumulation of PIE-1::GFP.

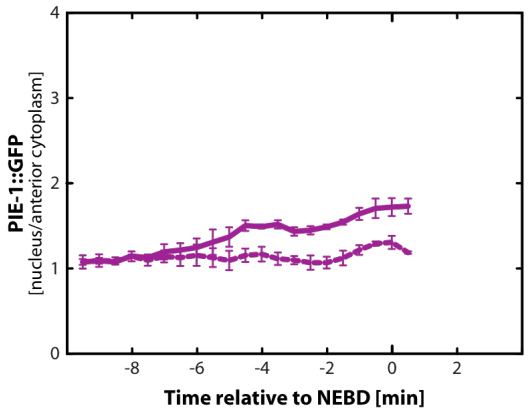

Figure 30: Nuclear accumulation of PIE-1 in nocodazole-treated embryos. The solid line represents the nuclear accumulation of PIE-1 in the paternal pronucleus, the dashed line in the maternal pronucleus (n=4).

For all RNAis and inhibitor experiments, I confirmed that the other parameters of PIE-1's asymmetry were not changed. In **Figure 31**, I show representative results of additional measurements such as posterior enrichment and PIE granule appearance for the nocodazole treatment:

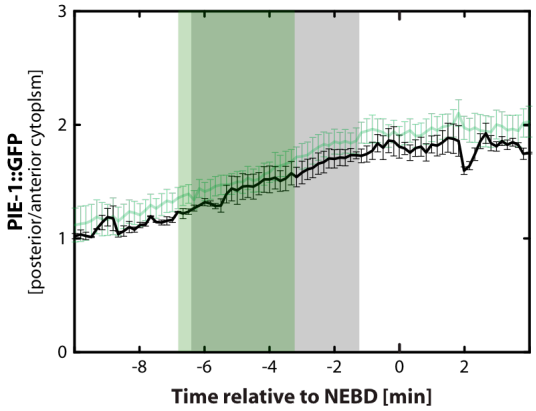

Figure 31: Nocodazole treatment does not effect posterior PIE-1 enrichment of the cytoplasm and PIE granules appearance. The cytoplasmic PIE-1 levels are displayed as the enrichment of PIE-1 in the posterior of nocodazole-treated embryos (n=4). The time window of PIE granule appearance is shaded gray. The measurements of untreated control embryos are in green (n=7).

2.5 PIE granule formation

2.5.1 Dynamics of PIE granule formation

Besides localising to the pronuclei and centrosomes, PIE-1 also associates with P granules (Mello et al., 1992). To investigate the dynamics of PIE-1 localisation to P granules, I analysed time-lapse images of PIE-1::GFP expressing embryos for the appearance of PIE-1 positive P granules, hereafter called PIE granules. The first evidence of PIE granules could be seen as a local increase of PIE-1::GFP intensity. The PIE granules accumulated more PIE-1::GFP and their shape became defined over time (**Figure 32**). The movement of the granules could be followed for at least 1 minute.

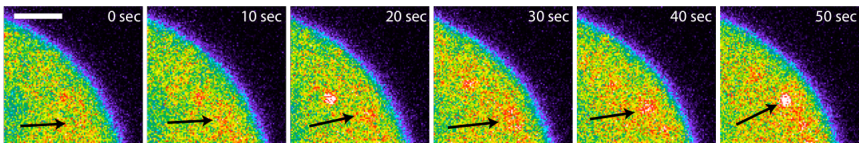

Figure 32: Appearance of PIE granules. Time-lapse series of the association of PIE-1::GFP with P granules (arrow). A region of the posterior cortex is shown. The images are pseudocoloured with red indicating the highest intensity and blue the lowest. The scale bar represents 5 µm.

2.5.2 Reduced PIE-1 levels delay PIE granule appearance

Next I wanted to know if the appearance of PIE granules correlated with the PIE-1::GFP levels of the surrounding cytoplasm. I timed the appearance of PIE granules in wildtype and *pie-1(partial RNAi)*. In wildtype embryos, PIE granules were detected between -6:30 and

-2:30 relative to NEBD (**Figure 32 A**). In contrast, the lower cytoplasmic PIE-1::GFP levels of *pie-1(partial RNAi)* embryos delayed PIE granule appearance by about 3 minutes. The PIE granules appeared between -3:00 and -0:30 relative to NEBD (**Figure 32 B**).

The low cytoplasmic PIE-1 level in embryos partially depleted of PIE-1 seemed to delay the appearance of PIE granules.

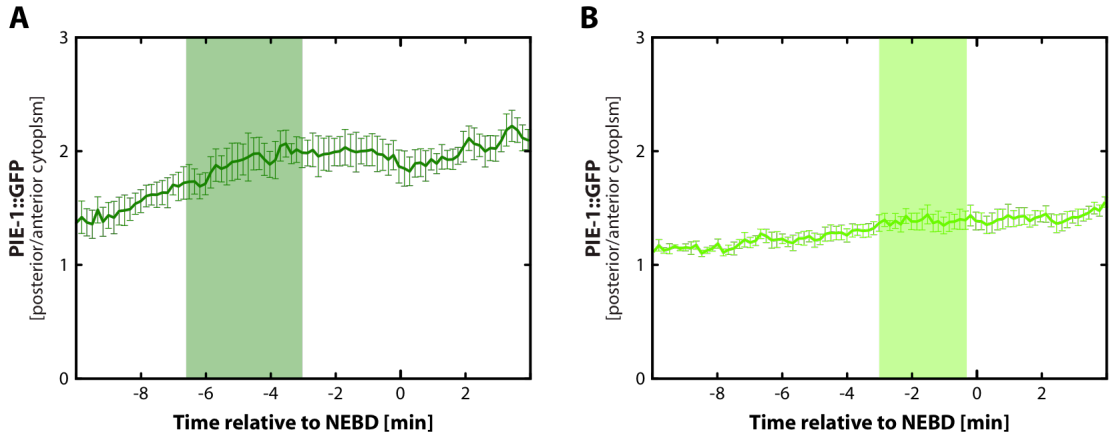

Figure 33: Low levels of cytoplasmic PIE-1 delay PIE granule appearance. The cytoplasmic PIE-1 levels are displayed as the enrichment of PIE-1 in the posterior. The time windows of appearing PIE granules are shaded green in control (**A**, n=16) and *pie-1(partial RNAi)* embryos (**B**, n=10).

2.5.3 Stabilisation of the PIE-1 gradient correlates with appearance of PIE granules

I next wanted to test if the formation of the PIE-1 gradient is related to PIE granule appearance. I tested this hypothesis by comparing the time of PIE-1 gradient formation and the time of PIE granule appearance in wildtype and *pie-1(partial RNAi)* embryos expressing. In 30 sec intervals, the PIE-1 gradient formation was analysed by the gradient shape (decay constant λ) and the goodness of the exponential fit to the PIE-1 intensity profile along the anterior–posterior axis (R^2 value). The R^2 value was used to assign the time at which the PIE-1 gradient became statistically exponential, using a cut-off of $R^2 \geq 0.75$.

During the early phase of polarity establishment (before -6:00 relative to NEBD) the gradient did not fit an exponential curve: the R^2 values were smaller than 0.75. Instead, the PIE-1 intensity profile was best fit by a line (data not shown). Around time -4:30 relative to NEBD, the PIE-1 gradient became statistically exponential ($R^2 \geq 0.75$). The R^2 values continued to increase during the cell cycle, meaning that the exponential PIE-1 gradient was

stabilised. The shape of the gradient was stable between -1:30 and +2:00 relative to NEBD, as indicated by stable decay constants λ. In wildtype embryos, PIE granules became detectable between -6:30 and -2:30 relative to NEBD. This was shortly before the exponential PIE-1 gradient became stable (**Figure 34 A**).

In *pie-1(RNAi)* embryos, PIE granules were detected between -3:00 and -0:30 relative to NEBD (**Figure 34 B**). The partial depletion of PIE-1 delayed the formation of the PIE-1 gradient by 2 minutes, which is consistent with the delayed appearance of the PIE granules.

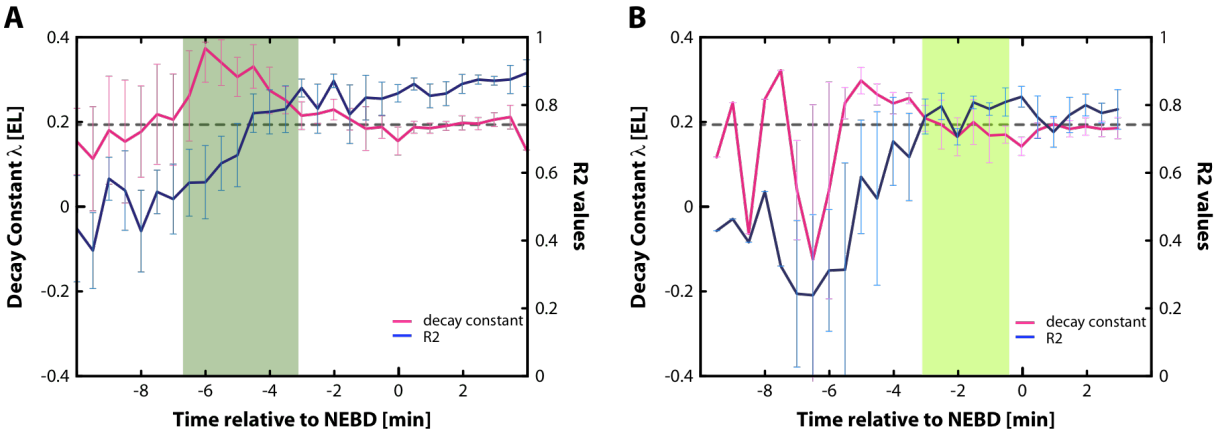

Figure 34: PIE-1 gradient forms later in *pie-1(partial RNAi)* embryos. Analysis of PIE-1 gradient formation by the shape of the gradient (decay constant λ, pink) and the goodness of the exponential fit to the PIE-1::GFP intensity profile along the anterior–posterior axis (R^2 value, blue) in control (**A**, n=10) and *pie-1(partial RNAi)* embryos (**B**, n=4). The dashed line indicates the cut-off value for exponential gradient formation ($R^2 \geq 0.75$). The time window of PIE granule appearance is shaded green. EL: embryo length.

These results showed that the appearance of PIE granules and the formation of the exponential PIE-1::GFP gradient are temporally correlated.

2.6 Molecular contributions to PIE-1 gradient formation

Several germline specific cell fate determinants show similar asymmetric segregation patterns as PIE-1. Those fate determinants are specific for cells of the P lineage and also associate with P granules. I wondered whether any of these other P lineage fate determinants were required for PIE-1 segregation.

2.6.1 Other cell fate determinants are required for PIE-1 asymmetry

To find out if P lineage fate determinates are necessary for the segregation of PIE-1, a candidate screen was performed by Sabina Sanegre Sans in the lab. POS-1, MEX-1, PGL-1, PAL-1 and SKN-4 were depleted by RNAi. The shape of the PIE-1 gradient as well was PIE granule size and number were analysed in worms expressing PIE-1::GFP.

A

RNAi	Decay constant λ	Number of P granules	Size of P granules
mex-1			
pos-1			
pgl-1			
pal-1			
spn-4			

PIE-1::GFP

B

RNAi	Decay constant λ	Number of P granules	Size of P granules
pie-1			
pos-1			
pgl-1			
pal-1			
spn-4	n/a	n/a	n/a

GFP::MEX-1

Figure 35: Summary of candidate screen in PIE-1::GFP (A) and GFP::MEX-1 (B) embryos. Red indicates results with significant changes, green with no significant changes.

MEX-1 depletion had a unique effect on all the parameters analysed in PIE-1::GFP worms, and thus I chose to further analyse the effects of MEX-1 depletion on PIE-1 gradient formation.

2.6.2 MEX-1 depletion lengthens the PIE-1 gradient

To determine how MEX-1 depletion affected the shape of the PIE-1 gradient, I performed time-lapse microscopy and calculated the decay constant λ in *mex-1(RNAi)* embryos expressing PIE-1::GFP at 0:00 (NEBD).

The intensity profile of PIE-1::GFP along the anterior–posterior axis showed a flatter gradient than the control (**Figure 36 A**). The depletion of MEX-1 changed the shape of the PIE-1 gradient significantly as determined by decay constant λ was significantly different from the control (*mex-1(RNAi)*: 0.20 ± 0.01 EL, control: 0.17 ± 0.01 EL, $p < 0.04$; **Figure 36 B**).

The shape of the PIE-1 gradient might be depended on MEX-1.

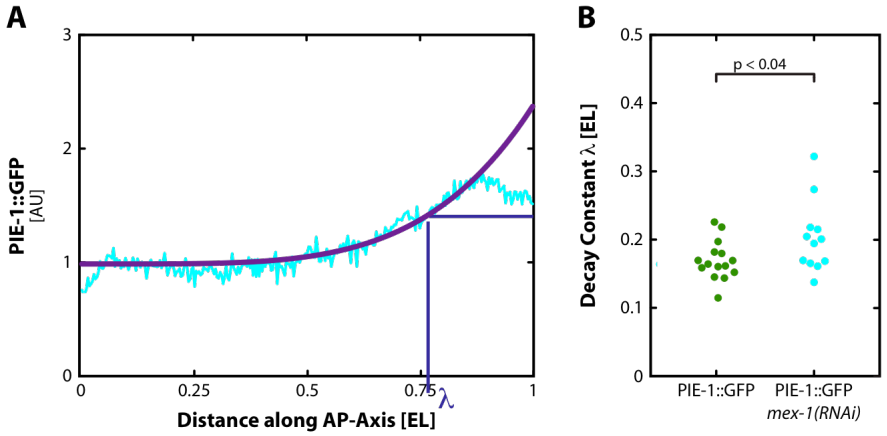

Figure 36: MEX-1 depletion changes shape of PIE-1 gradient. A) Intensity profile along the anterior–posterior axis of an one-cell *mex-1(RNAi)* embryo at 0:00 (NEBD). The blue line shows the fit exponential curve. The decay constant λ is calculated in EL from the source of the gradient. **B)** The average decay constant is 0.17 ± 0.01 EL in control (n=15) and 0.20 ± 0.01 EL in *mex-1(RNAi)* embryos (n=12). For statistical analysis an unpaired two-tailed student's t-test is used. AU: arbitrary units, EL: embryo length, AP-Axis: anterior–posterior axis.

2.6.3 MEX-1 depletion reduces size and number of PIE granules

The average number of PIE granules was another parameter analysed in the candidate screen. The PIE granules were counted in still images of *mex-1(RNAi)* embryos expressing PIE-1::GFP at 0:00 (NEBD) after applying an intensity threshold. I could detect PIE granules only in 4 of the 17 analysed images in *mex-1(RNAi)* embryos.

The average PIE granule number per embryo was significantly reduced in *mex-1(RNAi)* embryos (*mex-1(RNAi)*: 1.82 ± 0.80, control: 10.44 ± 0.80, p<0.001; **Figure 37 A**).

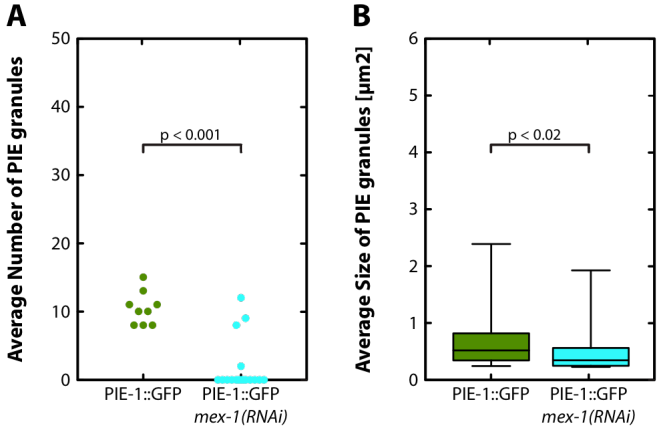

Figure 37: MEX-1 depletion decreased PIE granule size and number. A) The average PIE granule number per embryo is 10.44 ± 0.80 in the control (n=9) and 1.82 ± 0.93 in *mex-1(RNAi)* embryos expressing PIE-1::GFP (n=17). **B)** The average size of PIE granules per embryo in the control is 0.67 ± 0.05 µm^2 (n=9) and in *mex-1(RNAi)* 0.46 ± 0.06 µm^2 (n=17). For statistical analysis an unpaired two-tailed student's t-test is used.

After applying the intensity threshold, the area of PIE granules was determined. The average size of PIE granules per embryo after MEX-1 depletion was significantly lowered to the control (*mex-1(RNAi)*: 0.46 ± 0.06 µm^2, control: 0.67 ± 0.05 µm^2, p<0.02; **Figure 37 B**). MEX-1 might be needed for the association of PIE-1 to P granules, which could be the reason for the smaller number and size of PIE granules in *mex-1(RNAi)* embryos.

2.6.4 MEX-1 depletion delays formation of the exponential PIE-1 gradient

The shape of the PIE-1 gradient at 0:00 (NEBD) was slightly extended upon depletion of MEX-1 compared to controls. I therefore wanted to determine when MEX-1 affects the establishment of the exponential PIE-1 gradient. To address the question, I performed quantitative time-lapse microscopy of *mex-1(RNAi)* embryos during the first cell division. I analysed the PIE-1 gradient formation by the gradient's shape (decay constant λ) and goodness of the exponential fit to the PIE-1::GFP intensity profile along the anterior–posterior axis (R^2 value). I used the R^2 value to assign the time at which the PIE-1 gradient became statistically exponential $R^2 \geq 0.75$). Both values were calculated in 30 sec intervals.

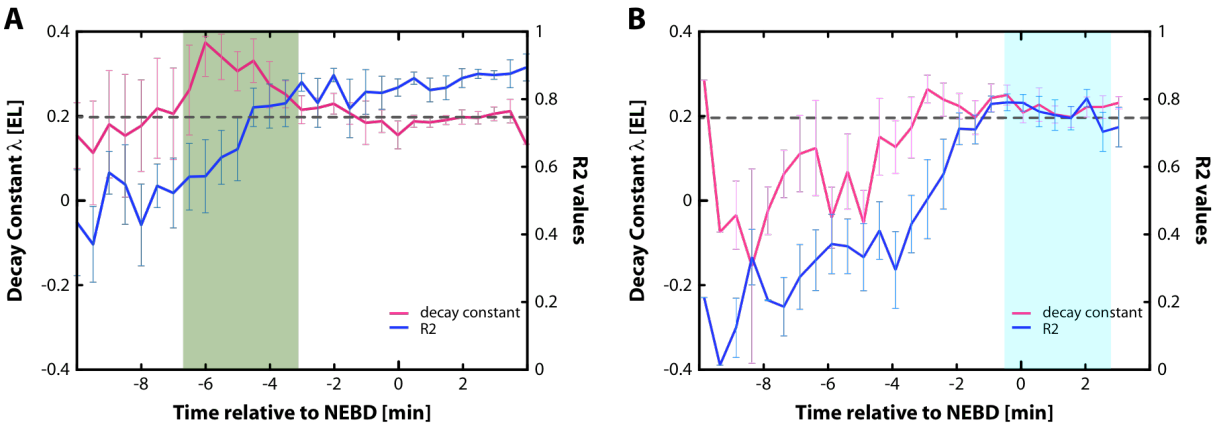

Figure 38: Delayed PIE-1 gradient formation upon MEX-1 depletion. Analysis of PIE-1 gradient formation by the shape of the gradient (decay constant λ, pink) and the goodness of the exponential fit to the PIE-1::GFP intensity profile along the anterior–posterior axis (R^2 value, blue) in control (**A**, n=10) and *mex-1(RNAi)* embryos (**B**, n=7). The dashed line indicates the cut-off value for exponential gradient formation ($R^2 \geq 0.75$). The time window of PIE granule appearance is shaded.

In comparison to the control, *mex-1(RNAi)* embryos formed the PIE-1 gradient at -1:30 relative to NEBD, which was a delayed the PIE-1 gradient formation by approximately 3 minutes (control: -4:30 relative to NEBD; **Figure 38**).

MEX-1 depletion impaired the timing of the exponential PIE-1 gradient formation, thus MEX-1 was needed for formation of the PIE-1 gradient.

2.6.5 PIE granule appearance and PIE-1 gradient stabilisation temporally correlate in MEX-1 depleted embryos

The analysis of PIE-1 gradient formation in wildtype embryos showed that the appearance of PIE granules correlated with the formation of an exponential gradient. To assign the time of PIE-1 gradient formation, I used the R^2 value, which was the goodness the exponential fit to the PIE-1::GFP intensity profile. The cut-off value was $R^2 \geq 0.75$.

To see whether the delayed formation of the exponential PIE-1 gradient after MEX-1 depletion was also correlated with later PIE granule appearance, I timed the PIE granules appearance in *mex-1(RNAi)* embryos. I could observe that PIE granules appear late in *mex-1(RNAi)* embryos, between -1:30 and +3:10 relative to NEBD. Most of the PIE granules appeared after 0:00, which explained why so few recordings showed PIE granules when counted at 0:00 (NEBD, **Figure 38 B**).

MEX-1 depletion delayed the appearance of PIE granules, which correlated with a delayed formation of the exponential PIE-1 gradient.

2.6.6 PIE granule appearance and low cytoplasmic levels of PIE-1 correlate in MEX-1 depleted embryos

To address the question if MEX-1 depletion also changes the cytoplasmic enrichment of PIE-1 in the posterior, I determined the ratio of cytoplasmic PIE-1 in the posterior and the anterior in time-lapse recordings of *mex-1(RNAi)* embryos expressing PIE-1::GFP. The maximum cytoplasmic PIE-1::GFP enrichment in the posterior in *mex-1(RNAi)* embryos was with 1.7-fold 20% lower than in the control. PIE granules appeared at a cytoplasmic enrichment of 1.5-fold at -1:00 relative to NEBD (**Figure 39**).

The lower cytoplasmic enrichment of PIE-1::GFP in the posterior was consistent with the later appearance of the PIE granules and the delayed formation of the exponential PIE-1 gradient.

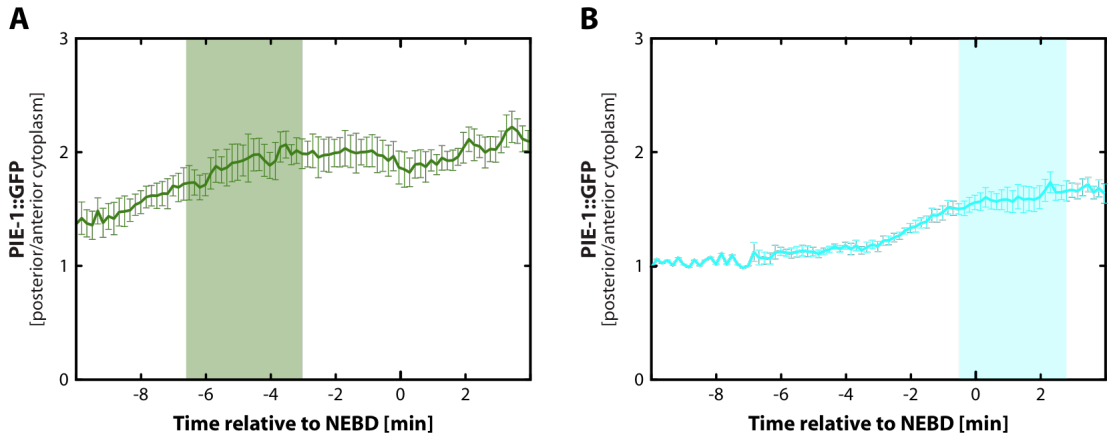

Figure 39: Delayed PIE-1 granule appearance in *mex-1(RNAi)* embryos. The cytoplasmic PIE-1 levels are displayed as the enrichment of PIE-1 in the posterior in control (**A**, n=7) and *mex-1(RNAi)* embryos (**B**, n=8). The time window of PIE granules appearance is shaded.

In control embryos, PIE granules appeared -6:30 and -2:30 relative to NEBD. At -6:30 relative to NEBD, the posterior cytoplasmic enrichment of PIE-1 was 1.5-fold. In *pie-1(partial RNAi)* embryos, PIE granules appeared between -3:00 and -0:30 relative to NEBD. The posterior cytoplasmic PIE-1 enrichment was 1.3-fold at -3:00 relative to NEBD. The effect of MEX-1 on PIE-1's ability to associate with P granules appeared to be at least partly independent of an affect on posterior cytoplasmic PIE-1 enrichment. My data suggests that there may be both concentration- and MEX-1-dependent contributions to PIE granule formation.

2.6.7 MEX-1 changes mobility of PIE-1::GFP

In a recent paper, the association of PIE-1 to P granules was proposed to slow the diffusion of PIE-1 in the posterior, which would contribute to the maintenance of the exponential PIE-1 gradient (Daniels et al., 2009).

MEX-1 seemed to be important for the formation of PIE granules. I wanted to test if the depletion of MEX-1 would change the mobility of PIE-1::GFP in the posterior of the embryo. Therefore I performed FRAP in *mex-1(RNAi)* embryos and determined the half-time recovery as a measure for the mobility of PIE-1::GFP (**Figure 40 A**). The depletion of MEX-1 significantly lowered the half-time recovery of PIE-1::GFP compared to control embryos ($p<0.01$; **Figure 40 B**), which meant that PIE-1::GFP was moving much faster in the posterior of the embryo.

The formation of PIE granules seemed to be important for determining the mobility of PIE-1, both of which were altered by MEX-1 depletion.

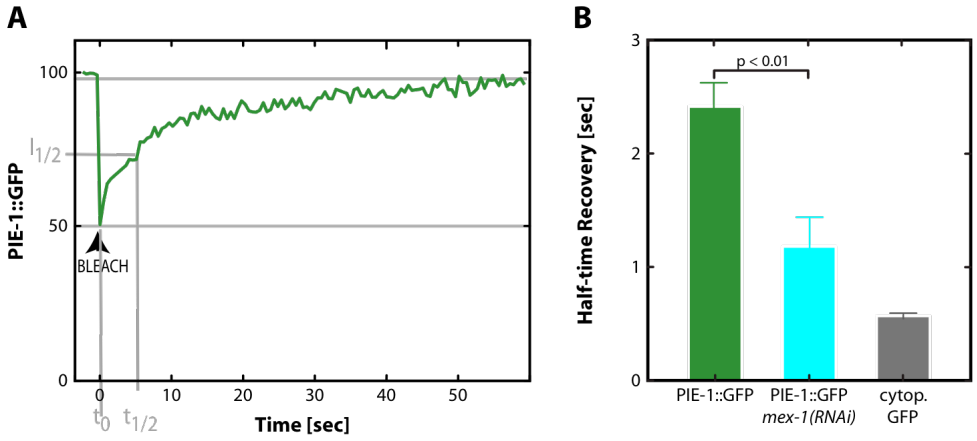

Figure 40: MEX-1 depletion increases PIE-1's mobility. A) FRAP curve and determination of the half-time recovery. **B)** Calculated half-time recoveries of PIE-1::GFP in PIE-1 control and *mex-1(RNAi)* embryos. For statistical analysis an unpaired two-tailed student's t-test is used.

2.6.8 MEX-1 is needed for formation of PIE granule intermediates

In a *F*luorescence *C*orrelation *S*pectroscopy (FCS) analysis of wildtype embryos, Daniels et al. (2009) found that PIE-1 appeared to be present in more than one population: a fast diffusing species that appears to represent free PIE-1, a slower diffusing species that may represent an aggregate or complexed form of PIE-1, and a very slow diffusing species that may reflect PIE-1 bound to P granules. The study further suggests that the fractions of each species vary along the anterior–posterior axis, such that in the posterior, the fast-diffusing species accounts for 30% of the total PIE-1, the slow-diffusing species 40%, and the very slow-diffusing species 30%. I wanted to test whether the depletion of MEX-1 would change the fractions of these different species or their diffusion properties. Therefore I depleted embryos of MEX-1 and measured the dynamics of single PIE-1::GFP molecules by FCS near the posterior cortex of the one-cell embryo.

The autocorrelation functions could be fit with a two-component anomalous diffusion model in three dimensions: PIE-1::GFP was present in the posterior cytoplasm as a fast and slow-diffusing component. This was in contrast to the three-component model used by Daniels et

al. (2009), but because addition of a third component did not significantly improve the fit of my data, I chose to use the simpler, two-component model (**Figure 41**).

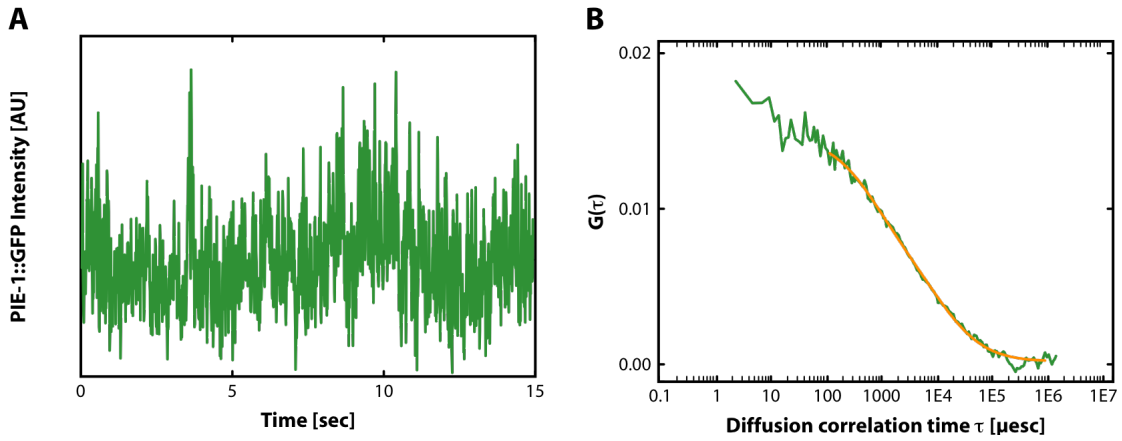

Figure 41: FCS data processing. A typical time course of PIE-1::GFP intensity fluctuations as measured by FCS (**A**) is converted into a PIE-1::GFP intensity autocorrelation function G(τ) (green line, **B**). The fit curve of the two-component anomalous diffusion model in three dimensions is shown in orange.

The diffusion correlation time measures the dwell time of GFP molecules within the confocal volume of the microscope and thus is directly related to the diffusion rate and inversely proportional to the diffusion coefficient, respectively. The diffusion correlation time of the fast component (3.55 ± 0.65 msec) was 20 times faster than the slow component (60.97 ± 8.26 msec) and accounted for about 56% of the entire PIE-1 protein in the posterior (**Figure 42 A**). The higher diffusion correlation time of the slow component suggested that the PIE-1 in this fraction is associated in complexes of a larger size than the PIE-1 species making up the fast component. The depletion of MEX-1 significantly increased the fraction of the fast-diffusing component (65 ± 2%, control: 56 ± 3%, $p<0.01$; **Figure 42 A**). In *mex-1(RNAi)* embryos, the average diffusion correlation time of the fast component was 1.30 ± 0.10 msec and that of the slow component was 32.24 ± 2.41 msec, both values significantly faster from the control (3.55 ± 0.65 msec, $p<0.01$; 60.97 ± 8.26 msec; $p<0.002$, respectively; Table 1).

To more precisely investigate how the difference in diffusion correlation times between wildtype and *mex-1(RNAi)* embryos arose, I analysed the frequency distribution of diffusion correlation times from individual FCS experiments. Wildtype embryos exhibited a wider

distribution of diffusion correlation times for both fast- and slow-diffusing components compared to MEX-1 depleted embryos (**Figure 42 B** and **C**). The heterogeneous correlation diffusion times suggested that PIE-1 was integrated into complexes of varying sizes. MEX-1 affected the formation of PIE-1 complexes of intermediate size, consistent with the increased proportion of fast-diffusion PIE-1 in *mex-1(RNAi)* embryos.

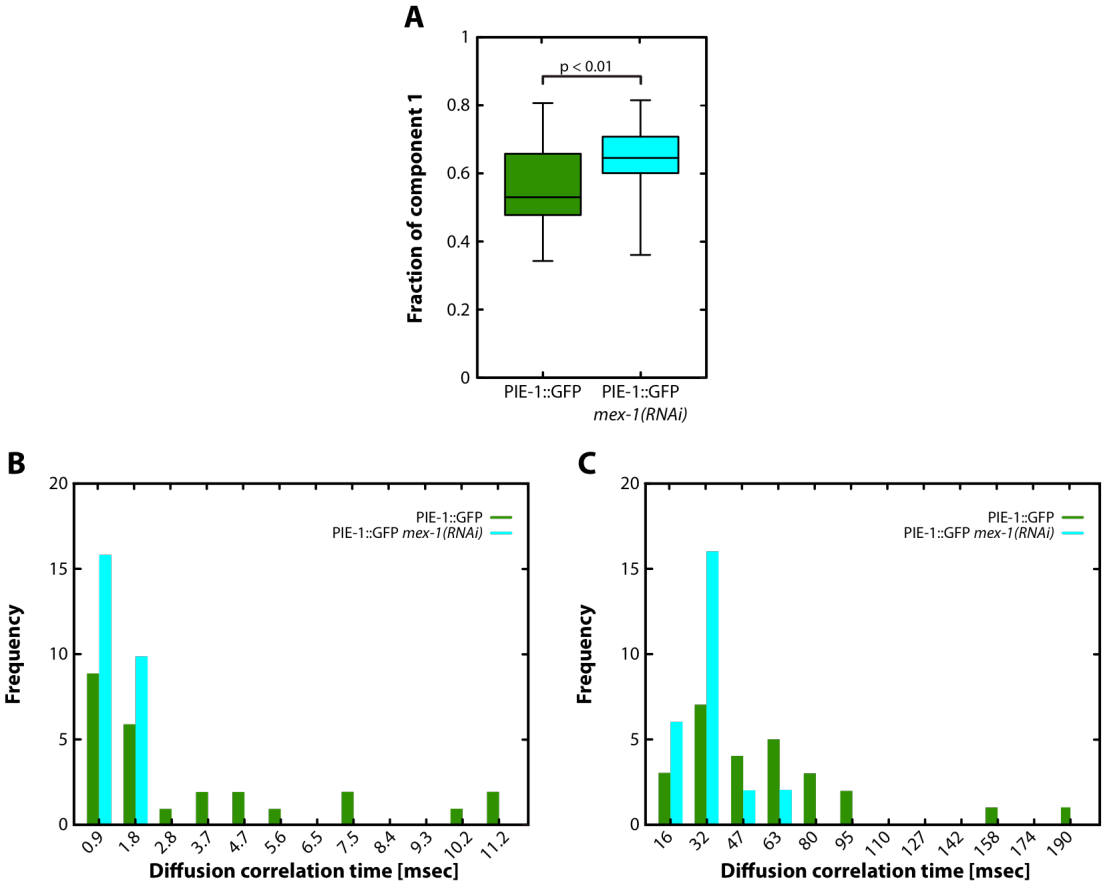

Figure 42: MEX-1 depletion changes PIE-1 intermediates. A) Fraction size of component 1 in control is 56 ± 2.6% (n=26) and *mex-1(RNAi)* 65 ± 2% (n=26). **B)** Histogram of diffusion correlation times of component 1 in control and *mex-1(RNAi)*. **C)** Histogram of diffusion correlation time of component 2 in wildtype and *mex-1(RNAi)*. For statistical analysis an unpaired two-tailed student's t-test is used.

Table 1: Calculations of apparent Diffusion coefficient D.

Particle	Diffusion correlation time [msec]	D [µm²/sec]
PIE-1::GFP, wildtype component 1	3.55 ± 0.65	3.66 ± 0.54
PIE-1::GFP, wildtype component 2	60.97 ± 8.26	0.17 ± 0.03
PIE-1::GFP, *mex-1(RNAi)* component 1	1.30 ± 0.10	5.92 ± 0.59
PIE-1::GFP, *mex-1(RNAi)* component 2	32.24 ± 2.41	0.23 ± 0.03

2.6.9 MEX-1 depletion changes the nuclear accumulation of PIE-1

While recording MEX-1 depleted embryos, I noticed that PIE-1::GFP seemed to accumulate in the maternal pronucleus earlier during the cell cycle than in wildtype embryos. Therefore I analysed *mex-1(RNAi)* embryos for the nuclear accumulation of PIE-1 (**Figure 43**).

The nuclear enrichments of both pronuclei increased by the same rate. The maximum enrichment of the paternal pronucleus in *mex-1(RNAi)* embryos was 2.0-fold over the anterior cytoplasm, within the range in control embryos. The nuclear enrichment of PIE-1 in the maternal pronucleus started at -6:00 relative to NEBD, about 2 minutes earlier than in the control (**Figure 24**).

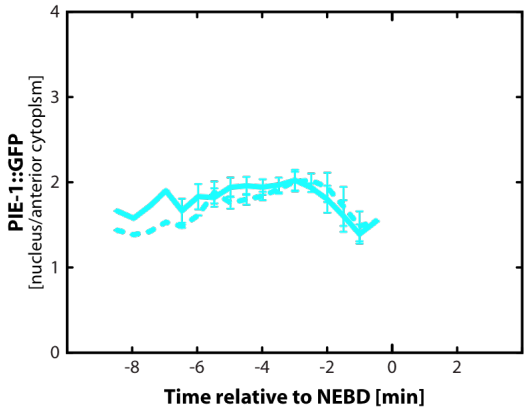

Figure 43: Nuclear Accumulation of PIE-1 in *mex-1(RNAi)* embryos. The solid line represents the nuclear accumulation of PIE-1 in the paternal pronucleus, the dashed line in the maternal pronucleus (n=4).

Because my previous studies indicated that the nuclear accumulation of PIE-1 depended largely on the cytoplasmic concentration of PIE-1 near the nucleus, one possible explanation of the earlier accumulation of PIE-1 in the maternal pronucleus in *mex-1(RNAi)* embryos is that MEX-1 depletion changes the level of cytoplasmic PIE-1 in the anterior.

2.7 ZIF-1 affects stabilisation of the PIE-1 gradient

Not much is known about PIE-1 interactions with other proteins. In order to identify potential interaction partners of PIE-1, a yeast-two-hybrid screen was performed commercially (Hybridgenics). The full-length cDNA of PIE-1 was used as pray, and the *C. elegans* embryonic library screened for robust interactors. The strongest candidates were:

*C. e*legans *h*omeobox (CEH)-3 protein, *p*oly-*A* *p*olymerase (PAP)-1, *p*rion-like (*Q*/*N*-rich) domain-bearing (PQN)-59 *p*rotein, *SR* protein related (RSR)-2 protein, *s*tress-*i*nduced *p*rotein (SIP)-1, *sy*napsis *d*efective (SYD)-9 protein, abnormal *t*hermo*tax*is (TTX)-1, *zi*nc-*f*inger interaction protein (ZIF)-1. C44H4.4 and K07E3.1 were two proteins of unknown function.

By testing all candidates for effects on the PIE-1 gradient formation by RNAi-mediated depletion, I found that several genes (ceh-37, sip-1, pap-1) gave a similar phenotype, namely reduced PIE-1 levels. The shape of the PIE-1 gradient and PIE granule appearance, however, were not affected. In contrast, *zif-1(RNAi)* embryos showed more pronounced PIE granules, and thus I focused on ZIF-1 for further analysis.

2.7.1 zif-1 mutants change the shape of PIE-1 gradient

The *zif-1(RNAi)* phenotype of was not very consistent, so I decided to use the mutant allele *zif-1(gk117)*, which deletes part of the promotor and the first exon of the gene (Checchi and Kelly, 2006).

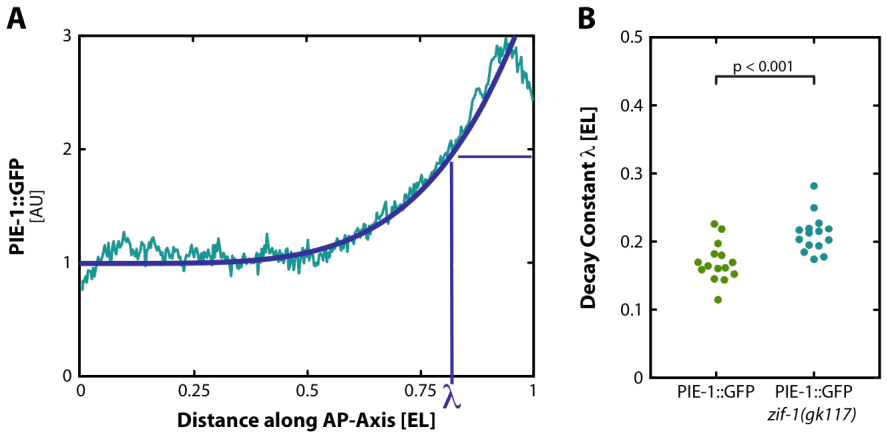

Figure 44: zif-1 mutants change PIE-1 gradient shape. A) Intensity profile along the anterior–posterior axis of a one-cell embryo at 0:00 (NEBD). The blue line shows the fit exponential curve. The decay constant λ is calculated in EL from the source of the gradient. **B)** Average decay constants are in PIE-1 control 0.17 ± 0.01 EL (n=15) and *zif-1(gk117)* embryos 0.21 ± 0.01 EL (n=15). For statistical analysis an unpaired two-tailed student's t-test is used. AU: arbitrary units, EL: embryo length, AP-Axis: anterior–posterior axis.

To determine whether deletion of ZIF-1 affected the shape of the PIE-1 gradient, I performed quantitative time-1apse recording of *zif-1(gk117)* embryos expressing PIE-1::GFP followed by calculation of the decay constant λ. The decay constant was significantly

different from the control (*zif-1(gk117)*: 0.21 ± 0.01 EL, control: 0.17 ± 0.01 EL, p<0.001; **Figure 36 B**).

The loss of functional ZIF-1 lengthened the PIE-1 gradient compared to wildtype. I observed the same phenotype after MEX-1 depletion. The decay constant λ was 0.20 ± 0.01 EL in *mex-1(RNAi)* embryo, which was not significantly different from zif-1 mutants (p>0.7, data not shown;).

2.7.2 zif-1 mutants do not affect the number and size of PIE granules

Next I wondered if the depletion of ZIF-1 changed the number or size of PIE granules. The PIE granules were counted in still images of *zif-1(gk117)* embryos expressing PIE-1::GFP at 0:00 (NEBD) after applying an intensity threshold.

The average number of PIE granules was not significantly different from the control (*zif-1(gk117)*: 10.67 ± 2.68, control: 10.40 ± 0.80, p>0.27; **Figure 45 A**).

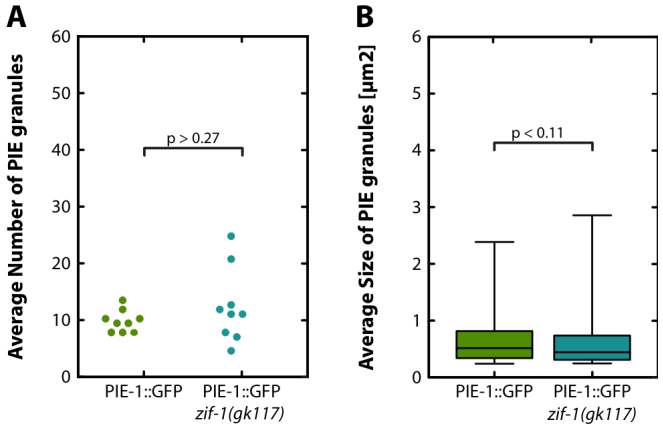

Figure 45: Average number and size of PIE granules are independent of ZIF-1. A) The average number of PIE granules at 0:00 (NEBD) is 10.40 ± 0.80 (n=9) in the PIE-1 control and 10.67 ± 2.68 (n=9) in *zif-1(gk117)* embryos. **B)** The average size of PIE granules is 0.67 ± 0.05 μm^2 (n=9) in control and 0.57 ± 0.4 μm^2 (n=9) in ZIF-1 mutant embryos. For statistical analysis an unpaired two-tailed student's t-test is used.

The same intensity threshold was used to determine the size of PIE granules in *zif-1(gk117)* embryos. The average size of PIE granules in *zif-1(gk117)* embryos was not significantly different from the control (*zif-1(gk117)*: 0.57 ± 0.4 μm^2, control: 0.67 ± 0.05 μm^2, p>0.11; **Figure 45 B**).

The depletion of ZIF-1 did not affect PIE granule formation.

2.7.3 Time of PIE granule appearance is unchanged in zif-1 mutants

Next I analysed the appearance of PIE granules. I quantified the time of PIE granule appearance in *zif-1(gk117)* embryos expressing PIE-1::GFP.

I could detect PIE granules during a similar time range as in the wildtype embryos, between -5:30 and -2:20 relative to NEBD. I could also see no difference in the posterior enrichment of cytoplasmic PIE-1::GFP in *zif-1(gk117)* mutants relative to the control. The maximum enrichment was about 2.5-fold (**Figure 46 A**).

2.7.4 zif-1 mutants promote the formation of the PIE-1 gradient

The shape of the PIE-1 gradient at 0:00 (NEBD) in *zif-1(gk117)* mutants was changed relative to controls. To answer the question if the kinetics of gradient formation was altered, I performed quantitative time-lapse microscopy of *zif-1(gk117)* embryos expressing PIE-1::GFP during the first cell division. The formation of the PIE-1 gradient formation was analysed by the shape of the gradient (decay constant λ) and goodness of the exponential fit to the Pie-1::GFP intensity profile along the anterior–posterior axis (R^2 value) in 30 sec intervals. I used the R^2 values to assign the time at which the gradient became statistically exponential, using 0.75 as the cut-off value.

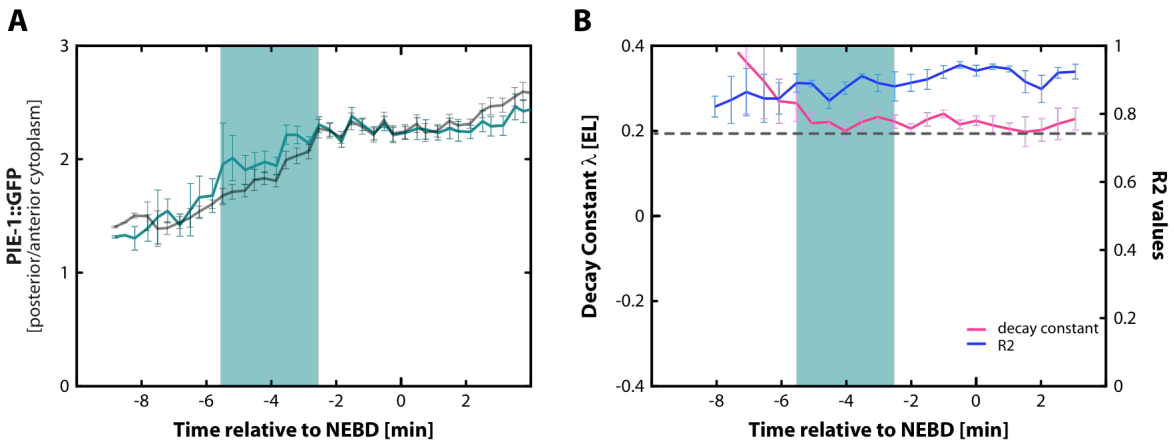

Figure 46: zif-1 mutants promote formation of PIE-1 gradient. A) The posterior enrichment of cytoplasmic PIE-1 in *zif-1(gk117)* embryos (n=6). The posterior enrichment in control embryos is in gray (n=10). **B)** Analysis of the PIE-1 gradient formation by the shape of the gradient (decay constant λ, pink) and the goodness of the exponential fit to the PIE-1::GFP intensity profile along the anterior–posterior axis (R^2 value, blue). The dashed line indicates the cut-off value for the exponential gradient formation ($R^2 \geq 0.75$). PIE-1::GFP expressing *zif-1(gk117)* embryos are analysed (n=6). The time window of PIE granule appearance is shaded. EL: embryo length.

The PIE-1 gradient was already exponential at -8:00 relative to NEBD, often the beginning of the recordings. Thus the exponential PIE-1 gradient was formed around 3 minutes earlier in zif-1 mutants relative to wildtype (-5:00 relative to NEBD, **Figure 46 B**).

The deletion of ZIF-1 seemed to promote the formation of the exponential PIE-1 gradient independently of the association of PIE-1 to PIE granules or overall levels of PIE-1.

2.7.5 Depletion of the SUMO-conjugating enzyme UBC-9 does not affect PIE-1 gradient shape

Another interaction partner of PIE-1 is the E2 *ub*iquitin-*c*onjugating enzyme (UBC)-9 (C. Mello, personal communication), which uses *s*mall *u*biquitin-*l*ike *m*odifier (SUMO) as a substrate (Jones et al., 2002). To test if UBC-9 contributed to the shape of the PIE-1 gradient, I depleted UBC-9 by RNAi. I performed quantitative time-lapse microscopy of *ubc-9(RNAi)* embryos expressing PIE-1::GFP and determined the decay constant λ at 0:00 (NEBD). The decay constant λ was not significantly different from the control (*ubc-9(RNAi)*: 0.18 ± 0.02 EL, control: 0.19 ± 0.02 EL, p>0.56; **Figure 47**).

Depletion of UBC-9 did not affect the shape of the PIE-1 gradient.

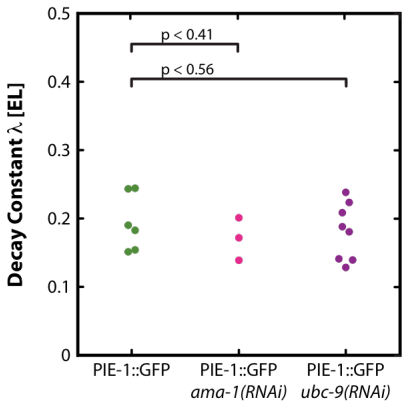

Figure 47: Shape of PIE-1 gradient is independent of UBC-9 and AMA-1. At 0:00 (NEBD), the average decay constants after UBC-9 and AMA-1 depletion are 0.18 ± 0.02 EL (n=8) and 0.17 ± 0.02 EL (n=3), respectively. The decay constant λ is 0.19 ± 0.02 EL in the PIE-1 control (n=6). For statistical analysis an unpaired two-tailed student's t-test is used. EL: embryo length.

2.7.6 Depletion of the large subunit of RNAPII AMA-1 does not affect PIE-1 gradient shape

PIE-1 is reported to compete with the CTD domain of RNAPII for binding to the CDK-9 (Zhang et al., 2003). In *C. elegans*, the *ama*nitin resistant (*ama*)-1 gene encodes the large subunit of RNAPII required for mRNA transcription. Depletion of AMA-1 by RNAi causes embryonic lethality at gastrulation (Powell-Coffman et al., 1996). To test if AMA-1 was needed for shaping the PIE-1 gradient, I performed quantitative time-lapse microscopy in *ama-1(RNAi)* embryos expressing PIE-1::GFP and determined the decay constant λ at 0:00 (NEBD). The decay constant λ was not significantly different from the control (*ama-1(RNAi)*: 0.17 ± 0.02 EL, control: 0.19 ± 0.02 EL, p>0.41; **Figure 47**).

Depletion of AMA-1 did not affect the shape of the PIE-1 gradient at NEBD.

2.8 MEX-1 forms an exponential concentration gradient

Given that MEX-1 influenced PIE-1 gradient formation and mobility, I next sought to determine the localisation of MEX-1. To gain information about the dynamic distribution of MEX-1, I performed quantitative time-lapse microscopy of embryos expressing GFP::MEX-1 (UE27) during the first cell division.

As previously reported, I observed the association of GFP::MEX-1 to P granules. In contrast to PIE-1, GFP::MEX-1 did not accumulate in the pronuclei throughout the cell cycle. MEX-1 also exhibited a non-P granule cytoplasmic localisation, similar to PIE-1. After the onset of polarity and expansion of the smooth domain, cytoplasmic GFP::MEX-1 intensity increased near the posterior cortex. At 0:00 (NEBD), cytoplasmic GFP::MEX-1 occupied half of the embryo. This asymmetry in MEX-1 localisation persisted through the first cell division. Thus, MEX-1 was only segregated to the P_1 cell (**Figure 48**).

I addressed the different aspect of cytoplasmic asymmetry with the following intensity measurements: The cytoplasmic distribution of GFP::MEX-1 was determined with the posterior–anterior ratio. MEX-1 was uniformly distributed at -9:00 (relative to NEBD), shortly after the onset of polarity establishment. GFP::MEX-1 became enriched in posterior

cytoplasm at -5:00 relative to NEBD. The maximal enrichment was 1.5-fold relative to the anterior (**Figure 49 B**).

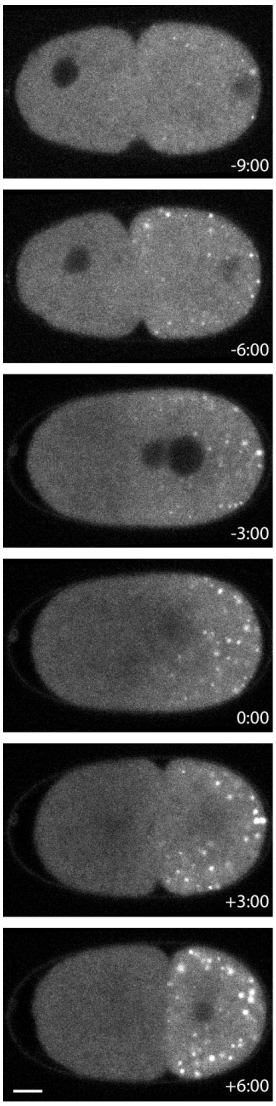

Figure 48: Time-lapse images of a one-cell embryo expressing GFP::MEX-1. The first cell division is shown. The scale bar represents 10 µm. The anterior is to the left.

At 0:00 (NEBD), the intensity profile of cytoplasmic GFP::MEX-1 was determined along the posterior–anterior axis. GFP::MEX-1 intensities were highest at the posterior pole and decreased along the embryo axis. GFP::MEX-1 intensities reached background levels around 0.4 EL. An exponential decay function could be fit to the GFP::MEX-1 profile (**Figure 49 A**). The decay constant λ was 0.14 ± 0.01 EL (**Figure 51 A**).

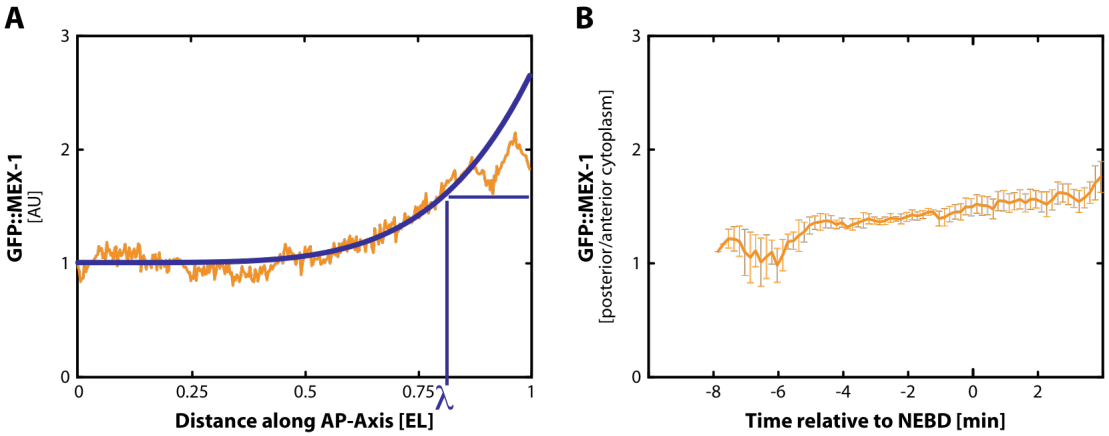

Figure 49: GFP::MEX-1 forms an exponential gradient. A) Intensity profile along the anterior–posterior axis of an one-cell embryo at NEBD. The blue line shows the fit exponential curve. The decay constant λ is calculated in EL from the source of the gradient. **B)** Posterior enrichment of cytoplasmic GFP::MEX-1 during the first cell cycle (n=8). AU: arbitrary units, EL: embryo length, AP-Axis: anterior–posterior axis.

2.8.1 MEX-1 levels accumulate independent of PAR-1

PIE-1 accumulation depends on PAR-1. I wanted to check if MEX-1 was controlled by a similar mechanism. I performed quantitative time-lapse microscopy of *par-1(RNAi)* embryos expressing GFP::MEX-1 during the first cell division and determined the levels of GFP::MEX-1 in the anterior and posterior cytoplasm. The region measurements showed that the cytoplasmic asymmetry of GFP::MEX-1 between the anterior and posterior was lost in *par-1(RNAi)* embryos: GFP::MEX-1 was uniformly distributed.

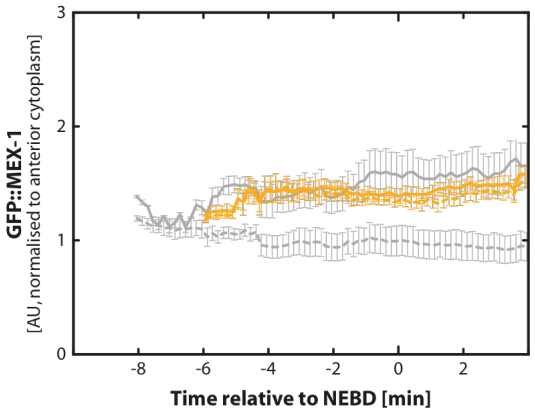

Figure 50: MEX-1 accumulates independent of PAR-1. Region measurements in MEX-1 control (gray, n=8) and *par-1(RNAi)* embryos expressing GFP::MEX-1 (orange, n=6). Measurements at the anterior (dashed line) and posterior pole of the embryo (solid line) are displayed. AU: arbitrary units

However, in contrast to PIE-1 in *par-1(RNAi)* embryos, GFP::MEX-1 intensities of the anterior and the posterior cytoplasm increased throughout the cell cycle in *par-1(RNAi)* embryos and reached the same level as the control (**Figure 50**).

The depletion of PAR-1 did not affect the production of MEX-1. PAR-1 was needed to position the source of the MEX-1 gradient to the posterior cortex.

2.8.2 PIE-1 depletion delays MEX granule appearance

In control GFP::MEX-1 embryos, MEX-1-positive P granules, hereafter referred to as MEX granules, were present at the beginning of each recording, around -8:00 relative to NEBD. The average number and size of MEX granules was determined at 0:00 (NEBD) after applying an intensity threshold. About 19.92 ± 1.17 MEX granules were present with an average size of 0.75 ± 0.03 µm^2 (**Figure 51 A** and **B**).

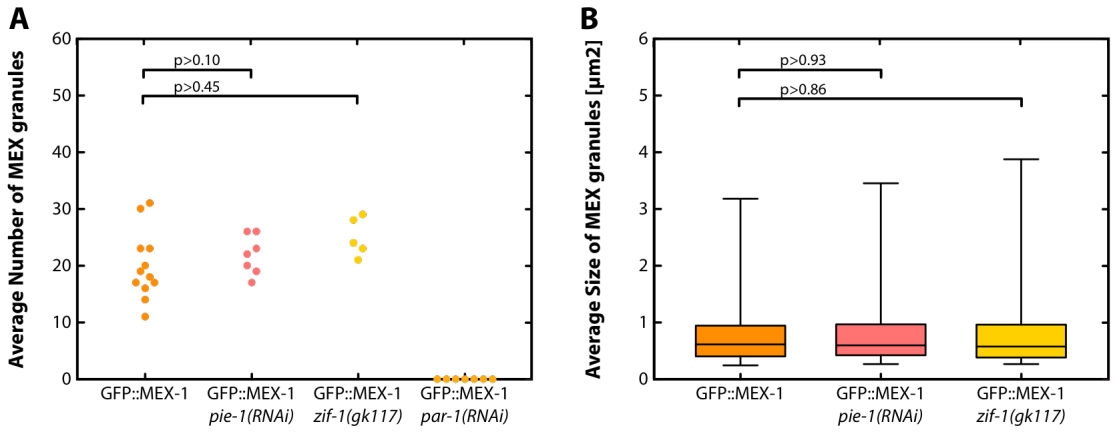

Figure 51: Average number and size of MEX granules. The average size and number of P granules are determined by an intensity threshold in embryos expressing GFP::MEX-1 at 0:00 (NEBD). **A)** The average number of MEX granules in control, *pie-1(RNAi)*, *zif-1(gk117)*, and *par-1(RNAi)* embryos is 19.92 ± 1.17 (n=12), 21.86 ± 1.51 (n=7), 25.00 ± 1.30 (n=5) and 0 ± 0 (n=7), respectively. **B)** The average size of MEX granules in control, *pie-1(RNAi)*, and *zif-1(gk117)* embryos is 0.75 ± 0.03 µm^2 (n=12), 0.74 ± 0.04 µm^2 (n=7), and 0.76 ± 0.05 µm^2 (n=7), respectively. For statistical analysis an unpaired two-tailed student's t-test is used.

To test whether depletion of PIE-1 altered the time of MEX granule appearance, I performed quantitative time-lapse recoding in *pie-1(RNAi)* embryos expressing GFP::MEX-1 during the first cell division. I quantitatively timed the appearance of MEX granules in *pie-1(RNAi)* embryos. In contrast to wildtype, and I could first detect MEX granules between -6:40 and -3:30 relative to NEBD (data not shown).

The depletion of PIE-1 delayed MEX granule appearance.

2.8.3 MEX granule size and number are independent of PIE-1

To answer the question if PIE-1 not only delayed the time of MEX granule appearance but also their number and size, I analysed MEX granules in still images of *pie-1(RNAi)* embryos expressing GFP::MEX-1 after applying an intensity threshold. Neither the average number (21.86 ± 1.51) nor size (0.74 ± 0.04 μm^2) of MEX granules in *pie-1(RNAi)* embryos was significantly different from the control (19.92 ± 1.17, p>0.45; 0.75 ± 0.03 μm^2, p>0.86, respectively; **Figure 51 A** and **B**).

2.8.4 PIE-1 has minor effect on MEX-1 gradient shape

To investigate if the delayed appearance of MEX granules affected the MEX-1 gradient shape, I analysed recordings of *pie-1(RNAi)* embryos expressing GFP::MEX-1 for the decay constant λ at 0:00 (NEBD). The decay constant λ in *pie-1(RNAi)* embryos was not significantly different from the control (*pie-1(RNAi)*: 0.18 ± 0.01 EL, control: 0.13 ± 0.01 EL, p>0.05; **Figure 52**).

PIE-1 has a minor effect on the shape of the MEX-1 gradient.

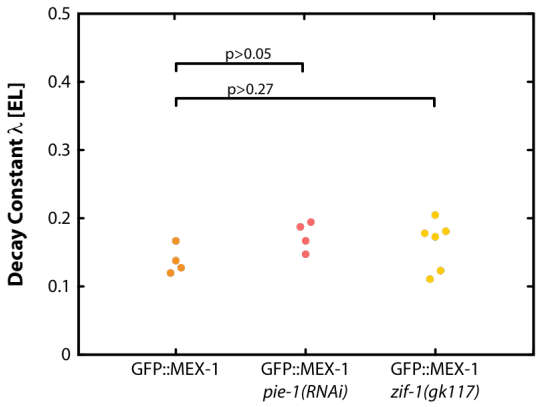

Figure 52: Shape of MEX-1 gradient is independent of ZIF-1 and PIE-1. A) The decay constant λ was determined in control, *pie-1(RNAi)*, and *zif-1(gk117)* embryos expressing GFP::MEX-1 as 0.13 ± 0.01 EL (n=4), 0.18 ± 0.01 EL (n=4), and 0.16 ± 0.02 EL (n=6), respectively. **B)** For statistical analysis an unpaired two-tailed student's t-test is used. EL: embryo length.

2.8.5 Kinetics of MEX-1 gradient formation are independent of PIE-1

To investigate if delayed appearance of MEX granules would have an effect on the temporal dynamics of MEX-1 gradient formation, I analysed recordings of *pie-1(RNAi)* embryos

expressing GFP::MEX-1 for MEX-1 gradient formation. I analysed the MEX-1 gradient formation by the shape of the gradient (decay constant λ) and the goodness of the exponential fit to the GFP::MEX-1 intensity profile (R^2 value). Both values were calculated in 30 sec intervals. I used the R^2 value to assigned the time at which the PIE-1 gradient became statistically exponential, using the cut of values of $R^2 \geq 0.75$.

In wildtype, the exponential MEX-1 gradient was established around -1:30 relative to NEBD. I used the decay constant λ for assessing the stability of the PIE-1 gradient shape. The shape of the MEX-1 gradient was never as stable as the PIE-1 gradient around 0:00 (NEBD; **Figure 53 A**) maybe due to the small number of analysed embryos. The depletion of PIE-1 only minorly changed the timing of exponential MEX-1 gradient formation (-1:00 relative to NEBD; **Figure 53 B**).

The formation of the MEX-1 gradient was largely independent of PIE-1.

Thus, there might be a hierarchy of fate determinant localisation, such that PIE-1 requires MEX-1 for accurate gradient formation but MEX-1 does not require PIE-1 to establish a gradient.

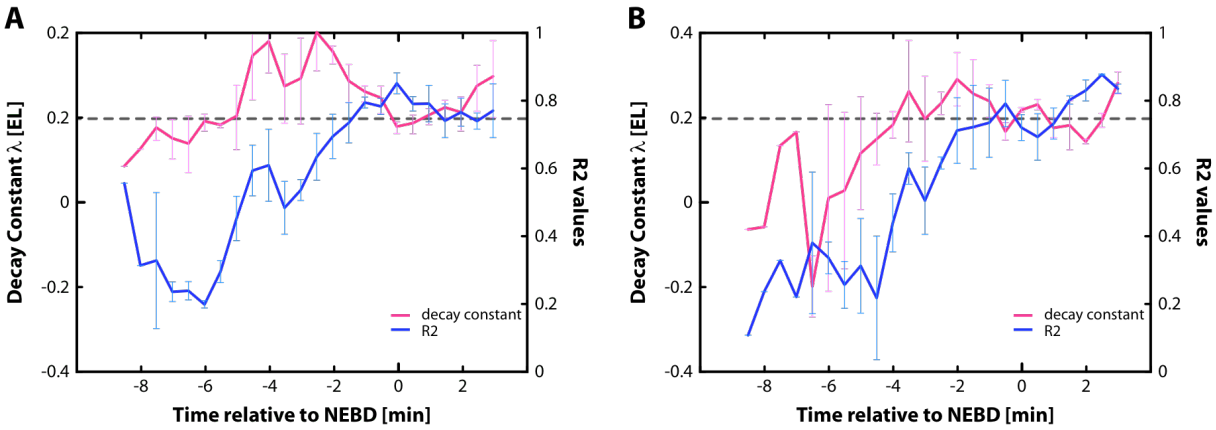

Figure 53: Formation of MEX-1 gradient is independent of PIE-1. Analysis of the PIE-1-gradient formation by the shape of the gradient (decay constant λ, pink) and the goodness of the exponential fit to PIE-1::GFP intensity profile along the anterior–posterior axis (R^2 value, blue) and in control (**A**, n=5) and in *pie-1(RNAi)* embryos expressing GFP::MEX-1 (**B**, n=3). The dashed line indicates the cut-off value for exponential gradient formation ($R^2 \geq 0.75$). EL: embryo length.

2.8.6 MEX-1 gradient forms independently of ZIF-1

The formation of the PIE-1 gradient was accelerated in zif-1 mutants. To find out if this was true for the formation of the MEX-1 gradient, I performed quantitative microscopy of

GFP::MEX-1;*zif-1(gk117)* embryos (UE25) during the first cell division. I determined the decay constant λ and the R^2 values in 30 sec intervals as a measure to access the formation of the MEX-1 gradient. The time, at which the exponential MEX-1 gradient stabilised, was similar in *zif-1(gk117)* and control embryos, occurring around -2:00 relative to NEBD (**Figure 54**).

Thus, zif-1 mutants did not affect the formation of the MEX-1 gradient.

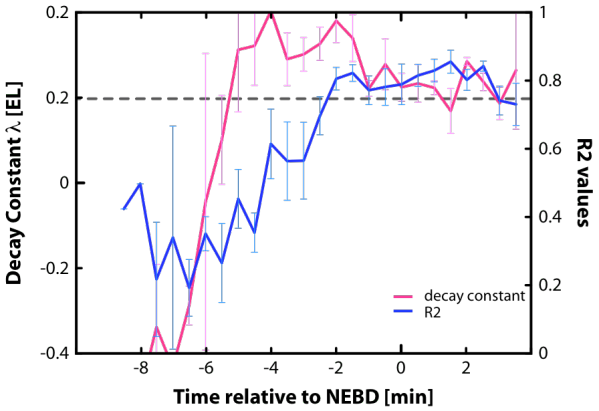

Figure 54: MEX-1 gradient formation independent of zif-1. Analysis of the PIE-1-gradient formation by the shape of the gradient (decay constant λ, pink) and the goodness of the exponential fit to PIE-1::GFP intensity profile along the anterior–posterior axis (R^2 value, blue). GFP::MEX-1 expressing *zif-1(gk117)* embryos are analysed (n=4). The dashed line indicates the cut-off value for exponential gradient formation ($R^2 \geq 0.75$). EL: embryo length.

2.8.7 MEX-1 granule assemble independently of ZIF-1

To test if the MEX granules appeared independently of ZIF-1, I timed the appearance of MEX granules in *zif-1(gk117)* embryos expressing GFP::MEX-1. Similar to the controls, MEX granules in *zif-1(gk117)* embryos were present already present at the beginning of each recordings, as early as -8:00 relative to NEBD.

Zif-1 mutants did not have an effect on the time of MEX granule appearance.

To check whether zif-1 mutants have an effect on other MEX granule properties, I determined the number and size of MEX granules in still images of *zif-1(gk117)* embryos expressing GFP::MEX-1 at 0:00 (NEBD) after applying an intensity threshold. The average number of MEX granules was 25.00 ± 1.30 and the average size was 0.76 ± 0.05 μm^2 in *zif-1(gk117)* embryos, neither of which was significantly different from in controls (19.92 ± 1.17, $p>0.45$; 0.75 ± 0.03 μm^2; $p>0.86$, respectively; **Figure 51**).

Thus the effect of ZIF-1 on stabilizing the cytoplasmic gradient appears to be limited to PIE-1.

2.9 P granules coalesce in the posterior

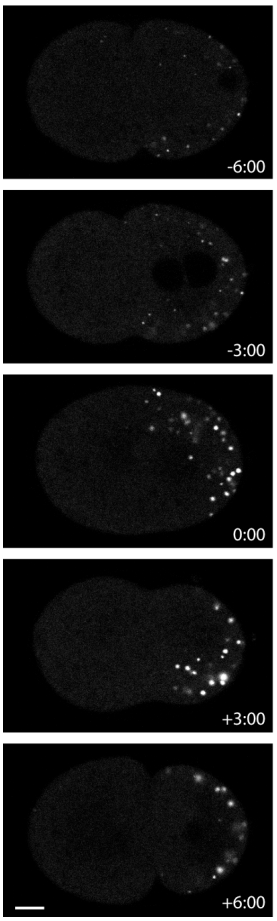

Figure 55: Time-lapse images of a one-cell embryo expressing GFP::PGL-1. The first cell division is shown. The scale bar represents 10 µm. The anterior is to the left.

Because of the apparent importance of P granule association of PIE-1 through MEX-1 in the establishment of a stable PIE-1 gradient, I wanted to better understand the dynamics of P granules in one-cell embryos. I performed quantitative time-lapse microscopy on embryos expressing GFP::PGL-1 (UE18), a constitutive component of P granules (Spike et al., 2008b).

As described previously (Kawasaki et al., 1998), during early stages of the first cell division, P granules were small and numerous in the cytoplasm. With cell cycle progression, fewer,

bigger and brighter P granules were observed. At 0:00 (NEBD), P granules occupied only the posterior half of the embryo only. GFP::PGL-1 was not found in the cytoplasm. The asymmetry in P granules persisted through cell division. Thus P granules segregation was restricted to the P_1 cell (**Figure 55**).

2.9.1 P granule number and size are independent of PIE-1 and MEX-1

To follow up on the idea that MEX-1 facilitates the association of PIE-1 to P granules, I wanted to check whether the number of P granules per se was altered due to depletion of MEX-1. Therefore I performed quantitative time-lapse microscopy of GFP::PGL-1 embryos depleted of MEX-1 during the first cell division. The average number of PGL-1 positive P granules was calculated after applying an intensity threshold. Depletion of MEX-1 did not alter significantly the number of P granules compared to controls (*mex-1(RNAi)*: 27.40 ± 3.45, control: 30.85 ± 3.08, p>0.4; **Figure 56 A**).

To confirm that P granule appearance does not rely on PIE-1, I depleted GFP::PGL expressing embryos of PIE-1 and recorded the first cell division by time-lapse microscopy. The number of P granules was counted at 0:00 (NEBD) after applying an intensity threshold to the images. The average number of P granules in *pie-1(RNAi)* embryos was not significantly changed in compared to control embryos (*pie-1(RNAi)*: 29.29 ± 3.09, control: 30.85 ± 3.08, p>0.7; **Figure 56 A**).

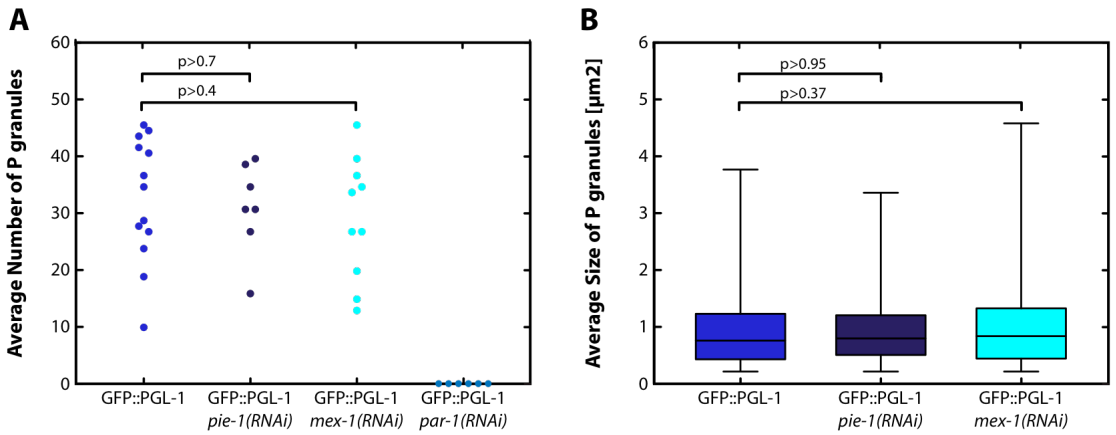

Figure 56: Average numbers and size of P granules in worms expressing GFP::PGL-1. A) The average numbers of P granules are determined by an intensity threshold at 0:00 (NEBD) for GFP::PGL-1 control, *pie-1(RNAi)*, *mex-1(RNAi)* and *par-1(RNAi)* embryos as 30.85 ± 3.08 (n=13), 29.29 ± 3.09 (n=7), 27.40 ± 3.45 (n=10) and 0 ± 0 (n=5), respectively. **B)** The average size of P granules in the control is 0.96 ± 0.04 µm^2 (n=13), after depletion of PIE-1 0.96 ± 0.04 µm^2 (n=7) and of MEX-1 1.02 ± 0.05 µm^2 (n=10). For statistical analysis an unpaired two-tailed student's t-test is used.

Additionally, I determined the size of P granules in worms expressing GFP::PGL-1. The depletion of neither PIE-1 nor MEX-1 changed the size of P granules significantly from the control (*pie-1(RNAi)*: 0.96 ± 0.04 μm^2, *mex-1(RNAi)*: 1.02 ± 0.05 μm^2, control: 0.96 ± 0.04 μm^2, p>0.9; p>0.3, respectively; **Figure 56 B**).

Depletion of PIE-1 and MEX-1 did not change the number and size of P granules in GFP::PGL-1 expressing worms.

2.9.2 Depletion of PAR-1 impairs P granules formation

PAR-1 depletion lowered the number of both MEX granules and PIE granules. To figure out if the formation of P granules was generally dependent on PAR-1, I analysed *par-1(RNAi)* embryos expressing GFP::PGL-1 using quantitative time-lapse microscopy of the first cell cycle. I determined the number of P granules at 0:00 (NEBD) after applying an intensity threshold to the images. No P granules were detected in GFP::PGL-1; *par-1(RNAi)* embryos, suggesting either granules were too small to be counted or below the intensity threshold I applied. Previous reports have found that PAR-1 depletion interferes with P granule size and number (Updike and Strome, 2009), which is consistent with my findings (**Figure 56**).

3 Discussion

My results show that PIE-1 forms an exponential concentration gradient in the *C. elegans* one-cell embryo at entry into mitosis. The gradient's source is located along the posterior cortex. The PIE-1 gradient seems to be shaped by diffusion rather than by cytoplasmic flows, active processes like microtubule-based transport, or nuclear trapping. Protein synthesis near the posterior PAR domain and protein degradation in the anterior half of the embryo may contribute to the exponential shape of the PIE-1 gradient. The anterior PAR complex and PAR-2 ensure the correct posterior positioning of the PIE-1 source and subsequently the cytoplasmic asymmetric localisation of PIE-1. PAR-1 is essential to generate a PIE-1 source at the posterior cortex. PIE-1 associates to P granules. The appearance of PIE-1 positive P granules, PIE granules, might help shape the PIE-1 gradient and maintain its properties in varying conditions, such as changes in PIE-1 protein levels or embryo size. ZIF-1 might be involved in a mechanism counteracting the PIE-1 gradient formation while germline cell fate determinant MEX-1 restricts the spread of the PIE-1 gradient and stabilises it. MEX-1 itself forms also an exponential concentration gradient with the source at the posterior cortex. PAR-1 seems to be responsible for the correct positioning of the MEX-1 gradient.
This PIE-1 gradient achieves an asymmetric distribution of cytoplasmic PIE-1 and ensures the exclusive segregation of PIE-1 to P_1.

3.1 Gradient formation

A basic question in developmental biology is what makes cells take on one particular cell fate in one part of the embryo and those elsewhere adopt another? This developmental pattering is regulated on spatial and temporal level: When and where cell fates are determined. Mathematics has been used to describe this formation of these patterns. The concept of morphogens, as a substance that changes cell fate in a concentration-dependent manner was introduced by Turing in 1952 (Turing, 1952). He used a reaction-diffusion model, which could describe the stable formation of a pattern from initially randomly distributed morphogens. In cells close to the gradient source, genes are expressed that need a high concentration of the gradient, while in cells further away from the gradient start

expressing genes in response to lower concentration of the morphogen. A steady-state morphogen gradient can be reduced to the following four parameters: production, rate of diffusion, degradation and immobile fraction (Kicheva et al., 2007). For each morphogen, all these parameters determine its specific shape. Conceptually, a morphogen gradient is the simplest way of spatial patterning (Lewis, 2008).

3.1.1 Gradients in tissues

In the development of embryos, most morphogen gradients patterns tissues and have to travel over several cell diameters. The development of the wing in Drosophila larvae is an excellent system for studying morphogen gradients. Here, the patterning of the wing margins of the wing, vein patterns and growth of the wing are organised by morphogens (O'Connor et al., 2006). I will compare the formation of Wingless and Decapentalegic morphogen gradients:

Wingless, a secreted member of the Wingless/Int-1 (Wnt) family is reported to be a morphogen that is involved in forming the margins of the wing (Strigini and Cohen, 2000). It is known for its short-range gradient (Diaz-Benjumea and Cohen, 1994). The bone morphogenic protein (BMP) family member Decapentalegic (Dpp) forms a long-range gradient that spreads throughout the wing disc regulating the size of the wing (Entchev et al., 2000; Tabata, 2001).

Kicheva et al. (2007) measured the four parameters for the Wingless and Dpp gradient: Fast degradation, faster mobility and less constantly bound protein shaped the short-range Wingless gradient. In contrast, Dpp degradation was slow, the immobile fraction was big and the protein was slow-diffusing. These parameters shape the long-range Dpp gradient.

What processes controls diffusion rate in a tissue? As secreted proteins morphogens can move through the extracellular space but sole movement by free diffusion would not form the characteristic morphogen concentration gradient (Entchev et al., 2000). Restricted morphogen diffusion in the extracellular space might be more suitable. Interactions with the extracellular matrix or morphogen receptors could slow the motion (Tabata, 2001; Yu et al., 2009). Transport of morphogens by planar transcytosis, cytonemes and argosomes are

observed in wing disc development: In planar transcytosis repeated cycles of endocytosis and resecretion transport the morphogen for cell to cell (Entchev et al., 2000; Kicheva et al., 2007). For instance, in the case of Dpp, it has been postulated that Dpp the gradient is formed by dynamin-mediated transcytosis (Entchev et al., 2000).

Cells form actin-based long protrusion, cytonemes, which contact the cells expressing the source of the gradient (Ramírez-Weber and Kornberg, 1999). Agrosomes are vesicles of fragmented basolateral membrane, which transport the morphogen to neighbouring cells (Greco et al., 2001).

All these are possibility how the diffusion of proteins is restricted to shape a gradient. For the fine-tuning of a morphogen gradient all four parameters (production, degradation, diffusion and immobile faction) are needed to make a robust system to pass on spatial information as needed in e.g. patterning of the wing

3.1.2 Gradient in single cells

The Bicoid gradient in the *Drosophila* embryo is one of the few examples of an intracellular morphogen gradient, which is set up in one big cell. The early *Drosophila* embryo is a syncytium, where the nuclei are uniformly localised along the cortex. During oogenesis, the Bicoid mRNA is produced in the neighbouring nurse cells, transported across the plasma membranes and placed at the anterior pole (Riechmann and Ephrussi, 2004). After fertilisation, transcription of the Bicoid mRNA is initiated in the *Drosophila* embryo (Driever and Nüsslein-Volhard, 1988a). Bicoid protein diffuses away from the site of synthesis and forms a gradient that organised the anterior–posterior axis of the embryo (Driever and Nüsslein-Volhard, 1988a). Bicoid is a transcriptional repressor by controlling the expression of zygotic gap genes that specify the different regions within the embryo. Bicoid forms a spatial concentration gradient to which cells respond at different threshold concentrations (Driever and Nüsslein-Volhard, 1989). Depending on the position in the morphogen gradient, cells of the syncycial embryo start gene expression of zygotic genes that set up the different segments in the embryo (Driever and Nüsslein-Volhard, 1988b).

What shapes Bicoid gradient? Mathematical modelling of different scenarios show that simple diffusion of Bicoid through the cytoplasm is not able to form a concentration gradient (Gregor et al., 2007). Gregor et al. (2007) developed a model in which the Bicoid gradient is formed by local production of Bicoid in the anterior, diffusion and uniform degradation. Within this model, the degradation of Bicoid ensures the stability of the gradient that would otherwise spread out to occupy the whole embryo instead. A more recent paper questions the contribution of the degradation, as the rate of Bicoid degradation has not been experimentally determined. Instead, Coppey et al. (2007) develop a model that suggests a trapping function of the nuclei, which would limit Bicoid diffusion and maintain the gradient.

A recent model suggests that the protein Bicioid gradient is prefigured by an mRNA gradient (Spirov et al., 2009): Despite the similar shapes of both gradients, the Bicoid mRNA gradient is not likely to be formed by diffusion. Ribonucleoprotein complexes of bicoid mRNA and Staufen is formed, which travel along microtubules driven by the concentration difference (Weil et al., 2006). This mRNA gradient is set up before the nuclei migrate to the cortex of the embryo. The amount of Bicoid that is taken up by the nuclei depends on their position in the Bicoid gradient.

How can a stable PIE-1 gradient be established in the *C. elegans* one-cell embryo? As in all other model systems, there is a PIE-1 source, which seems to be located along the posterior cortex. There is diffusion of PIE-1 in the cytoplasm away from the source. The interaction with P granules could change the diffusion parameters of PIE-1. The existence of an immobile PIE-1 fraction is at present not known. There is the possibility however that an immobile fraction of PIE-1 could be bound to P granules. Finally, the degradation in the anterior completes the shaping of the PIE-1 concentration gradient. In the next section I will discuss all four parameters essential for gradient formation separately.

3.2 The PIE-1 source

3.2.1 Positioning of the source

The PAR proteins at the cortex of the embryo are key regulators of polarity in the one-cell embryo. Their depletion leads to symmetric cell division as well as a failure in generating the founder cells of the cell lineages (Kemphues et al., 1988). According to PAR polarity, cell fate determinants are asymmetrically segregated, which results in different cell fates.

What are the roles of PAR proteins in PIE-1 source positioning? The PIE-1 source is the place of the highest cytoplasmic PIE-1 level. The anterior and posterior PAR protein complexes seem to have distinct roles in organising the PIE-1 source positioning. The loss of any of anterior PAR complex proteins allows positioning of the PIE-1 source along the entire cortex. The "rim" of high cytoplasmic PIE-1::GFP intensity, which can be seen at the cortex after depletion of the anterior PAR complex, might be an initial PIE-1 source, which becomes bigger and spreads with progression of the cell cycle. So, the anterior PAR complex restricts the PIE-1 source to the posterior.

PAR-2 is initially not needed for the positioning of PIE-1 source. Later in cell division PAR-2 is required for PIE-1 asymmetry by preventing localisation of the anterior PAR complex to the posterior cortex. There might be an additional role for PAR-2 in PIE-1 source positioning as cytoplasmic PIE-1 is lost along the cortex when the anterior PARs re-enter the posterior cortex during polarity maintenance phase (Cuenca et al., 2003).

What happens to the PIE-1 source if polarity is not established? In *spd-5(RNAi)* or cytochalasin D-treated embryos, the PIE-1 source locates to the centre of one-cell embryos instead of along the posterior cortex. The treatment leads to inhibition of polarity establishment (Hill and Strome, 1990). The prevention of contractile polarity in the one-cell embryo allows the anterior PAR complex proteins to remain uniformly along the cortex. The anterior PAR complex may prevent the PIE-1 source from forming in the vicinity of the cortex, which leaves the centre of the as the only possibility for PIE-1 source location.

3.2.2 PAR-1 and the PIE-1 source formation

While anterior PARs and PAR-2 are involved in source positioning, depletion of PAR-1 by RNAi shows a different phenotype: the cytoplasmic level of PIE-1 was depleted. Thus PAR-1 might contribute to PIE-1 gradient by forming the PIE-1 source. The PIE-1 source is defined as the position within the one-cell embryo of highest cytoplasmic PIE-1 levels. High levels of cytoplasmic PIE-1 could be achieved by local protein synthesis, local release of newly folded protein or even stabilisation of present protein. Additionally, the local protection from degradation or trapping of the protein could cause in formation of a protein source. For example, in *Drosophila* embryos, the local protein synthesis of Bicoid lead to the formation of a local protein source (Driever and Nüsslein-Volhard, 1988a).

How could PAR-1 contribute to the formation source of the PIE-1 gradient? PAR-1 is a serine/threonine kinase of the highly conserved *m*icrotubules *a*ffinity *r*egulating *k*inase (MARK) family. In mammals, these kinases control the stability of microtubules by phosphorylation certain microtubule-associated proteins (Drewes et al., 1997). MARK signalling affects the polarity e.g. in neurons and their cell differentiation (Matenia and Mandelkow, 2009). In the early *Drosophila* embryo, PAR-1 plays an important role in regulation of the local mRNA accumulation of the morphogen *oskar*, which organises the posterior of the embryo. By controlling the nucleation of the microtubules in this way that the plus-ends point towards the posterior of the oocyte (Cha et al., 2001), *oskar* mRNA is transported in a kinesin-dependent process to the posterior pole (Brendza et al., 2000). Additionally, Oskar protein is stabilised by PAR-1-dependent phosphorylation in the posterior cytoplasm (Riechmann and Ephrussi, 2001). Oskar in turn restricts PAR-1 to the posterior and thus amplifies the microtubule nucleation by a positive feedback loop (Zimyanin et al., 2007).

PAR-1 kinase activity is needed for polarity establishment. Mutations in the kinase domain result in embryonic lethal (Guo and Kemphues, 1995). In *C. elegans* however, no target for PAR-1 phosphorylation has been identified. Speculations suggest a role for PAR-1 in regulation of mRNA localisation as P granules are fewer in the posterior in par-1(-) mutants (Goldstein and Macara, 2007). The presence of fewer and smaller P granules could influence

the PIE-1 protein production by limiting PIE-1 mRNA transcript, which in turn would cause less translation of PIE-1. But no evidence exists for this pathway.

PAR-1 could be involved in PIE-1 source formation by organisation microtubules. One possibility would be that PIE-1 mRNA is local deposition and that the protein is made only in the posterior. This possibility can be excluded as no asymmetric mRNA could be detected in *in situ* hybridisation (Reese et al., 2000).

Local deposition of mRNA would involve directed transport e.g. along microfilaments as it has been described for *bicoid* (Cha et al., 2001) and *oskar* mRNA (Brendza et al., 2000) in the developing *Drosophila* oocyte. The contribution of microtubules to the formation of PIE-1 source can be also neglected. The PIE-1 posterior localisation was undisturbed in nocodazole treated embryos. Similar results have been described for PIE-1's cytoplasmic asymmetry in the two-cell stage (Reese et al., 2000), which indicates that PIE-1 source positioning is independent of PAR-1 microtubule regulation function.

All the reported functions do not explain how PAR-1 might regulate PIE-1 source formation. My results suggest that PIE-1 source is most likely formed by increase of local protein levels along the posterior cortex. Redistribution of existing protein is unlikely to be a dominant mechanism of posterior PIE-1 enrichment.

The constant increase of integrated PIE-1::GFP intensity however argues for a PIE-1 source formation mechanism that involves protein synthesis than stabilisation of present protein. In the *C. elegans* embryo, protein synthesis has not been observed in the one-cell embryo. The earliest detection of translation in the *C. elegans* embryo is POS-1 in the AB cell (Evans et al., 1994) but translation of PIE-1 was never specifically investigated.

The release of newly folded protein could be a possible mechanism for forming the PIE-1 source in absence of protein synthesis. The experiments I performed would not distinguish between protein synthesis and release of newly folded protein as the mechanism for PIE-1 source formation. Further experiments like the inhibition of protein synthesis in the one-cell embryo could provide further information about the nature of PIE-1 source formation.

The PIE-1 source formation does not occur during the whole cell division. There seems to be a time window during polarity establishment in which the PIE-1 source is made. This time seems to be sufficient to make a source that controls the asymmetry segregation of PIE-1.

3.2.3 PIE-granules contribution to source formation

In my results, PAR-1 depletion caused P granules and the PIE-1 source to disappear. In the literature, no depletion of a protein has been reported to cause the loss of all P granules. It might be that the settings I used for live-cell imaging were not sensitive enough to detect the small P granules, which would explain why I saw neither PIE granules nor MEX granules nor PGL-1 positive P granules. In a recent screen by Updike et al. (2009), PAR-1, PAR-2, as well as CDC-42 are reported to reduced levels of P granules, which are visualised by GFP::PGL-1. In my thesis, I could show that depletion of PAR-2 and CDC-42 still allowed the formation of the PIE-1 source. I detected a defect in PIE-1 source formation only after PAR-1 depletion. Thus, PIE-1 source formation seems to be independent of P granules.

3.3 Diffusion shapes the PIE-1 gradient

Is PIE-1 freely diffusing? An excellent method to answer this question is FCS. FCS data can be used to describe the mobility of proteins by giving information about the diffusion species, the diffusion coefficient and the type of motion (Bacia and Schwille, 2003).

The measured apparent diffusion coefficients of PIE-1 in wildtype and *mex-1(RNAi)* embryos were significantly smaller than the diffusion coefficient of free GFP in water (87 $\mu m^2/s$ (Pack et al., 2006): The fastest PIE-1::GFP molecule in wildtype embryos diffused approximately 10x slower and the fastest PIE-1::GFP molecule in *mex-1(RNAi)* embryos 6x slower than GFP in water. However, in a cell, where the viscosity of the cytoplasm slows the diffusion of the GFP molecule, cytosolic GFP diffusion is about 5x slower than GFP in water (Pack et al., 2006). Thus it appears that PIE-1-GFP can exist as a freely diffusing cytoplasmic species. The majority of correlation times about 70% however, implied that PIE-1 more often exists in a slow-moving form.

Table 2: Summary of diffusion coefficients D.

Particle	D [µm^2/sec]	Medium	Reference
GFP	87	water	(Pack et al., 2006)
GFP	23	cytoplasm HeLa cells	(Pack et al., 2006)
PIE-1::GFP fastest molecule	8	cytoplasm *C. elegans* embryo	
PIE-1::GFP mex-1(RNAi) fastest molecule	13	cytoplasm *C. elegans* embryo	

3.4 Degradation shapes the PIE-1 gradient

That degradation can shape a protein gradient is obvious but why is degradation so important? The Bicoid gradient is only present in the anterior of the developing *Drosphila* embryo, where it inhibits the transcription of genes that regulate the segment pattern of the embryo. In the posterior half of the embryo, transcription of these genes has to take place for the correct patterning of the embryo. The degradation of the morphogen, in this case Bicoid, restricts the spatial information to the part of the cell where it is needed. No mechanism has been identified that is involved in Bicoid degradation.

Is degradation of PIE-1 important for the PIE-1 gradient shape? In the 2-cell stage, a mechanism for clearance of mislocalised PIE-1 in AB cell has been suggested (DeRenzo et al., 2003). The interaction of PIE-1 with the *z*inc-*f*inger *i*nteracting protein (ZIF)-1 marks PIE-1 for degradation via the ubiquitin–proteasome pathway. Up to now, no role for protein degradation in establishing PIE-1 asymmetry in the one-cell embryo has been proposed.

My results indicate that there might be ZIF-1-dependent degradation involved in shaping the PIE-1 gradient. Without degradation, the PIE-1 gradient shape is more extended.

Is it local or global degradation? At this stage, I can only speculate about the mode of PIE-1 degradation. If global degradation is involved, additional PIE-1 protein stabilisation or constant production of PIE-1 has to occur to maintain the cytoplasmic levels of PIE-1. In the one-cell embryo, the production of PIE-1 seems to occur only in a short time window before NEBD. After this time, the cytoplasmic levels of PIE-1 remained constant, which makes it quite unlikely to have global degradation ocurring in the embryo.

What could loaclise PIE-1 degradation activity to the anterior? PAR-3 seems to be an ideal candidate. In some experiments, the depletion of PAR-3 led to a greater increase of total PIE-1 than in the control. In absence of PAR-3, the local degradation might not occur, which would result in the accumulation of cytoplasmic PIE-1. Additionally, the uniform distribution of PAR-3 along the cortex in cytochalsin D-treated embryos resulted in the localisation of PIE-1 source in the centre of the embryo. The lack of cytoplasmic PIE-1 along the cortex could not only be happening due to exclusion of the source from the cortex but also due to local degradation of PIE-1 along the cortex.

What would happen to PIE-1 when the PIE-1 gradient extends into the anterior? Mislocalised PIE-1 in the anterior might be degraded to ensure that PIE-1 only occupies the posterior cytoplasm. Evidence of such an effect can be observed in MEX-1 depleted embryos: PIE-1 diffusion is not slowed and enters the anterior half of the embryo. The cytoplasmic levels of PIE-1 in *mex-1(RNAi)* embryos are lower than controls, suggesting perhaps that PIE-1 is degraded. Increased degradation of the mislocalised anterior PIE-1 may be depleting the cytoplasmic pool of PIE-1. Ultimately, less PIE-1 would be segregated into P_1 cell, as observed in *mex-1(RNAi)* embryos.

An ideal experiment would be the inhibition of the ubiquitin–proteasome pathway by inhibitors and measurement the shape of the PIE-1 gradient. This way the contribution of degradation could be assessed.

3.5 PIE granule contribution to PIE-1 gradient formation

3.5.1 Formation of PIE granules

P granules have a multi protein composition. They can be visualised e.g. by PIE-1, MEX-1 or PGL-1 (Guedes and Priess, 1997; Kawasaki et al., 1998; Mello et al., 1996). In my results, the numbers of P granules detected by these proteins differ: the most P granules are detected by PGL-1. This suggests that either not all P granules contain PIE-1 and MEX-1 or that I could not detect all P granules with the imaging setting I used. P granules were detected when their intensity was about 10% above background level. PIE-1::GFP, for example, has a strong cytoplasmic signal. There might have been some PIE granules that I did not detect

due to the their low intensity. This problem seems rather minor for MEX-1, as P granules were readily visualised by GFP::MEX-1. The cytoplasmic MEX-1 signal was never as high as observed in PIE-1. In the one-cell embryo, not all P granules might contain PIE-1 or MEX-1, while the constitutive P granule component PGL-1 is always present (Kawasaki et al., 2004).

The formation of P granules themselves is thought to follow a hierarchical assembly: DEPS-1→ GLH-1→ PGL-1→ IFE-1 (Spike et al., 2008b). These proteins might interact with each other, with themselves, and with mRNAs, thus creating scaffold to which other proteins and mRNAs associate. These interactions have been described for proteins of the PGL family: Interactions between all three PGL proteins and IFE-1 have been reported *in vitro.* They associate with P granules independently (Kawasaki et al., 2004). There is no evidence for PIE-1 interacting with the any of P granules components but no extensive analysis has been done.

How does PIE-1 associate with P granules? The association of PIE-1 to P granules seemed to be controlled by MEX-1 and by cytoplasmic PIE-1 levels: In MEX-1 depleted embryos, PIE granules were detected when the cytoplasm reached 1.5-fold enrichment over the cytoplasm. This may represent a critical cytoplasmic PIE-1 concentration that allows PIE-1 to associate with P granules. Perhaps once PIE-1 is bound to P granules, it may be able to recruit more PIE-1 either directly by interacting with PIE-1 protein or by binding more mRNA via PIE-1's zinc-fingers. The absence of MEX-1 delays PIE-1 association with P granules but does not prevent it entirely.

MEX-1 may be needed for PIE granule formation if the cytoplasmic PIE-1 levels are lower than the critical concentration. Lowering the cytoplasmic PIE-1 concentration in the presence of MEX-1 [*pie-1(partial RNAi)*] allowed formation of PIE granules at a lower cytoplasmic concentration than without MEX-1.

How does MEX-1 facilitate PIE granule formation? P granules have been reported to behave like droplets, which fuse and drip (Brangwynne et al., 2009). How dynamic these processes are is unknown. My FCS data suggest that PIE-1 exists as two different fractions: fast- and slow-diffusing components. These components themselves are PIE-1 complexes of varying

sizes, perhaps P granule intermediates. The PIE-1 intermediates of the fast diffusing component would be rather small, e.g. PIE-1 interacting with only a few other proteins, which lowers the diffusion of this small PIE-1 intermediate. In contrast, PIE-1 intermediates of the slow-diffusing component could be PIE granules that underwent fusion. This big PIE-1 intermediate shows very slow diffusion.

These PIE-1 intermediates are dependent on MEX-1. Perhaps MEX-1 binds first to P granules and then starts recruiting PIE-1, either through protein–protein or protein–mRNA interactions.

Both mechanisms, MEX-1 facilitated binding and a critical concentration of PIE-1, appear to contribute to the formation of PIE granules. I propose the following hierarchy of P granule assembly in one-cell embryos: DEPS-1→ GLH-1→ PGL-1→ IFE-1→ MEX-1→ PIE-1. Several steps in this pathway, however, remain to be tested.

3.5.2 PIE granules and PIE-1 gradient formation

The association of PIE-1 to P granules seems to be important for the formation of a stable PIE-1 gradient. How do PIE granules stabilise the PIE-1 gradient? The diffusion of morphogens in tissues or in the syncyial *Drosophila* embryo is restricted in order to form a concentration gradient (Entchev et al., 2000). In a similar way, PIE-1 diffusion may need to be restricted in order to form the stable PIE-1 gradient. The association of PIE-1 to P granules may induce the necessary restricted diffusion in the one-cell embryo of *C. elegans*. I propose the following model of PIE-1 gradient formation: PIE-1 is produced at the source in the posterior of the embryo and freely moves away from the source. At the same time, PIE-1 protein starts aggregation and formation of higher complexes that fuse with other P granules and make up bigger PIE granules that then are visible above the cytoplasmic PIE-1 levels (Brangwynne et al., 2009). Since P granules only appear in the posterior half of the embryo and in proximity to the cortex, PIE-1 diffusion is restricted.

What happens if PIE-1's association with P granules is impaired? The aggregation of PIE-1 is reduced. Less PIE-1 is bound to P granules, which results in faster mobility of PIE-1. Consequently, an extended PIE-1 gradient forms.

But how can a stable PIE-1 gradient be formed in partial depletion of PIE-1, where fewer PIE granules form? The partial depletion of PIE-1 does not change PIE-1's ability to associate with P granules. The cytoplasmic level of PIE-1 is under the critical concentration for P granule association, which delays the appearance of PIE granules. I would assume that the PIE-1 aggregates are still formed. These PIE-1 intermediates are smaller than the detection limit but nevertheless present. Consequently, association into these PIE granule intermediates restricts PIE-1 mobility. Thus a stable PIE-1 gradient is formed.

3.6 Common mechanism for other germline fate determinants?

The cell fate determinant MEX-1 shows a similar segregation pattern to PIE-1 in the early *C. elegans* embryo (Mello et al., 1992). Additionally, MEX-1 forms a posterior concentration gradient with the source along the posterior cortex. Is there a common mechanism for the asymmetric segregation of germline cell fate determinants in *C. elegans* one-cell embryos? The formation of a MEX-1 concentration gradient at the posterior cortex and the association of MEX-1 with P granules are similar to the mechanism of PIE-1 segregation and would support the idea of a common mechanism. On the other hand, MEX-1 source formation seems to be independent of PAR-1 whereas PIE-1 source formation depends strictly on PAR-1. Furthermore, PGL-1 does not have a cytoplasmic component. These are evidences that not all germline fate determinants follow the same mechanism for asymmetric segregation as PIE-1. The formation of a concentration gradient might be a common tool for the segregation of molecules; however, the parameters for establishment of a gradient – source, diffusion rate, degradation and immobile faction – might vary.

4 Material and Methods

4.1 Cloning

4.1.1 Primers

Table 3: List of primers. The specific annealing temperature (T_{anneal}) is given for the primer pair. The primer pair with a geneservice (GS)-ID is a RNAi feeding construct from the Ahringer library accessed through http://www.geneservice.co.uk/products/tools/Celegans_Finder.jsp.

Name	Sequence	T_{anneal}	GS-ID
ama-1 FOR	GATAACTGGGAGACGTCGGTG		
ama-1 REV	ATCAATCGTCAGGAGGTTGG		
C44H4.4 FOR	ACACTTCACTCACCCTTGGC		X-6D24
C44H4.4 REV	TCAGCAATCTCATTTGCCAG		
cdc-42 FOR	GTTTGGCATTTTTCAGGGAA		
cdc-42 REV	ACGTGTGCGTGCACATTTAT		
ceh-37 FOR	CAACAAGTTTCAAATAGGCAAGG		X-6L05
ceh-37 REV	ATCTTCAACAAAAATCGAGGACA		
ima-2 FOR	GTGAGTGATGATGCGGTAAGC		
ima-2 REV	CTGGAAATGACTCGCTGACA		
ima-5 REV	AAGCATTTGCGCCTCGAATCTTCG	58	
imb-5 FOR	GGGACAGCGGAAGGATCAACT		
K07E3.1 FOR	GTCCACAACCATTGCATCTG		X-4K07
K07E3.1 REV	AAATCCATACGGCGAAAGTG		
L4440 seq	ACGACGTTGTAAAACGAC	44	
nmy-2 FOR	CTCAAATGGTGACAGTAAATTGGC	52	
nmy-2 REV	AACACGAGATCCAAATACTCC		
npp-9 FOR	TGCGAATCCTCTCGGCTCAATGATTCCTCC	52	
npp-9 REV	ATTTTGCCTCAGCGACAGCCTTCT		
pap-1 FOR	CCTCAATTTTCAGATCCCGA		V-7A16
pap-1 REV	ATGTTCCGCGAATTCAAGAC		
par-1 FOR	TAATACGACTCACTATAGTCCACATTCATG		
par-1 REV	AATTAACCCTCACCTAAAGGCACGTGATA		
par-2 FOR	GCCATTTTTCACGCAATTTT		
par-2 REV	GCATCAACGACGTTCAACAG		
pie-1 #3 FOR	CAAATGGCTGCACTCAACAACT	52	
pie-1 #3 REV	CTTATCCTTCGCCGAGCTATG		
pie-1 #5 FOR	TTTCAATGCGAATGCGACGGTT	52	
pie-1 #5 REV	CTGAGAGAAGAATCCATCGGGG		
pkc-3 FOR	GTGTTCCAAAGCTTCCCAATC		
pkc-3 REV	CATTTCCAACCACAATTCCC		
pqn-59 FOR	CGTCAATTCCTAACGGCGAT	52	
pqn-59 REV	TTCCAAGATTTCCACCATTGT		
ran-1 FOR	AGCTTGTCCTTGTCGGAGA		
ran-1 REV	TCTACCCAAGCCAGCACTTTGAATT		
rsr-2 FOR	GAGTACAACGGCGAAGATGAC	57	
rsr-2 REV	TGGCAGTGGATCTTCTCTCATTT		
sip-1 FOR	TGTCTTCTCTCTGCCCATAC	52	
sip-1 REV	TGCTGGATGGCTTCTGGGTGA		
smo-1 FOR	GCACTTCCGTGTAAAGTATGG	54	
smo-1 REV	GCAATTTGGCTTCCTCATCG		

Name	Sequence	T_{anneal}	GS-ID
spd-5 FOR	GTCGCAACCAGTTCTGAAT		
spd-5 REV	ATGGAGGCAAATTGTTGCTG		
syd-9 FOR	GAGCAGAACGAAGCAATAGC	57	
syd-9 REV	ACTACTTGCTGGAGTTGTTGG		
T7 promotor	GCGTAATACGACTCACTATA	44	
ttx-1 FOR	GCAACAACAGTAGCCGCCGC	63	
ttx-1 REV	GAACTCTGCTCTCGGGGAGTTG		
zen-4 FOR	GGAAAATGATGGACAAGCTACTG		IV-3I07
zen-4 REV	TCTTTGAATTCTGAACGAACCAT		
zif-1 FOR	CAAATTTTCAATTTTCCCATCAA		III-1K08
zif-1 REV	CAAAATCGCATTTAGAGCACAAT		
ubc-9 FOR	TTCGGCAGCATACTTCACAG		
ubc-9 REV	CAAAAATGTCGGGAATTGCT		

4.1.2 Reactions

blunt end digest	
10 µl	L4440 vector
2 µl	10x Tango buffer
2 µl	SmaI
	add water to 20 µl
2 hrs on 37°C	

The enzymes were removed the QIAGEN PCR purification kit following the protocol. The vector was eluted in 50 µl water.

t-tailing reaction	
50 µl	DNA
10 µl	10X PCR buffer
10 µl	25 mM $MgCl_2$
4 µl	100 mM dTTP
2 µl	Taq polymerase
	add water to 100 µl
2 hrs on 72°C	

The t-tailed vector cleaned with the QIAGEN PCR purification kit according to the manufacturer's protocol. The vector was stored for several months on -20°C.

PCR reaction	
0.1 µl	primer 1 (100 µM)
0.1 µl	primer 2 (100 µM)
1 µl	template DNA
2.5 µl	10X PCR buffer
1.5 µl	25 mM $MgCl_2$
0.25 µl	dNTP mix (10 mM)
0.5 µl	Taq polymerase
	add water to 25 µl

The template DNA was genomic DNA from N2 Bristol strain.

PCR Program		Temperature	Time [min:sec]
		95°C	2:00

	25x cycles	95°C T_{anneal} 72°C	0:45 0:45 1:00/kb target ($Time_{extensiton}$)
		72°C	2x $Time_{extension}$

The PCR product was purified with the QIAGEN PCR purification kit according to the manufacturer's protocol and eluted in 30 µl water. For the specific annealing temperatures of each primer pair see **Table 3**.

Ligation reaction	
1 µl	10X T4 ligation buffer
1 µl	t-tailed L4440 vector
8 µl	insert
16°C overnight	

Colony PCR reaction	
0.1 µl	primer 1 (100 µM)
0.1 µl	primer 2 (100 µM)
1 µl	template DNA
1 µl	DMSO
2.5 µl	10X PCR buffer
1.5 µl	25 mM MgCl2
0.25 µl	dNTP mix (10 mM)
0.5 µl	Taq polymerase
	add water to 25 µl

The template DNA was a bacterial colony picked and diluted in 5 µl water.

Colony PCR Program		Temperature	Time [min:sec]
		95°C	2:00
	25x cycles	95°C T_{anneal} 72°C	0:45 0:45 1:00/kb target ($Time_{extensiton}$)
		72°C	2x $Time_{extension}$

The PCR reaction was analysed by gel electrophoresis on a 1% agarose gel.

A pellitier thermocycler (Biorad, DNA Engine) was used for all PCR reactions.

4.1.3 Vectors

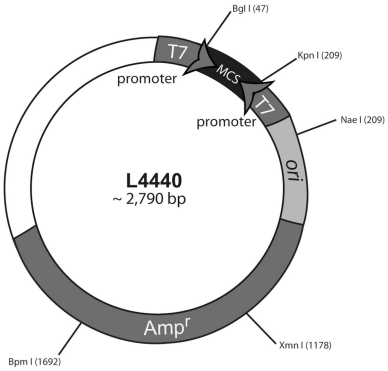

Figure 57: Vector map of L4440 expression vector. Adapted from Timmons and Fire (1998) and (2001).

4.2 Maintenance of worms

C. elegans is maintained on Nematode Growth Medium (NGM) agar plates and grown on a lawn of *E. coli* strain OP50 as a food source (Brenner, 1974). The worm stocks are kept on 16°C or 20°C (JH1327). Every other day, 3 to 5 adult hermaphrodites are transferred to a new feeding plate using a LEICA MZ125 stereomicroscscope equipped with Planapo objectives either 1.0x or 0.63x.

4.2.1 Freezing and recovery of *C. elegans* stocks

C. elegans can be frozen and stored a limited time at -80°C. Freshly starved young larvae (L1-L2 stage) survive freezing best. A plate of animals was washed off the plate with 0.1 M NaCl in a small volume and transferred to a freezing vial. The excess NaCl solutions was removed and glycerol 85% was added in equal volume. The vial was placed in a Styrofoam container on -80°C to allow a 1°C decrease in temperature per minute (Brenner, 1974).

For the recovery of frozen worms, 1/3 of the frozen worm stock was removed from the freezing vial and placed on a fresh feeding plate on room temperature. After 1 to 6 days, thawed worms could be recovered and transferred to a fresh feeding plate. The worms were used in experiments after one generation time.

4.2.2 Worm strains

The following worm strains were used in this study.

Table 4: Table of Worm strains:

Strain name	Genotyp
JA1559	mCH::β-tubulin
JH1327	PIE-1::GFP::rol-6 (axEx73)
JH1380	PAR-2::GFP
KK571	lon-1(e185) par-3(it71)/qC1 dpy-19(e1259) glp-1(q339)III
KK725	nop-1(it142)III
N2	Bristol strain
TH25	GFP::PAR-6
UE12	PIE-1::GFP::rol-6 (axEx73); nop-1(it142)
UE13	PIE-1::GFP::rol-6 (axEx73);par-3(e2074) lon-1(e185)
UE18	oaEX7[GFP::PGL-1];unc-119(ed3)
UE25	GFP::MEX-1(oaEX9); zif-1(gk117):unc-119(ed3)
UE27	GFP::MEX-1(oaEX9)
UE29	PIE-1::GFP::rol-6 (axEx73); zif-1(gk117):unc-119(ed3)
UE37	PIE-1::GFP::rol-6 (axEx73); mCH::β-tubulin

4.2.3 Crosses

4.2.3.1 UE13

The parental strains JH1327 and KK571 were crossed. The F1 progeny was allowed to self and the F2 progeny scored for rol-6 expression (worms were all rollers). Positive hermaphrodites were allowed to self and the F3 progeny was scored for homozygosity of the rol-6 and for dead embryos.

The strain was maintained heterozygous for par-3(e2074) lon-1(e185).

4.2.3.2 UE12

JH1327 and KK725 parental strains were used. F1 allowed to self, and the F2 generation scored for rol-6 mutation. Positive hermaphrodites were allowed to self, and the F3 progeny was scored for homozygosity of the rol-6 mutation and the no pseudocleavage (Nop) phenotype. In the next generation the homogozysity of the Nop phenotype was confirmed.

4.2.3.3 UE37

The parental strains JH1327 and JA1559 were crossed. The F1 progeny was allowed to self, and F2 was scored for rol-6 mutation. Positive hermaphrodites were allowed to self, and the

F3 generation was scored for homozygous rol-6 and mCherry expression of β-tubulin. The F4 progeny was scored for homozygous mCherry expression.

4.3 RNA-mediated interference (RNAi) by feeding

Feeding double stranded (ds)RNA expressing bacteria to *C. elegans* is a commonly used method to induce RNAi: A fragment corresponding to the gene of interest is inserted into the feeding vector (L4440) via TA cloning between two T7 promoters in inverted orientation. The vector is transformed into E. coli strain (HT115(DE3)), carrying IPTG-inducible expression of T7 polymerase (Kamath and Ahringer, 2003; Timmons and Fire, 1998).

4.3.1 Making the feeding bacteria

In brief, the linearised vector was t-tailed and the insert amplified from N2 genomic DNA was inserted into the modified L4440 vector and transformed into to *E. coli* HT115 bacteria. The bacteria were plated on LB + amp plates and positive colonies identified by colony PCR using the "T7 promotor" primer. The sequence of the insert was validated by sequencing using the L4440 seq primer. Transformed bacteria could be stored as a glycerol stock on -80°C.

4.3.2 Preparation of RNAi feeding plates

RNAi feeding bacteria were inoculated in an over night culture (LB + carb + tet) at 37°C on a shaker. Then 100 µl of the liquid culture were diluted in 5 ml LB + carb and incubated for 3 hours at 37°C on a shaker. Transcription of RNA was induced by adding 3 mM IPTG and additional incubation (30 min) on 37°C. The 250 µl bacterial solution was seeded onto NGM + carb + IPTG plates (4 cm). The plates were allowed to dry room temperature over night, shifted to 25°C for additional grows of the bacteria for 24 to 48 hrs and then stored at 4°C for a maximum of 4 weeks.

4.3.3 RNAi experiment set up

Worms were transferred to unseeded NGM plates for about 20 min to clean them of excess OP50 bacteria before placing them onto RNAi feeding plates. The stage of the used worms

depended on the incubation time on the RNAi plates (see **Table 5**). RNAi was induced on 25°C for the indicated times.

The RNAi efficiency was confirmed with a lethality test. In brief, 4 to 6 hermaphrodites were transferred to an OP50 plate at the beginning of each recording. After 4 hours, the adults were removed, and the eggs on the plate were counted. The plate was left on room temperature overnight. The non-hatched embryos were counted.

Table 5: RNAi incubation and developmental stages. * A consistent phenotype on 2 weeks old plates. In experiments with incubation time over 48 hrs, N2 males were added 6 hrs before the recording to avoid sterility of the hermaphrodites (labelled as 48+)

RNAi	Incubation Time [hrs]	Worm stage
ama-1	24	L4
cdc-42	48+	L3
ima-1	≥24	L4
imb-5	≥24	L4
mex-1	≥24	L4
nmy-2	≥24	L4
npp-9	≥24	L4
par-1	≥24	L4
par-2	48+	L3
par-3	20-24	L4
par-6	≥24*	L4
pie-1	18-20	L4
pie-1 partial	6	young adults
pkc-3	<20	young adults
ran-1	12	young adults
smo-1	≥24	L4
spd-5	20-24	L4
ubc-9	48+	L3
zen-4	≥24	L4

4.4 Western Blot

4.4.1 Preparation of worm lysate

20 adult hermaphrodites were washed with 0.1 M NaCl and centrifuged for 5 min at 3000 rpm. Afterwards, the supernatant was removed leaving about 10 µl of liquid in the reaction tube. The tube was transferred to liquid nitrogen for about 2 min, and an equal amount of 2x SDS-sample buffer was added. Twice, the lysate was heated up to 95°C and vortexed for 1 min. The lysate could be stored on -80°C.

4.4.2 SDS-Gel electrophoresis and wet-transfer

The lysate was centrifuged (max. speed, 5 min) and the supernatant was loaded on a NuPAGE® 4-12% Bis-Tris gradient gel (Invitrogen). The proteins were separated according to the manufactores protocol. 1x NuPAGE® MOPS buffer was used as the running buffer. The electrophoresis of the proteins was performed with 200 V constant for 50 minutes in the cold room.

The 20% methanol was freshly added to 1x transfer buffer (25 mM Tris, 190 mM Glycin, 0.02% SDS). For the wet blotting, the NuPAGE® XCellII™ Blot Module was used. According to the manufacture's protocol, the transfer was run on 30 Volts constant for 1 hour.

4.4.3 Detection

The membrane was incubated in blocking solution (5% milk in 0.1% Tween PBS) for 30 min at room temperature on shaker. The primary antibodies were diluted in blocking solution: mouse monoclonal anti-GFP (Santa Cruz, GFP (B-2), SC9990) 1:200 and mouse monoclonal anti-α tubulin (Sigma, T 6199) 1:3000. The membrane was incubated with the primary antibody over night at 4°C under constant moving. The excess antibody was washed off in 0.1% Tween/PBS for 15 min at room temperature on a shaker. The wash was repeated twice before the secondary antibody solution was added for 30 min at room temperature. The secondary antibody conjugated horseradish peroxidase goat anti-mouse IG (Biorad, 170-6516) was diluted in blocking solution 1:3000. Three washing steps removed the excess antibody. For the detection of the bound antibodies, enhanced chemiluminescence reagents were used (Amersham).

4.5 Microscopy

4.5.1 Preparation of worms

Worms were shifted to 25°C 18 to 48 hours before the recording to have full expression of the GFP. Worms were dissected in 2.5 µl dissection buffer (0.1 M NaCl, 4% sucrose) on a coverslip (18x18 mm) to release early embryos. Coverslips with embryos were inverted onto

an agarose pad (0.1 M NaCl, 4% sucrose, 2% agarose) on a standard microscope slide for microscopy.

Alternatively, hanging drop mounting was used, where coverslips were coated twice with poly-L-lysine: 20 µl of 0.01% poly-L-lysine solution were placed in the middle of the coverslip and allowed to dry at 50°C. Worms were dissected in 8 µl of dissecting buffer and embryos were pressed gently onto the sticky poly-L-lysine coat using an eyelash clued to a toothpick. On a glass slide, two strips of double-sided tape were fixed and then inverted onto the coverslip to create an imaging chamber.

4.5.2 Inhibitor treatment by soaking

About 10 gravid hermaphrodites were placed in 10 µl dissection buffer with inhibitor on a coverslip (18x18 mm). After cutting the tip of the worms' tails, the coverslip was transferred to a humid chamber for 20 min incubation at room temperature. Finally, the worms were dissected and the coverslip inverted onto an agarose pad on a microscope slide.

Table 6: List of inhibitors, their stock and final concentration as well as the storage information. All inhibitors were solubilised in DMSO except Sodium azide, which was solubilised in water.

Name	Stock concentration	Final concentration	Storage
Nocodazole	4 mg/ml	10 µg/ml	-20°C several months
Cytochalasin D	25 mg/ml	15 µg/ml	4°C, 3 years
Sodium azide	1 M	0.1 M	25°C, several months

4.5.3 Cytoplasmic displacement

About 5 gravid hermaphrodites were transferred into a 1.5 ml reaction tube containing 10 µl of dissection buffer and centrifuged for 3 min at 13000 rpm at room temperature. Afterwards the worms were transferred to a coverslip and process as described in 4.5.1.

4.5.4 Time-lapse recording

Images were taken on a LSM 510 Zeiss microscope using a Plan Apochromat 63x/1.40 Oil DIC M27 lens. LSM software AIM (version 4.2) was used for controlling the microscope and for acquisition of 12-bit images. Embryo recording was usually performed at 20°C to 25°C or as otherwise noted. GFP localisation dynamics were analysed by time-lapse

recordings at a single focal plane. Images were focused on the centre of the embryo and collected every 10 to 12 sec over an approximately 20 min period. At each time point, transmitted light images were collected. **Table 7** summarises the configurations of the microscopes.

Table 7: List of settings for the time-lapse recordings and the respective configurations.

	Parameters
Setting 1	pixel time: 6.4 µsec BP 500-550 488 laser pinhole: optical slice < 3.2 µm LSM 510
Setting 2	pixel time: 6.4 µsec BP 500-550 488 laser pinhole: optical slice < 3.2 µm LSM 510
Setting 4	pixel time: 6.4 µsec LP505 488 laser pinhole: optical slice < 3.2 µm LSM 510
Setting 5 Inhibitor Settings	pixel time: 12.8 µsec LP505 488 laser pinhole: optical slice < 3.2 µm LSM 510
Setting 7 MEX Settings	Argon/2 458/477/488/514 LP505 pixel time: 12.8 µsec pinhole: optical slice < 3.2 µm LSM 510 DUO
PGL Settings	Argon/2 458/477/488/514 LP505 pixel time: 12.8 µsec pinhole: optical slice < 1.5 µm LSM 510 DUO

4.5.5 Fluorescence Recovery after Photobleach (FRAP)

Embryos were prepared as described in 4.5.1. Images were acquired on a LSM 510 Duo (Zeiss) with a Plan Apochromat 63x/1.40 Oil DIC M27 lens. GFP fluorescence was excited by a 488 Argon laser and recorded with a bandpass filter 500–550 nm. 5 pre-bleach images were taken. The time of the bleach was optimised to give an approximate 50% drop of the

pre-bleach GFP intensity. The bleach was performed in a circular region with a diameter 30-pixels close to the posterior pole of the embryo (see **Figure 58**). The recovery of the GFP intensity was recorded in 0.5 sec time interval. The post-bleach time was chosen to allow complete recovery of the fluorescence intensity. One FRAP measurement per embryo was performed.

4.5.6 Fluorescence Correlation Spectroscopy (FCS)

Embryos were prepared using the hanging drop mounting (as described in 4.5.1) on a 170 μm thick coverglass (Menzel-Gläser 18x18 mm #1) FCS data were acquired with a Leica TCS SP2 AOBS FCS2 or with a Leica TCS SP5 AOBS SMD confocal laser scanning/FCS microscope. Green fluorescence was excited with the 488 nm line of an Argon laser and detected with a bandpass filter transmitting at 500–550 nm. For FCS and imaging an HCX Plan Apo 63x/1.2 NA CS water immersion objective lens was used that allows correcting for variations of the coverglass thickness. The pinhole diameter was set to match one Airy disk.
FCS data were acquired according to the following workflow: the focal plane of the microscope was placed at the equatorial plane of the embryo. Confocal images allowed to determine appropriate measurement positions as well as the time point when the nuclear envelope started to disassemble, at -2:00 relative to NEBD. Then FCS measurements were started for 8 x 15 sec. Images were acquired directly before and after the FCS measurement. Each embryo was observed until after cell division.

4.6 Data analyses

Data quantification was performed using MetaMorph (7.0r4) software. Data analyses were done in EXCEL, Graph Pad Prism 5 (version 5.0b) and GNU Octave (version 2.9.17; http://www.octave.org).
Average values are presented as mean ± standard error of the mean or whisker plot showing the minimum and maximum. The two-tailed Student's t-test assessed the significance of independent experiments. Values were considered significant at 95% confidence interval.

0:00 [min:sec] was assigned as nuclear envelope breakdown (NEBD): at this time, the nuclear envelope was completely disassembled, and the rotation of the spindle almost completed. If not otherwise state, the embryo length was standardised to 1 (anterior pole = 0).

4.6.1 Linescan measurements

The intensities along the anterior–posterior axis of the embryo were measured as average values of a 10-pixel wide line at indicated time points. The line was positioned so as to avoid contact with the centrosomes and nuclei, marked in **Figure 58**.

For smoothing of the data, a running average with a window size of the sample size (n) was used. The intensities were normalised to the average PIE-1 control for the appropriate acquisition setting (1 to 7) in a 25 pixels region around 0.25 EL at 0:00.

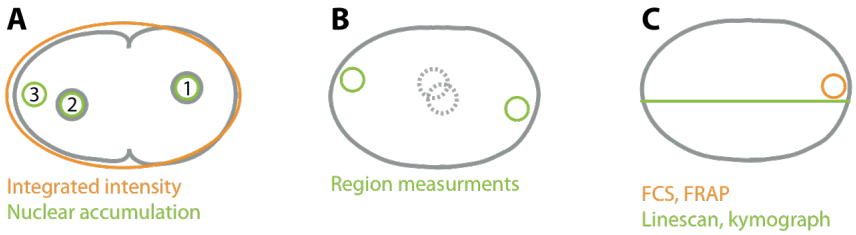

Figure 58: Positions for measurement in the embryo. A) The position of the ellipse to measure the integrated intensity of the entire embryo is drawn in orange. The positions of the three regions used to measure the nuclear accumulations are shown in green (1: male pronucleus, 2: female nucleus, 3: anterior cytoplasm). **B**) Positions of anterior and posterior circles to measure the posterior enrichement. **C**) Localisation of the bleach for FRAP and the FCS measurement is shown in orange. The line to get the intensity profiles and kymographs are shown. The dashed line indicates the postision of the disassembling nuclear envelope.

4.6.2 Region measurements and posterior enrichment

The cytoplasmic intensities at the posterior and anterior pole of embryos were measured as the average pixel intensity within circular regions (30-pixelss diameter). Pronuclei were not included, and the position was adjusted to avoid loss of signal due to embryo shortening around 0:00 (NEBD, see **Figure 58**). For analysis of mutant phenotypes, intensities were normalised to the average anterior intensity (0:00 to +0:40 relative to NEBD) of the respective wildtype control (setting 1 to 7).

The posterior–anterior ratio was determined from the average posterior and anterior region intensity measurements.

4.6.3 Integrated intensity

Embryos were mounted for microscopy with the hanging drop method. The integrated intensity GFP of the entire embryo was measured (**Figure 58**). The percent of increase was determined from -9:00 to -2:00 relative to NEBD.

4.6.4 PIE-1 levels

Embryos from JH1327 and UE37 strain were placed next to each other on poly-L-lysine coated coverslip and mounted for microscopy by hanging drop as described in 4.5.1. At time 0:00 (NEBD), the PIE-1::GFP integrated intensities were measured as described in 4.6.3. The ratio of the integrated PIE-1::GFP intensities of JH1327 over UE37 embryos was normalised to wildtype ratio.

4.6.5 Kymograph

A kymograph is an intensity measurement plotted against the time. PIE-1 intensities along the anterior–posterior axis of the embryo were measured as average values of a 10-pixels wide line from -8:00 to +4:00 relative to NEBD. The line was positioned so as to avoid contact with the centrosomes and nuclei. The image was displayed in pseudocolour.

4.6.6 Nuclear accumulation

The GFP intensities within the maternal and paternal pronuclei were determined as the average intensity of circular regions (30-pixels diameter, see **Figure 58**). The intensities were analysed every 30 sec from the first appearance of the pronuclei until 0:00. The intensities were normalised to the anterior cytoplasm (30-pixels diameter) at each time point.

4.6.7 P granule appearance

The time of P granule appearance was determined qualitatively. The earliest appearance of a P granule that could be followed in three consecutive frames was counted as the time of appearance. The cytoplasmic intensity in proximity of the granule was measured (circular

region 20-pixels diameter, see **Figure 58** for details), which were normalised to the anterior cytoplasm (circular region 20-pixels diameter).

4.6.8 Determination of P granule size and number

For detecting the size and number of P granules, an intensity threshold was used: The size was fixed to 0.5 and 5 µm for UE18 embryos and 0.7 and 5 µm for JH1327 and UE27 embryos and while the intensity was set to 10% above cytoplasmic intensity at EL 0.6.
The measurements were performed at 0:00 (NEBD).

4.6.9 Cortical and subcortical intensity measurements

The cortical and subcortical GFP intensities of PAR-2, PAR-6 and PIE-1 were measured as average values of a 10-pixel wide line at 0:00. The line was positioned on the plasma membrane and about 5 pixels away from the membrane for cortical and subcortical measurements, respectively (see **Figure 58** for details). The lateral cortex of half of an embryo was standardised to one, with 0 representing the anterior pole and 1 the posterior. Each intensity profile was standardised to its maximum value.

4.6.10 Single decay constant λ calculation (L.m)

The shape of an exponential gradient can be described with the decay constant λ (Robbins et al., 2001), which is defined as the position in the embryo at which the intensity was equal the maximum intensity divided by *e*. To calculate the decay constants for PIE-1 and MEX-1, the GFP intensities along the anterior–posterior axis of the embryo were determined from the average values of a 10-pixel wide line at 0:00. The line was perpendicular to the plasma membrane. For details see **Figure 58**.
We tried to avoid including P granules in the intensity measurements but nonetheless applied a filter to remove deviant intensity peaks from the data. Peak detection was performed by finding data points at positions x and x+4 that exhibited intensity differences exceeding 10% of the mean intensity value. These conditions were determined empirically using a set of representative PIE-1 and MEX-1 embryos with clearly visible P granule peaks. The background intensity was defined as the most frequent intensity bin after calculating the distribution histogram (ten bins) of all intensities. Intensity values were standardised to

background and background was subsequently subtracted. Embryo length was set to one (anterior pole = 0). Using intensity values from 0.33 to 0.90 EL, we then obtained the best-fit line (first order polynomial) of log(intensity) (x) and log(position) (y). The maximum intensity value from this range was divided by *e* to give the decay half-life, which was then used to solve the line equation at max/e to obtain the log(position) along the embryo axis. $e^{\log(\text{position})}$ produces the decay length of the gradient along the embryo axis. A correlation coefficient was calculated to evaluate the goodness of line fits; R^2 values ranged from 0.75 to 0.93 for the data included in the analysis.

4.6.11 Time-lapse decay constant λ calculations (Ltime.m)

Best-fit polynomials were determined every 30 sec over a period of 15 min starting with polarity establishment, according to the method described in 4.6.10 but including linear (first order), exponential (double-log first order), or complex (double-log second order) equations. Correlation coefficients were calculated to evaluate the goodness of fits. Higher order polynomials did not describe the data with greater accuracy than first order equations throughout the time series, and thus we did not consider complex distribution patterns. Based on R^2 values, intensity profiles were assigned as either exponential ($R^2 \geq 0.75$) or linear (exponential $R^2 < 0.75$) decays.

4.6.12 FRAP

For the determination of the half-time recovery, only the post-bleach recovery intensities were used. The average intensity in a circular region of 20-pixel diameter within the bleached region was used for calculating the half-time recovery. A region (20-pixel diameter) outside the embryo was used for background correction. The recovery curve was fit with a single exponential association equation using the build in function “bottom to span” in Graphpad Prism. The FRAP half-time $t(1/2) = \ln(2)/k$ was calculated. Only fits with a R^2 value >0.95 were used.

4.6.13 FCS

The autocorrelation functions of FCS raw data were computed using the Fluctuation Analyser software (version 2.0) written by Malte Wachsmuth, EMBL Heidelberg, that

allows to remove slow fluctuations due to cellular movements or photobleaching. The correlated curves were fitted individually with a two-component three-dimensional anomalous diffusion model (Wachsmuth & Weisshart 2007) using Origin (OriginLab, Northampton/MA, USA):

$$G(\tau) = \frac{1}{N}\left[1 - \Theta + \Theta \exp\left(-\frac{\tau}{\tau_{\text{blink}}}\right)\right] \sum_{i=1}^{2} f_i \left[1 + \left(\frac{\tau}{\tau_{\text{diff},i}}\right)^{\alpha_i}\right]^{-1} \left[1 + \frac{1}{\kappa^2}\left(\frac{\tau}{\tau_{\text{diff},i}}\right)^{\alpha_i}\right]^{-1/2},$$

where N is the average number of molecules inside the focal volume, θ the average number of molecules in a non-fluorescent state, τ_{blink} the lifetime of that state, $\tau_{\text{diff},i}$ the diffusional dwell time of the molecules of component i in the focal volume, α_i the corresponding anomaly parameter (with $0 \le \alpha_i \le 2$) and f_i the fraction of the molecules belonging to component i. The ellipticity of the focal volume is accounted for with the structure parameter κ that describes the ratio of axial to lateral focal radius. The diffusional dwell time or diffusion correlation time is related to the lateral focal radius w_0 and the diffusion coefficient D_i according to $\tau_{\text{diff},i} = w_0^2 / 4D_i$. Using the fluorophore Alexa488 in aqueous solution, the focal volume could be characterized with $w_0 = 160 \pm 16$ nm, $\kappa = 6 \pm 1$, allowing determining apparent diffusion coefficients.

4.7 Material

4.7.1 Plates

NGM plates	
3 g	NaCl
17 g	agar
2.5 g	peptone
	add to 1 litre with water autoclave for 50 min cool flask in 55°C water bath for 15 min
1 ml	1 M $CaCl_2$
1 ml	5 mg/ml cholesterol in ethanol
25 ml	1 M KPO_4
	Swirl to mix well fill NGM solution petri plates 2/3 full of agar let plates cool down before storing them 4°C in a air-tight contrainer for several weeks

4.7.2 Reagents

All reagents were purchased from Sigma Aldrich or otherwise indicated.

5 References

WormAtlas, Altun, Z.F., Herndon, L.A., Crocker, C., Lints, R. and Hall, D.H. (ed.s) 2002-2010. http://www.wormatlas.org

http://nobelprize.org/

Wachsmuth M, and Weisshart K (2007). Fluorescence photobleaching and fluorescence correlation spectroscopy: two complementary technologies to study molecular dynamics in living cells. In Imaging Cellular and Molecular Biological Functions (eds. Shorte S, and Frischknecht F), Springer Verlag, Heidelberg.

Afshar, K., Werner, M.E., Tse, Y.C., Glotzer, M., and Gönczy, P. (2010). Regulation of cortical contractility and spindle positioning by the protein phosphatase 6 PPH-6 in one-cell stage C. elegans embryos. Development *137*, 237-247.

Afshar, K., Willard, F.S., Colombo, K., Johnston, C.A., McCudden, C.R., Siderovski, D.P., and Gönczy, P. (2004). RIC-8 is required for GPR-1/2-dependent Galpha function during asymmetric division of C. elegans embryos. Cell *119*, 219-230.

Albertson, D.G. (1984). Formation of the first cleavage spindle in nematode embryos. Dev Biol *101*, 61-72.

Amiri, A., Keiper, B.D., Kawasaki, I., Fan, Y., Kohara, Y., Rhoads, R.E., and Strome, S. (2001). An isoform of eIF4E is a component of germ granules and is required for spermatogenesis in C. elegans. Development *128*, 3899-3912.

Ariz, M., Mainpal, R., and Subramaniam, K. (2009). C. elegans RNA-binding proteins PUF-8 and MEX-3 function redundantly to promote germline stem cell mitosis. Dev Biol *326*, 295-304.

Askjaer, P., Galy, V., Hannak, E., and Mattaj, I.W. (2002). Ran GTPase cycle and importins alpha and beta are essential for spindle formation and nuclear envelope assembly in living Caenorhabditis elegans embryos. Mol Biol Cell *13*, 4355-4370.

Bacia, K., and Schwille, P. (2003). A dynamic view of cellular processes by in vivo fluorescence auto- and cross-correlation spectroscopy. Methods *29*, 74-85.

Barbee, S.A., Lublin, A.L., and Evans, T.C. (2002). A novel function for the Sm proteins in germ granule localization during C. elegans embryogenesis. Curr Biol *12*, 1502-1506.

Batchelder, C., Dunn, M.A., Choy, B., Suh, Y., Cassie, C., Shim, E.Y., Shin, T.H., Mello, C., Seydoux, G., and Blackwell, T.K. (1999). Transcriptional repression by the Caenorhabditis elegans germ-line protein PIE-1. Genes Dev *13*, 202-212.

Betschinger, J., and Knoblich, J.A. (2004). Dare to be different: asymmetric cell division in Drosophila, C. elegans and vertebrates. Curr Biol *14*, R674-685.

Blackshear, P.J. (2002). Tristetraprolin and other CCCH tandem zinc-finger proteins in the regulation of mRNA turnover. Biochem Soc Trans *30*, 945-952.

Bowerman, B., Draper, B.W., Mello, C.C., and Priess, J.R. (1993). The maternal gene skn-1 encodes a protein that is distributed unequally in early C. elegans embryos. Cell *74*, 443-452.

Boyd, L., Guo, S., Levitan, D., Stinchcomb, D.T., and Kemphues, K.J. (1996). PAR-2 is asymmetrically distributed and promotes association of P granules and PAR-1 with the cortex in C. elegans embryos. Development *122*, 3075-3084.

Brangwynne, C.P., Eckmann, C.R., Courson, D.S., Rybarska, A., Hoege, C., Gharakhani, J., Jülicher, F., and Hyman, A.A. (2009). Germline P granules are liquid droplets that localize by controlled dissolution/condensation. Science *324*, 1729-1732.

Brendza, R.P., Serbus, L.R., Duffy, J.B., and Saxton, W.M. (2000). A function for kinesin I in the posterior transport of oskar mRNA and Staufen protein. Science *289*, 2120-2122.

Brenner, S. (1974). The genetics of Caenorhabditis elegans. Genetics *77*, 71-94.

Bringmann, H., and Hyman, A.A. (2005). A cytokinesis furrow is positioned by two consecutive signals. Nature *436*, 731-734.

Cha, B.J., Koppetsch, B.S., and Theurkauf, W.E. (2001). In vivo analysis of Drosophila bicoid mRNA localization reveals a novel microtubule-dependent axis specification pathway. Cell *106*, 35-46.

Checchi, P.M., and Kelly, W.G. (2006). emb-4 is a conserved gene required for efficient germline-specific chromatin remodeling during Caenorhabditis elegans embryogenesis. Genetics *174*, 1895-1906.

Cheeks, R.J., Canman, J.C., Gabriel, W.N., Meyer, N., Strome, S., and Goldstein, B. (2004). C. elegans PAR proteins function by mobilizing and stabilizing asymmetrically localized protein complexes. Curr Biol *14*, 851-862.

Colombo, K., Grill, S.W., Kimple, R.J., Willard, F.S., Siderovski, D.P., and Gönczy, P. (2003). Translation of polarity cues into asymmetric spindle positioning in Caenorhabditis elegans embryos. Science *300*, 1957-1961.

Coppey, M., Berezhkovskii, A.M., Kim, Y., Boettiger, A.N., and Shvartsman, S.Y. (2007). Modeling the bicoid gradient: diffusion and reversible nuclear trapping of a stable protein. Dev Biol *312*, 623-630.

Couwenbergs, C., Labbé, J.-C., Goulding, M., Marty, T., Bowerman, B., and Gotta, M. (2007). Heterotrimeric G protein signaling functions with dynein to promote spindle positioning in C. elegans. The Journal of Cell Biology *179*, 15-22.

Cowan, C.R., and Hyman, A.A. (2004a). Asymmetric cell division in C. elegans: cortical polarity and spindle positioning. Annu Rev Cell Dev Biol *20*, 427-453.

Cowan, C.R., and Hyman, A.A. (2004b). Centrosomes direct cell polarity independently of microtubule assembly in C. elegans embryos. Nature *431*, 92-96.

Cowan, C.R., and Hyman, A.A. (2006). Cyclin E-Cdk2 temporally regulates centrosome assembly and establishment of polarity in Caenorhabditis elegans embryos. Nat Cell Biol *8*, 1441-1447.

Cowan, C.R., and Hyman, A.A. (2007). Acto-myosin reorganization and PAR polarity in C. elegans. Development *134*, 1035-1043.

Cuenca, A.A., Schetter, A., Aceto, D., Kemphues, K., and Seydoux, G. (2003). Polarization of the C. elegans zygote proceeds via distinct establishment and maintenance phases. Development *130*, 1255-1265.

Daniels, B.R., Perkins, E.M., Dobrowsky, T.M., Sun, S.X., and Wirtz, D. (2009). Asymmetric enrichment of PIE-1 in the Caenorhabditis elegans zygote mediated by binary counterdiffusion. The Journal of Cell Biology *184*, 473-479.

Dechant, R., and Glotzer, M. (2003). Centrosome separation and central spindle assembly act in redundant pathways that regulate microtubule density and trigger cleavage furrow formation. Dev Cell *4*, 333-344.

DeRenzo, C., Reese, K.J., and Seydoux, G. (2003). Exclusion of germ plasm proteins from somatic lineages by cullin-dependent degradation. Nature *424*, 685-689.

Diaz-Benjumea, F.J., and Cohen, S.M. (1994). wingless acts through the shaggy/zeste-white 3 kinase to direct dorsal-ventral axis formation in the Drosophila leg. Development *120*, 1661-1670.

Draper, B.W., Mello, C.C., Bowerman, B., Hardin, J., and Priess, J.R. (1996). MEX-3 is a KH domain protein that regulates blastomere identity in early C. elegans embryos. Cell *87*, 205-216.

Drewes, G., Ebneth, A., Preuss, U., Mandelkow, E.M., and Mandelkow, E. (1997). MARK, a novel family of protein kinases that phosphorylate microtubule-associated proteins and trigger microtubule disruption. Cell *89*, 297-308.

Driever, W., and Nüsslein-Volhard, C. (1988a). A gradient of bicoid protein in Drosophila embryos. Cell *54*, 83-93.

Driever, W., and Nüsslein-Volhard, C. (1988b). The bicoid protein determines position in the Drosophila embryo in a concentration-dependent manner. Cell *54*, 95-104.

Driever, W., and Nüsslein-Volhard, C. (1989). The bicoid protein is a positive regulator of hunchback transcription in the early Drosophila embryo. Nature *337*, 138-143.

Eddy, E.M. (1975). Germ plasm and the differentiation of the germ cell line. Int Rev Cytol *43*, 229-280.

Edgar, L.G., Carr, S., Wang, H., and Wood, W.B. (2001). Zygotic expression of the caudal homolog pal-1 is required for posterior patterning in Caenorhabditis elegans embryogenesis. Dev Biol *229*, 71-88.

Entchev, E.V., Schwabedissen, A., and González-Gaitán, M. (2000). Gradient formation of the TGF-beta homolog Dpp. Cell *103*, 981-991.

Etemad-Moghadam, B., Guo, S., and Kemphues, K.J. (1995). Asymmetrically distributed PAR-3 protein contributes to cell polarity and spindle alignment in early C. elegans embryos. Cell *83*, 743-752.

Evans, T.C., Crittenden, S.L., Kodoyianni, V., and Kimble, J. (1994). Translational control of maternal glp-1 mRNA establishes an asymmetry in the C. elegans embryo. Cell *77*, 183-194.

Ghosh, D., and Seydoux, G. (2008). Inhibition of transcription by the Caenorhabditis elegans germline protein PIE-1: genetic evidence for distinct mechanisms targeting initiation and elongation. Genetics *178*, 235-243.

Glotzer, M. (2009). The 3Ms of central spindle assembly: microtubules, motors and MAPs. Nat Rev Mol Cell Biol *10*, 9-20.

Goldstein, B., and Hird, S.N. (1996). Specification of the anteroposterior axis in Caenorhabditis elegans. Development *122*, 1467-1474.

Goldstein, B., and Macara, I.G. (2007). The PAR proteins: fundamental players in animal cell polarization. Dev Cell *13*, 609-622.

Gomes, J.E., Encalada, S.E., Swan, K.A., Shelton, C.A., Carter, J.C., and Bowerman, B. (2001). The maternal gene spn-4 encodes a predicted RRM protein required for mitotic spindle orientation and cell fate patterning in early C. elegans embryos. Development *128*, 4301-4314.

Gönczy, P. (2008). Mechanisms of asymmetric cell division: flies and worms pave the way. Nat Rev Mol Cell Biol *9*, 355-366.

Gönczy, P., Pichler, S., Kirkham, M., and Hyman, A.A. (1999a). Cytoplasmic dynein is required for distinct aspects of MTOC positioning, including centrosome separation, in the one cell stage Caenorhabditis elegans embryo. The Journal of Cell Biology *147*, 135-150.

Gönczy, P., and Rose, L.S. (2005). Asymmetric cell division and axis formation in the embryo. WormBook : the online review of C elegans biology, 1-20.

Gönczy, P., Schnabel, H., Kaletta, T., Amores, A.D., Hyman, T., and Schnabel, R. (1999b). Dissection of cell division processes in the one cell stage Caenorhabditis elegans embryo by mutational analysis. The Journal of Cell Biology *144*, 927-946.

Gotta, M., and Ahringer, J. (2001a). Axis determination in C. elegans: initiating and transducing polarity. Curr Opin Genet Dev *11*, 367-373.

Gotta, M., and Ahringer, J. (2001b). Distinct roles for Galpha and Gbetagamma in regulating spindle position and orientation in Caenorhabditis elegans embryos. Nat Cell Biol *3*, 297-300.

Gotta, M., Dong, Y., Peterson, Y.K., Lanier, S.M., and Ahringer, J. (2003). Asymmetrically distributed C. elegans homologs of AGS3/PINS control spindle position in the early embryo. Curr Biol *13*, 1029-1037.

Greco, V., Hannus, M., and Eaton, S. (2001). Argosomes: a potential vehicle for the spread of morphogens through epithelia. Cell *106*, 633-645.

Greenstein, D. (2005). Control of oocyte meiotic maturation and fertilization. WormBook : the online review of C elegans biology, 1-12.

Gregor, T., Wieschaus, E.F., McGregor, A.P., Bialek, W., and Tank, D.W. (2007). Stability and nuclear dynamics of the bicoid morphogen gradient. Cell *130*, 141-152.

Grill, S.W., Gönczy, P., Stelzer, E.H., and Hyman, A.A. (2001). Polarity controls forces governing asymmetric spindle positioning in the Caenorhabditis elegans embryo. Nature *409*, 630-633.

Grill, S.W., Howard, J., Schäffer, E., Stelzer, E.H.K., and Hyman, A.A. (2003). The distribution of active force generators controls mitotic spindle position. Science *301*, 518-521.

Guedes, S., and Priess, J.R. (1997). The C. elegans MEX-1 protein is present in germline blastomeres and is a P granule component. Development *124*, 731-739.

Guo, S., and Kemphues, K.J. (1995). par-1, a gene required for establishing polarity in C. elegans embryos, encodes a putative Ser/Thr kinase that is asymmetrically distributed. Cell *81*, 611-620.

Guo, S., and Kemphues, K.J. (1996). A non-muscle myosin required for embryonic polarity in Caenorhabditis elegans. Nature *382*, 455-458.

Hamill, D.R., Severson, A.F., Carter, J.C., and Bowerman, B. (2002). Centrosome maturation and mitotic spindle assembly in C. elegans require SPD-5, a protein with multiple coiled-coil domains. Dev Cell *3*, 673-684.

Hao, Y., Boyd, L., and Seydoux, G. (2006). Stabilization of cell polarity by the C. elegans RING protein PAR-2. Dev Cell *10*, 199-208.

Hill, D.P., and Strome, S. (1988). An analysis of the role of microfilaments in the establishment and maintenance of asymmetry in Caenorhabditis elegans zygotes. Dev Biol *125*, 75-84.

Hill, D.P., and Strome, S. (1990). Brief cytochalasin-induced disruption of microfilaments during a critical interval in 1-cell C. elegans embryos alters the partitioning of developmental instructions to the 2-cell embryo. Development *108*, 159-172.

Hird, S.N., Paulsen, J.E., and Strome, S. (1996). Segregation of germ granules in living Caenorhabditis elegans embryos: cell-type-specific mechanisms for cytoplasmic localisation. Development *122*, 1303-1312.

Hung, T.J., and Kemphues, K.J. (1999). PAR-6 is a conserved PDZ domain-containing protein that colocalizes with PAR-3 in Caenorhabditis elegans embryos. Development *126*, 127-135.

Hunter, C.P., and Kenyon, C. (1996). Spatial and temporal controls target pal-1 blastomere-specification activity to a single blastomere lineage in C. elegans embryos. Cell *87*, 217-226.

Jenkins, N., Saam, J.R., and Mango, S.E. (2006). CYK-4/GAP provides a localized cue to initiate anteroposterior polarity upon fertilization. Science *313*, 1298-1301.

Jones, A.R., Francis, R., and Schedl, T. (1996). GLD-1, a cytoplasmic protein essential for oocyte differentiation, shows stage- and sex-specific expression during Caenorhabditis elegans germline development. Dev Biol *180*, 165-183.

Jones, D., Crowe, E., Stevens, T.A., and Candido, E.P.M. (2002). Functional and phylogenetic analysis of the ubiquitylation system in Caenorhabditis elegans: ubiquitin-conjugating enzymes, ubiquitin-activating enzymes, and ubiquitin-like proteins. Genome Biol *3*, RESEARCH0002.

Kamath, R.S., and Ahringer, J. (2003). Genome-wide RNAi screening in Caenorhabditis elegans. Methods *30*, 313-321.

Kawasaki, I., Amiri, A., Fan, Y., Meyer, N., Dunkelbarger, S., Motohashi, T., Karashima, T., Bossinger, O., and Strome, S. (2004). The PGL family proteins associate with germ granules and function redundantly in Caenorhabditis elegans germline development. Genetics *167*, 645-661.

Kawasaki, I., Shim, Y.H., Kirchner, J., Kaminker, J., Wood, W.B., and Strome, S. (1998). PGL-1, a predicted RNA-binding component of germ granules, is essential for fertility in C. elegans. Cell *94*, 635-645.

Kemphues, K.J., Priess, J.R., Morton, D.G., and Cheng, N.S. (1988). Identification of genes required for cytoplasmic localization in early C. elegans embryos. Cell *52*, 311-320.

Kicheva, A., Pantazis, P., Bollenbach, T., Kalaidzidis, Y., Bittig, T., Jülicher, F., and González-Gaitán, M. (2007). Kinetics of morphogen gradient formation. Science *315*, 521-525.

Kimura, A., and Onami, S. (2005). Computer simulations and image processing reveal length-dependent pulling force as the primary mechanism for C. elegans male pronuclear migration. Dev Cell *8*, 765-775.

Kirby, C., Kusch, M., and Kemphues, K. (1990). Mutations in the par genes of Caenorhabditis elegans affect cytoplasmic reorganization during the first cell cycle. Dev Biol *142*, 203-215.

Kuznicki, K.A., Smith, P.A., Leung-Chiu, W.M., Estevez, A.O., Scott, H.C., and Bennett, K.L. (2000). Combinatorial RNA interference indicates GLH-4 can compensate for GLH-1; these two P granule components are critical for fertility in C. elegans. Development *127*, 2907-2916.

Labbé, J.-C., McCarthy, E.K., and Goldstein, B. (2004). The forces that position a mitotic spindle asymmetrically are tethered until after the time of spindle assembly. The Journal of Cell Biology *167*, 245-256.

Levitan, D.J., Boyd, L., Mello, C.C., Kemphues, K.J., and Stinchcomb, D.T. (1994). par-2, a gene required for blastomere asymmetry in Caenorhabditis elegans, encodes zinc-finger and ATP-binding motifs. Proc Natl Acad Sci USA *91*, 6108-6112.

Lewis, J. (2008). From signals to patterns: space, time, and mathematics in developmental biology. Science *322*, 399-403.

Li, J., Kim, H., Aceto, D.G., Hung, J., Aono, S., and Kemphues, K.J. (2010). Binding to PKC-3, but not to par-3 or to a conventional PDZ domain ligand, is required for PAR-6 function in C. elegans. Dev Biol.

Li, W., DeBella, L.R., Guven-Ozkan, T., Lin, R., and Rose, L.S. (2009). An eIF4E-binding protein regulates katanin protein levels in C. elegans embryos. The Journal of Cell Biology *187*, 33-42.

Lipshitz, H.D. (2009). Follow the mRNA: a new model for Bicoid gradient formation. Nat Rev Mol Cell Biol *10*, 509-512.

Matenia, D., and Mandelkow, E.-M. (2009). The tau of MARK: a polarized view of the cytoskeleton. Trends Biochem Sci *34*, 332-342.

Mello, C.C., Draper, B.W., Krause, M., Weintraub, H., and Priess, J.R. (1992). The pie-1 and mex-1 genes and maternal control of blastomere identity in early C. elegans embryos. Cell *70*, 163-176.

Mello, C.C., Schubert, C., Draper, B., Zhang, W., Lobel, R., and Priess, J.R. (1996). The PIE-1 protein and germline specification in C. elegans embryos. Nature *382*, 710-712.

Morton, D.G., Shakes, D.C., Nugent, S., Dichoso, D., Wang, W., Golden, A., and Kemphues, K.J. (2002). The Caenorhabditis elegans par-5 gene encodes a 14-3-3 protein required for cellular asymmetry in the early embryo. Dev Biol *241*, 47-58.

Motegi, F., and Sugimoto, A. (2006). Sequential functioning of the ECT-2 RhoGEF, RHO-1 and CDC-42 establishes cell polarity in Caenorhabditis elegans embryos. Nat Cell Biol *8*, 978-985.

Munro, E., Nance, J., and Priess, J.R. (2004). Cortical flows powered by asymmetrical contraction transport PAR proteins to establish and maintain anterior-posterior polarity in the early C. elegans embryo. Dev Cell *7*, 413-424.

Nguyen-Ngoc, T., Afshar, K., and Gönczy, P. (2007). Coupling of cortical dynein and G alpha proteins mediates spindle positioning in Caenorhabditis elegans. Nat Cell Biol *9*, 1294-1302.

O'Connell, K.F. (2000). The centrosome of the early C. elegans embryo: inheritance, assembly, replication, and developmental roles. Curr Top Dev Biol *49*, 365-384.

O'Connell, K.F., Maxwell, K.N., and White, J.G. (2000). The spd-2 gene is required for polarization of the anteroposterior axis and formation of the sperm asters in the Caenorhabditis elegans zygote. Dev Biol *222*, 55-70.

O'Connor, M.B., Umulis, D., Othmer, H.G., and Blair, S.S. (2006). Shaping BMP morphogen gradients in the Drosophila embryo and pupal wing. Development *133*, 183-193.

Oegema, K., and Hyman, A.A. (2006). Cell division. WormBook : the online review of C elegans biology, 1-40.

Ogura, K.-I., Kishimoto, N., Mitani, S., Gengyo-Ando, K., and Kohara, Y. (2003). Translational control of maternal glp-1 mRNA by POS-1 and its interacting protein SPN-4 in Caenorhabditis elegans. Development *130*, 2495-2503.

Pack, C., Saito, K., Tamura, M., and Kinjo, M. (2006). Microenvironment and effect of energy depletion in the nucleus analyzed by mobility of multiple oligomeric EGFPs. Biophys J *91*, 3921-3936.

Pelletier, L., Ozlü, N., Hannak, E., Cowan, C., Habermann, B., Ruer, M., Müller-Reichert, T., and Hyman, A.A. (2004). The Caenorhabditis elegans centrosomal protein SPD-2 is required for both pericentriolar material recruitment and centriole duplication. Curr Biol *14*, 863-873.

Powell-Coffman, J.A., Knight, J., and Wood, W.B. (1996). Onset of C. elegans gastrulation is blocked by inhibition of embryonic transcription with an RNA polymerase antisense RNA. Dev Biol *178*, 472-483.

Ramírez-Weber, F.A., and Kornberg, T.B. (1999). Cytonemes: cellular processes that project to the principal signaling center in Drosophila imaginal discs. Cell *97*, 599-607.

Reese, K.J., Dunn, M.A., Waddle, J.A., and Seydoux, G. (2000). Asymmetric segregation of PIE-1 in C. elegans is mediated by two complementary mechanisms that act through separate PIE-1 protein domains. Mol Cell *6*, 445-455.

Riechmann, V., and Ephrussi, A. (2001). Axis formation during Drosophila oogenesis. Curr Opin Genet Dev *11*, 374-383.

Riechmann, V., and Ephrussi, A. (2004). Par-1 regulates bicoid mRNA localisation by phosphorylating Exuperantia. Development *131*, 5897-5907.

Robbins, J.R., Monack, D., McCallum, S.J., Vegas, A., Pham, E., Goldberg, M.B., and Theriot, J.A. (2001). The making of a gradient: IcsA (VirG) polarity in Shigella flexneri. Mol Microbiol *41*, 861-872.

Rose, L.S., Lamb, M.L., Hird, S.N., and Kemphues, K.J. (1995). Pseudocleavage is dispensable for polarity and development in C. elegans embryos. Dev Biol *168*, 479-489.

Sadler, P.L., and Shakes, D.C. (2000). Anucleate Caenorhabditis elegans sperm can crawl, fertilize oocytes and direct anterior-posterior polarization of the 1-cell embryo. Development *127*, 355-366.

Schaner, C.E., Deshpande, G., Schedl, P.D., and Kelly, W.G. (2003). A conserved chromatin architecture marks and maintains the restricted germ cell lineage in worms and flies. Dev Cell *5*, 747-757.

Schisa, J.A., Pitt, J.N., and Priess, J.R. (2001). Analysis of RNA associated with P granules in germ cells of C. elegans adults. Development *128*, 1287-1298.

Schmidt, D.J., Rose, D.J., Saxton, W.M., and Strome, S. (2005). Functional analysis of cytoplasmic dynein heavy chain in Caenorhabditis elegans with fast-acting temperature-sensitive mutations. Mol Biol Cell *16*, 1200-1212.

Schonegg, S., and Hyman, A.A. (2006). CDC-42 and RHO-1 coordinate acto-myosin contractility and PAR protein localization during polarity establishment in C. elegans embryos. Development *133*, 3507-3516.

Schroeder, T.E. (1973). Actin in dividing cells: contractile ring filaments bind heavy meromyosin. Proc Natl Acad Sci USA *70*, 1688-1692.

Severson, A.F., Baillie, D.L., and Bowerman, B. (2002). A Formin Homology protein and a profilin are required for cytokinesis and Arp2/3-independent assembly of cortical microfilaments in C. elegans. Curr Biol *12*, 2066-2075.

Seydoux, G., Mello, C.C., Pettitt, J., Wood, W.B., Priess, J.R., and Fire, A. (1996). Repression of gene expression in the embryonic germ lineage of C. elegans. Nature *382*, 713-716.

Shakes, D.C., Sadler, P.L., Schumacher, J.M., Abdolrasulnia, M., and Golden, A. (2003). Developmental defects observed in hypomorphic anaphase-promoting complex mutants are linked to cell cycle abnormalities. Development *130*, 1605-1620.

Shelton, C.A., Carter, J.C., Ellis, G.C., and Bowerman, B. (1999). The nonmuscle myosin regulatory light chain gene mlc-4 is required for cytokinesis, anterior-posterior polarity, and body morphology during Caenorhabditis elegans embryogenesis. The Journal of Cell Biology *146*, 439-451.

Shimada, M., Yokosawa, H., and Kawahara, H. (2006). OMA-1 is a P granules-associated protein that is required for germline specification in Caenorhabditis elegans embryos. Genes Cells *11*, 383-396.

Skop, A.R., and White, J.G. (1998). The dynactin complex is required for cleavage plane specification in early Caenorhabditis elegans embryos. Curr Biol *8*, 1110-1116.

Spike, C., Meyer, N., Racen, E., Orsborn, A., Kirchner, J., Kuznicki, K., Yee, C., Bennett, K., and Strome, S. (2008a). Genetic analysis of the Caenorhabditis elegans GLH family of P-granule proteins. Genetics *178*, 1973-1987.

Spike, C.A., Bader, J., Reinke, V., and Strome, S. (2008b). DEPS-1 promotes P-granule assembly and RNA interference in C. elegans germ cells. Development *135*, 983-993.

Spirov, A., Fahmy, K., Schneider, M., Frei, E., Noll, M., and Baumgartner, S. (2009). Formation of the bicoid morphogen gradient: an mRNA gradient dictates the protein gradient. Development *136*, 605-614.

Srinivasan, D.G., Fisk, R.M., Xu, H., and van den Heuvel, S. (2003). A complex of LIN-5 and GPR proteins regulates G protein signaling and spindle function in C elegans. Genes Dev *17*, 1225-1239.

Strigini, M., and Cohen, S.M. (2000). Wingless gradient formation in the Drosophila wing. Curr Biol *10*, 293-300.

Strome, S. (2005). Specification of the germ line. WormBook : the online review of C elegans biology, 1-10.

Strome, S., and Lehmann, R. (2007). Germ versus soma decisions: lessons from flies and worms. Science *316*, 392-393.

Strome, S., and Wood, W.B. (1982). Immunofluorescence visualization of germ-line-specific cytoplasmic granules in embryos, larvae, and adults of Caenorhabditis elegans. Proc Natl Acad Sci USA *79*, 1558-1562.

Strome, S., and Wood, W.B. (1983). Generation of asymmetry and segregation of germ-line granules in early C. elegans embryos. Cell *35*, 15-25.

Sulston, J.E., Schierenberg, E., White, J.G., and Thomson, J.N. (1983). The embryonic cell lineage of the nematode Caenorhabditis elegans. Dev Biol *100*, 64-119.

Tabara, H., Hill, R.J., Mello, C.C., Priess, J.R., and Kohara, Y. (1999). pos-1 encodes a cytoplasmic zinc-finger protein essential for germline specification in C. elegans. Development *126*, 1-11.

Tabata, T. (2001). Genetics of morphogen gradients. Nat Rev Genet *2*, 620-630.

Tabuse, Y., Izumi, Y., Piano, F., Kemphues, K.J., Miwa, J., and Ohno, S. (1998). Atypical protein kinase C cooperates with PAR-3 to establish embryonic polarity in Caenorhabditis elegans. Development *125*, 3607-3614.

Tenenhaus, C., Schubert, C., and Seydoux, G. (1998). Genetic requirements for PIE-1 localization and inhibition of gene expression in the embryonic germ lineage of Caenorhabditis elegans. Dev Biol *200*, 212-224.

Tenenhaus, C., Subramaniam, K., Dunn, M.A., and Seydoux, G. (2001). PIE-1 is a bifunctional protein that regulates maternal and zygotic gene expression in the embryonic germ line of Caenorhabditis elegans. Genes Dev *15*, 1031-1040.

Timmons, L., and Fire, A. (1998). Specific interference by ingested dsRNA. Nature *395*, 854.

Tsou, M.-F.B., Hayashi, A., and Rose, L.S. (2003). LET-99 opposes Galpha/GPR signaling to generate asymmetry for spindle positioning in response to PAR and MES-1/SRC-1 signaling. Development *130*, 5717-5730.

Turing, A. (1952). The chemical basis of morphogenesis. Philos Trans R Soc Lond 237, 37-72.

Updike, D.L., and Strome, S. (2009). a genomewide rnai screen for genes that affect the stability, distribution and function of P granules in Caenorhabditis elegans. Genetics *183*, 1397-1419.

Wang, L., Eckmann, C.R., Kadyk, L.C., Wickens, M., and Kimble, J. (2002). A regulatory cytoplasmic poly(A) polymerase in Caenorhabditis elegans. Nature *419*, 312-316.

Watts, J.L., Etemad-Moghadam, B., Guo, S., Boyd, L., Draper, B.W., Mello, C.C., Priess, J.R., and Kemphues, K.J. (1996). par-6, a gene involved in the establishment of asymmetry in early C. elegans embryos, mediates the asymmetric localization of PAR-3. Development *122*, 3133-3140.

Weil, T.T., Forrest, K.M., and Gavis, E.R. (2006). Localization of bicoid mRNA in late oocytes is maintained by continual active transport. Dev Cell *11*, 251-262.

Wickens, M., Bernstein, D.S., Kimble, J., and Parker, R. (2002). A PUF family portrait: 3'UTR regulation as a way of life. Trends Genet *18*, 150-157.

Yu, S.R., Burkhardt, M., Nowak, M., Ries, J., Petrásek, Z., Scholpp, S., Schwille, P., and Brand, M. (2009). Fgf8 morphogen gradient forms by a source-sink mechanism with freely diffusing molecules. Nature *461*, 533-536.

Zhang, B., Gallegos, M., Puoti, A., Durkin, E., Fields, S., Kimble, J., and Wickens, M.P. (1997). A conserved RNA-binding protein that regulates sexual fates in the C. elegans hermaphrodite germ line. Nature *390*, 477-484.

Zhang, F., Barboric, M., Blackwell, T.K., and Peterlin, B.M. (2003). A model of repression: CTD analogs and PIE-1 inhibit transcriptional elongation by P-TEFb. Genes Dev *17*, 748-758.

Zimyanin, V., Lowe, N., and St Johnston, D. (2007). An oskar-dependent positive feedback loop maintains the polarity of the Drosophila oocyte. Curr Biol *17*, 353-359.

6 Appendix

6.1 Abbreviations

°C	degree Celsius
A-P axis	anterior–posterior axis
amp	ampicillin
AU	arbitrary units
BP	bandpass filter
carb	carbenicillin
DMSO	dimethylsulfoxide
DNA	Deoxyribonucleic acid
E. coli	Escherichia coli
EL	embryo length
FCS	Fluorescence Correlation Spectroscopy
FRAP	Fluorescence Recovery After Photobleach
GFP	Green fluorescent protein
hrs	hours
IPTG	isopropyl-β-D-thiogalactoside
kb	kilo-basepair
kDa	kilo-Dalton
LB	Luria-Bertani
Lt	longpass filter
M	molar
mCH	mCherry
MEX-1	muscle excess
$MgCl_2$	magnesium chlorid
min	minutes
ml	millilitre

mm	millimetre
mM	millimolar
mRNA	messenger ribonucleic acid
n	sample size
NaCl	natrium chlorid
NEBD	nuclear envelope breakdown
NGM	Nematode Growth Medium
PBS	phosphate buffered saline
PCR	polymerase chain reaction
PGL-1	P granule abnormality
PIE-1	pharynx and intestine in excess
RNAi	RNA mediate interference
rpm	rounds per minute
SDS	sodium dodecyl sulfate
sec	seconds
tet	tetracycline
λ	lambda
µg	gram
µl	microlitre
µm	micrometer

6.2 Curriculum vitae

Personal details

Name	Anne Göppert, Dipl. Bio
Date of Birth	01. September 1980
Place of Birth	Bad Kreuznach, Germany
Languages	German, English, French

Working experience

Since 03/2007	PhD thesis "Mechanism of asymmetric PIE-1 segregation in *C. elegans* one-cell embryo" Institute of Molecular Pathology Vienna/Austria Supervisor Dr. Cowan
06/2006 – 02/2007	Lab rotation Institute of Molecular Pathology Vienna/Austria Supervisor Prof. Dr. Beug
07/2005 – 04/2006	Diploma thesis "The Tetraspanin CD9 and Signalling in Ovarian Cancer" German Cancer Research Centre Heidelberg/Germany Prof. Altevogt, Department of Cellular Tumour Immunology

Conferences & Courses

2009	"A diffusion-based gradient of the cytoplasmic fate determinant PIE-1 determines asymmetry in one-cell *C. elegans* embryos" 10/2009 poster at the annual Recess of IMP, Vienna/Austria
2009	EMBO practical course: FRET, FLIM, FCS, FRAP and 3D imaging; application to Developmental Biology 04/2009 Biopolis, Singapore/Singapore
2008	Life under (Re)construction PhD Symposium 11/2008, IMP Vienna/Austria, organising committee
2008	"Segregation of Cell Fate During Asymmetric Cell Division" 10/2008 talk at the annual Recess of IMP, Vienna/Austria
2008	"A Posterior Gradient Ensures Asymmetric PIE-1 Segregation" 03/2008 talk at the European *C. elegans* Meeting 2008, Sevilla/Spain
2007	"Coordination of Cortical Polarity and Cytoplasmic Asymmetry" 10/2007 poster at the annual Recess of IMP, Vienna/Austria
2007	"Coordination of Cortical Polarity and Cytoplasmic Asymmetry" 06-07/2007 poster at International *C. elegans* Meeting, Los Angeles/USA

Publication

Meier F, Busch S, Gast D, Göppert A, Altevogt P, Maczey E, Riedle S, Garbe C and Schittek B (2006). The adhesion molecule L1 (CD171) promotes melanoma progression. Int J Cancer: 119(3):549-55.

6.3 Programs for GNU OCTAVE

6.3.1 Single Gradient Calculation

```
load ~/octave/decayfile;
dl=length(decay);
dl=dl+1;

infile=input("linescan file > ","s");
[k,o]=xlsread(infile);
clear o;
kn=k(find(isnan(k(:,1))==0));
clear k;
k=kn(5:(length(kn)-4));
kl=length(k);

decay(dl).file=infile;

## orient anterior = 0

ku=[floor(kl./4):1:floor(3*(kl./4))];
mink=find(k(:,1)==min(k(ku,1)));
maxk=find(k(:,1)==max(k(ku,1)));
if maxk(1)<mink(1)
    k(:,2)=[kl:-1:1];
    k=sortrows(k,2);
elseif mink(1)<maxk(1)
    k(:,2)=[1:1:kl];
endif;

## get rid of p granules

for x=5:kl
    if abs(k(x,1)-k((x-4),1))>=mean(k(:,1))./10
        k(x,1)=mean(k(x-4:x,1));
    endif
endfor;

##  subtract background intensity
##  and standardize intensities (ratio of background)
##  and standardize embryo length to 1

[fr,bn]=hist(k(:,1));
zer=find(fr(:)==max(fr));
MED=bn(zer(1));

k(:,1)=(k(:,1)./MED)-1;
k(:,2)=k(:,2)./max(k(:,2));

decay(dl).points=k;

plot(k(:,2),k(:,1),"go");

## fit curve (X = index; Y = intensity)
```

```
lok=find(k(:,2)>=0.33);
hik=find(k(:,2)<=0.9);
kr=intersect(lok,hik);

[p1,s1]=polyfit(k(kr,2),k(kr,1),1);
p1v=polyval(p1,k(:,2));
r2_1=corrcoef(k(kr,1),polyval(p1v,k(kr,2)));
decay(dl).r2_1=r2_1;

nn=find(k(kr,1)>0);
[lp1,ls1]=polyfit(log(k(kr(nn),2)),log(k(kr(nn),1)),1);
lp1v=polyval(lp1,log(k(:,2)));
logr2_1=corrcoef(log(k(kr(nn),1)),polyval(lp1,log(k(kr(nn),2))))
decay(dl).logr2_1=logr2_1;

## plot fit
hold on;
plot(k(:,2),e.^lp1v(:),"r","linewidth",4);

[p2,s2]=polyfit(k(kr,2),k(kr,1),2);
p2v=polyval(p2,k(:,2));
r2_2=corrcoef(k(kr,1),polyval(p2v,k(kr,2)));
decay(dl).r2_2=r2_2;

[p3,s3]=polyfit(k(kr,2),k(kr,1),3);
p3v=polyval(p3,k(:,2));
r2_3=corrcoef(k(kr,1),polyval(p3v,k(kr,2)));
decay(dl).r2_3=r2_3;

## lambda calculation (index = p*intensity)

ilp1=polyfit(log(k(kr(nn),1)),log(k(kr(nn),2)),1);
mi=find(k(:,1)==max(k(kr,1)));
maxik=log(k(find(k(:,1)==max(k(kr,1))),1)./e);
maxix=polyval(ilp1,maxik);
lambda=(k(mi(1),2))-(e.^maxix)
##lambda=1-(e.^maxix)
decay(dl).lambda=lambda;

hold off;
save ~/octave/decayfile;
```

6.3.2 Time-lapse Gradient Calculation

```
## to calculate lambda from raw linescan data
## distinguishes between multi- & single-column datasets
## requires separate time file (octave variable)
## modified 12/11/2009 crc
## CHANGE TWO ITEMS IN PROGRAM BEFORE RUNNING:
## time=[];  line 12
## file name for save;  line 152

clear;
infile=input("time-lapse linescan file > ","s");
[a,o]=xlsread(infile);

time=[-480:30:180];
clear o;

##can be taken away if there are problems for loading the file
##xa=find(isnan(a((floor(length(a)./2)),:))==0);
##ya=find(isnan(a(:,(floor(size(a,2)./2))))==0);
##a=a(ya,xa);


sa=size(a);
close all;

if sa(2)>=6
    ay=1;
    for y=1:sa(2)
        fii=find(isnan(a(:,y))==0);
        if length(fii)>=1
            an(1,ay)=time(ay);
            an(2:(length(fii)+1),ay)=a(fii,y);
            ay=ay+1;
        else
            ay=ay+1;
        endif
    endfor
elseif sa(2)<=5
    ay=1;
    fii=find(isnan(a(:,1))==1);
    fii=[fii;length(a)+1];
    for r=1:(length(fii)-1)
##changed from for r=1:(length(fii)-4) - maybe missing final time point? 11.11.2009
        if length(find(fii(:)==fii(r)+1))<1
            an(1,ay)=time(ay);
            tmp=a((fii(r)+1):(fii(r+1)-1),1);
            an(2:(length(tmp)+1),ay)=tmp;
            ay=ay+1;
            clear tmp;
        endif
    endfor
endif

clear a;
aw=size(an,2);
al=length(an);

## eliminate any zeroes / empty spaces

off=al;
for q=1:aw
    ff=min(find(an(2:al,q)==0));
    if ff<off
        off=ff;
    endif
endfor
```

```
t=an(1,:);
a=an(6:(off-4),:);
al=length(a);

## orient anterior = 0
for aX=1:aw
    n=find(a(ar,aX)>0);
    ilp1=polyfit(log(a(ar(n),aX)),log(a(ar(n),aw+1)),1);
    mi=find(a(:,aX)==max(a(ar,aX)));
    maxia=log(a(mi(1),aX)./e);
    maxix=polyval(ilp1,maxia);
    lamba=a(mi(1),aw+1)-(e.^maxix);
    logr2=corrcoef(log(a(ar(n),aw+1)),polyval(ilp1,log(a(ar(n),aX))));
    pieT(aX).time=t(aX);
    pieT(aX).max=a(mi(1),aX);
    pieT(aX).decay=lamba;
    pieT(aX).fit=logr2;

## get rid of p granules
    F1l=polyfit(log(a(ar(n),aw+1)),log(a(ar(n),aX)),1);
    c1l=corrcoef(log(a(ar(n),aX)),polyval(F1l,log(a(ar(n),aw+1))));
for xx=1:aw
    for x=5:al
    fitty=e.^(polyval(F1l,log(rng)));
## change the "c1l" value below to change stringency of fit
    if c1l>=0.75
        if abs(a(x,xx)-a(x-4),xx))>=mean(a(:,xx))./10
        a(x,xx)=mean(a(x-4:x,xx));
        endif
        plot(rng,fitty,"m","linewidth",3);
        hold on;
    endfor;
endfor
    else
        plot(rng,fitty,"c","linewidth",3);
        hold on;
    endif;
##  subtract background intensity
##  and standardize intensities (ratio of background)
    axis([0 1 0 2]);
##  and standardize embryo length to 1

    pieT(aX).curve=fitty;
[fr,bn]=hist(a(:,aw));
    clear lamba logr2 ilp* maxix fitty
zer=find(fr(:)==max(fr));
endfor;
MED=bn(zer(1));

for u=1:length(pieT)
for y=1:aw
    dc(u)=pieT(u).decay;
    a(:,y)=(a(:,y)./MED)-1;
    ft(u)=pieT(u).fit;
endfor
    ti(u)=pieT(u).time;
endfor;
a(:,aw+1)=a(:,aw+1)./max(a(:,aw+1));

save -ascii 25-3data ti dc ft
figure(20);
plot(a(:,aw+1),a(:,1:aw),"bs");

## fit curve (X = intensity; Y = index)
## lambda calculation (index = p*intensity)

loa=find(a(:,aw+1)>=0.33);
hia=find(a(:,aw+1)<=0.9);
ar=intersect(loa,hia);
rng=[.33:.01:1];

figure(22);
hold off;

for aX=1:aw
    n=find(a(ar,aX)>0);
    ilp1=polyfit(log(a(ar(n),aX)),log(a(ar(n),aw+1)),1);
    mi=find(a(:,aX)==max(a(ar,aX)));
    maxia=log(a(mi(1),aX)./e);
    maxix=polyval(ilp1,maxia);
    lamba=a(mi(1),aw+1)-(e.^maxix);
    logr2=corrcoef(log(a(ar(n),aw+1)),polyval(ilp1,log(a(ar(n),aX))));
```

6.4 Graphs

6.4.1 Region measurements

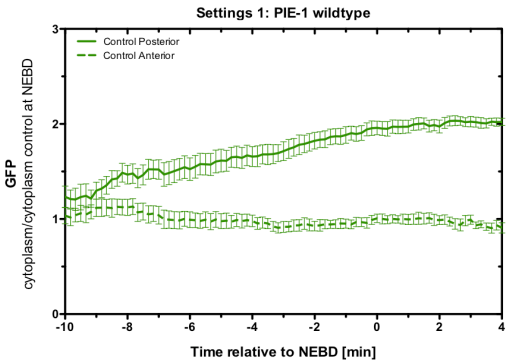

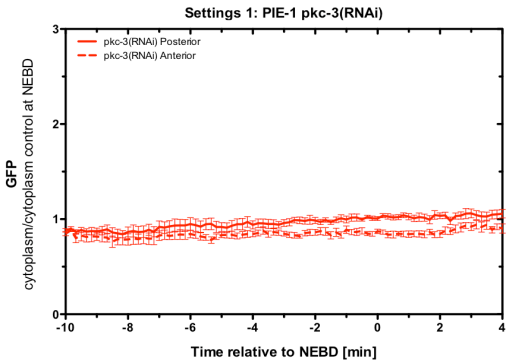

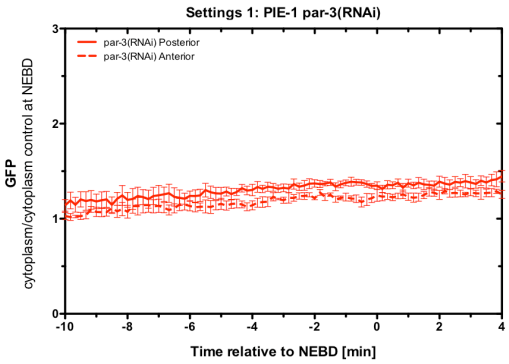

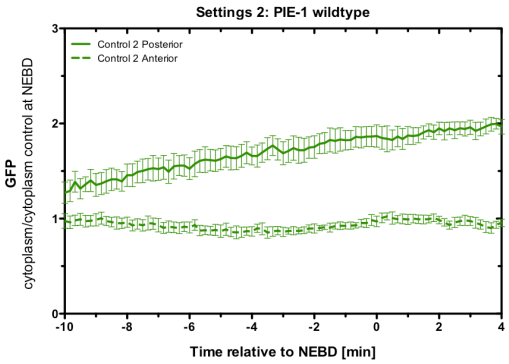

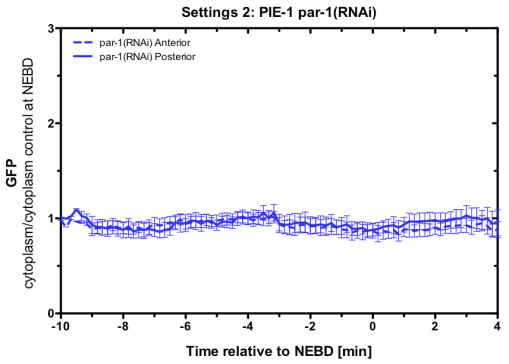

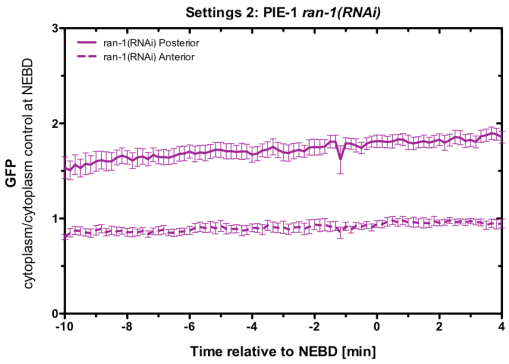

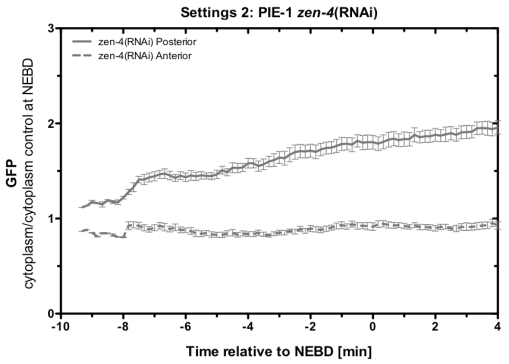

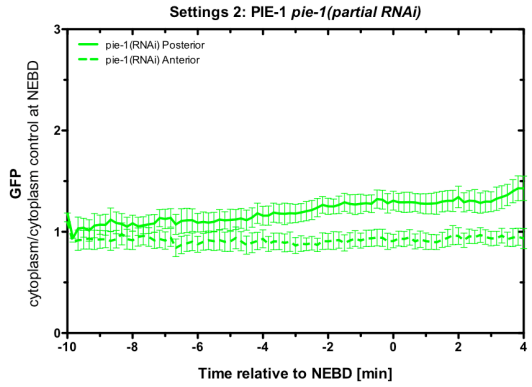
Settings 2: PIE-1 pie-1(partial RNAi)
pie-1(RNAi) Posterior
pie-1(RNAi) Anterior
GFP
cytoplasm/cytoplasm control at NEBD
Time relative to NEBD [min]

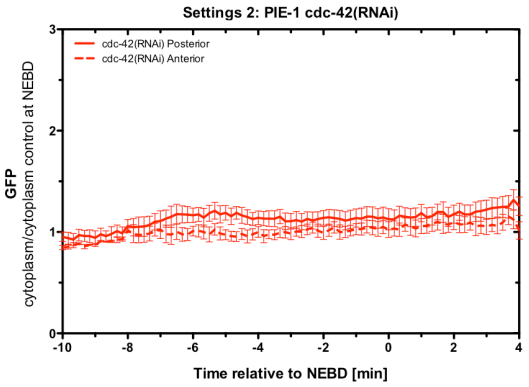
Settings 2: PIE-1 cdc-42(RNAi)
cdc-42(RNAi) Posterior
cdc-42(RNAi) Anterior
GFP
cytoplasm/cytoplasm control at NEBD
Time relative to NEBD [min]

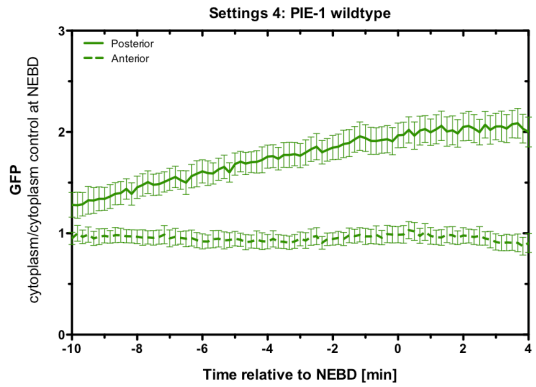
Settings 4: PIE-1 wildtype
Posterior
Anterior
GFP
cytoplasm/cytoplasm control at NEBD
Time relative to NEBD [min]

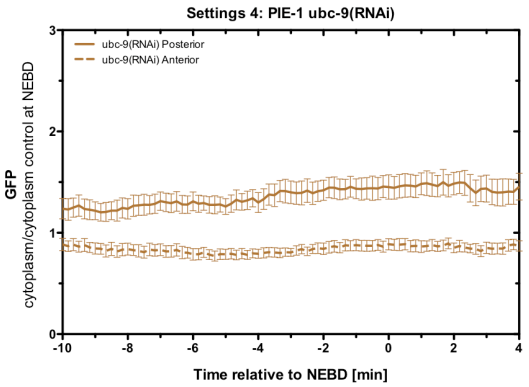
Settings 4: PIE-1 ubc-9(RNAi)
ubc-9(RNAi) Posterior
ubc-9(RNAi) Anterior
GFP
cytoplasm/cytoplasm control at NEBD
Time relative to NEBD [min]

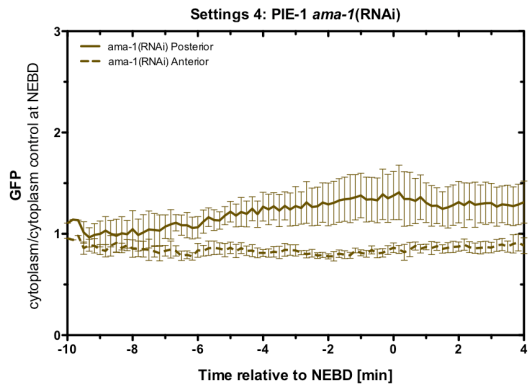
Settings 4: PIE-1 ama-1(RNAi)
ama-1(RNAi) Posterior
ama-1(RNAi) Anterior
GFP
cytoplasm/cytoplasm control at NEBD
Time relative to NEBD [min]

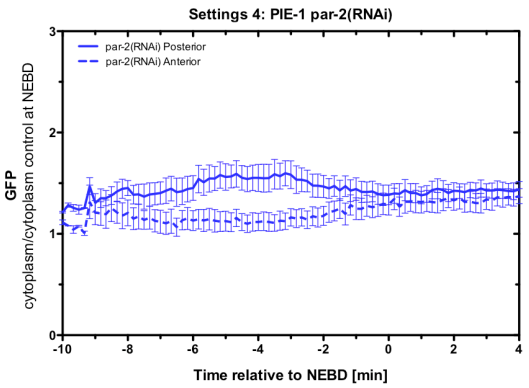
Settings 4: PIE-1 par-2(RNAi)
par-2(RNAi) Posterior
par-2(RNAi) Anterior
GFP
cytoplasm/cytoplasm control at NEBD
Time relative to NEBD [min]

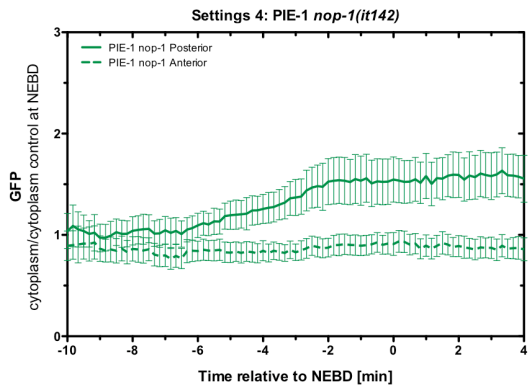
Settings 4: PIE-1 nop-1(it142)
PIE-1 nop-1 Posterior
PIE-1 nop-1 Anterior
GFP
cytoplasm/cytoplasm control at NEBD
Time relative to NEBD [min]

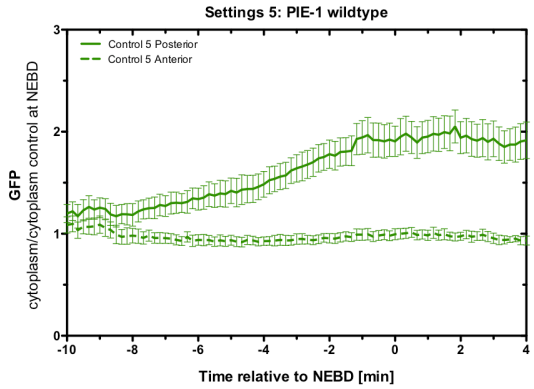
Settings 5: PIE-1 wildtype
Control 5 Posterior
Control 5 Anterior
GFP
cytoplasm/cytoplasm control at NEBD
Time relative to NEBD [min]

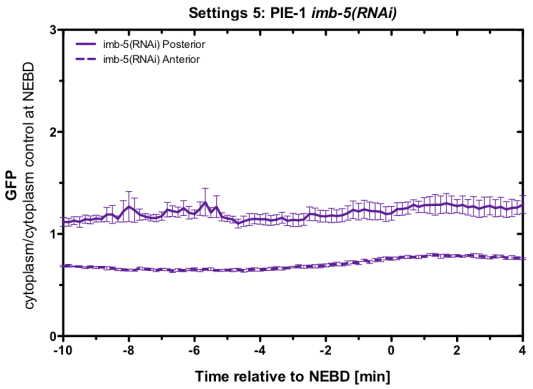
Settings 5: PIE-1 imb-5(RNAi)
imb-5(RNAi) Posterior
imb-5(RNAi) Anterior
GFP
cytoplasm/cytoplasm control at NEBD
Time relative to NEBD [min]

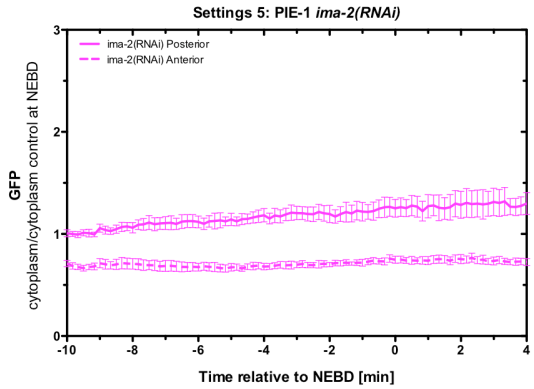
Settings 5: PIE-1 ima-2(RNAi)
ima-2(RNAi) Posterior
ima-2(RNAi) Anterior
GFP
cytoplasm/cytoplasm control at NEBD
Time relative to NEBD [min]

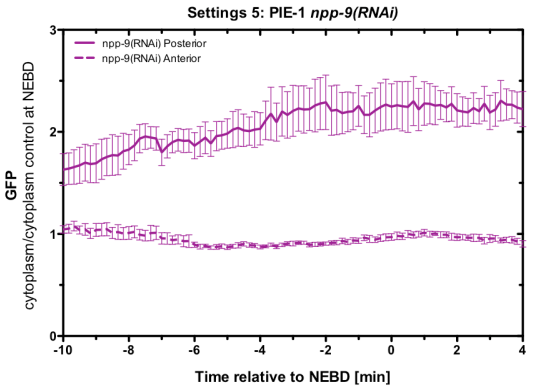
Settings 5: PIE-1 npp-9(RNAi)
npp-9(RNAi) Posterior
npp-9(RNAi) Anterior
GFP
cytoplasm/cytoplasm control at NEBD
Time relative to NEBD [min]

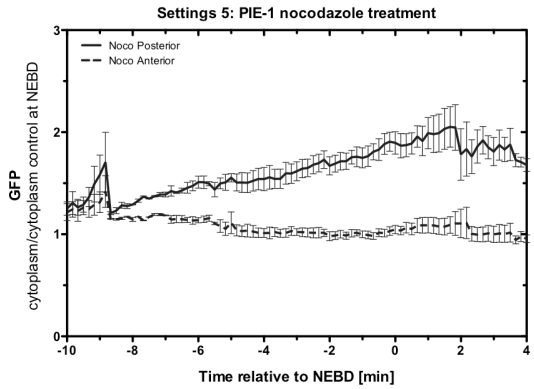
Settings 5: PIE-1 nocodazole treatment
Noco Posterior
Noco Anterior
GFP
cytoplasm/cytoplasm control at NEBD
Time relative to NEBD [min]

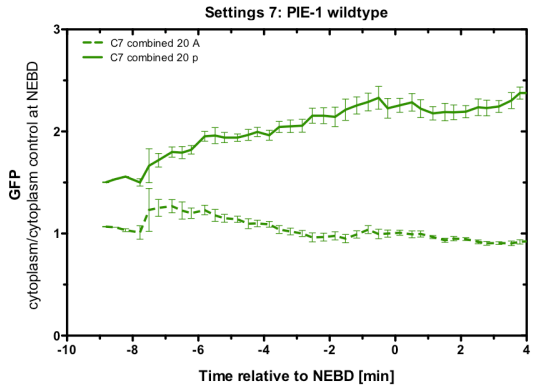
Settings 7: PIE-1 wildtype
C7 combined 20 A
C7 combined 20 p
GFP
cytoplasm/cytoplasm control at NEBD
Time relative to NEBD [min]

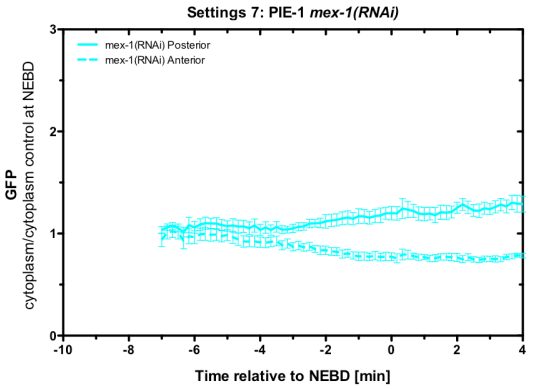
Settings 7: PIE-1 mex-1(RNAi)
mex-1(RNAi) Posterior
mex-1(RNAi) Anterior
GFP
cytoplasm/cytoplasm control at NEBD
Time relative to NEBD [min]

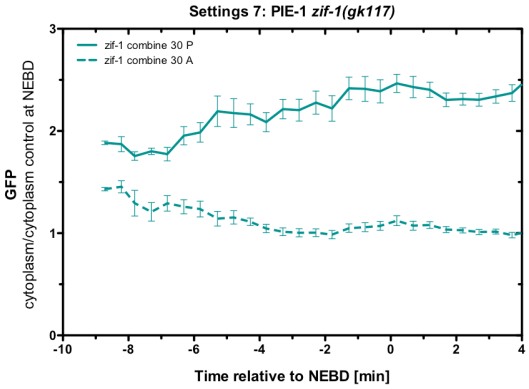

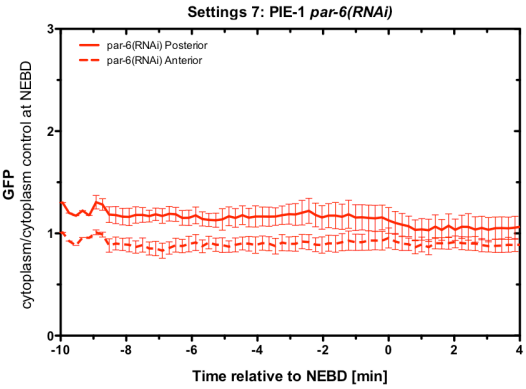

6.4.2 Gradient shape

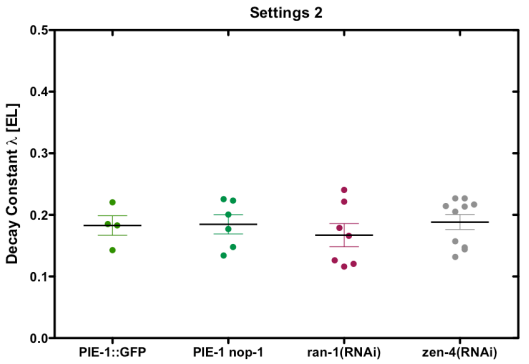

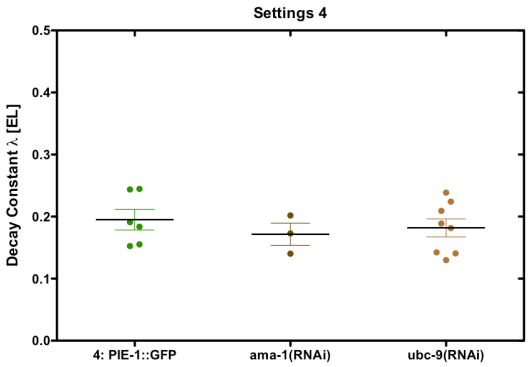

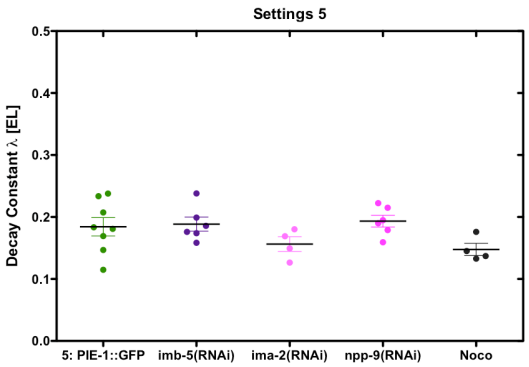

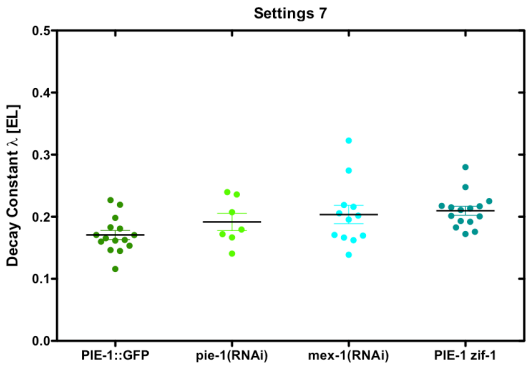

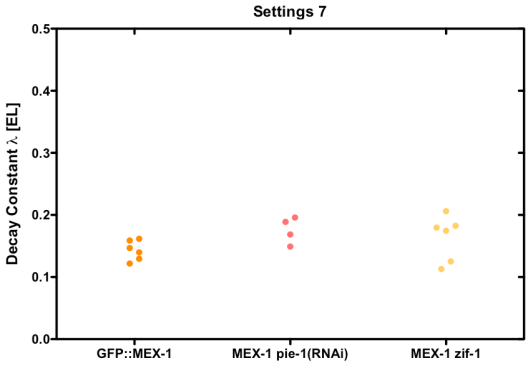

6.4.3 Gradient formation

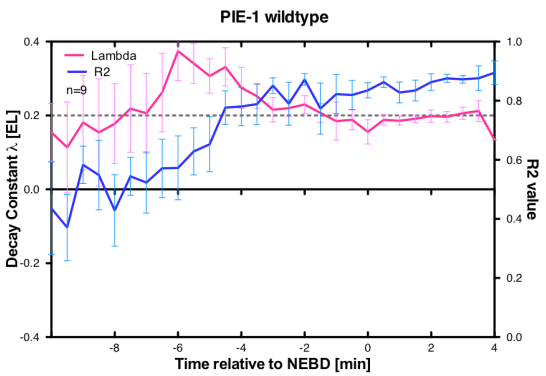

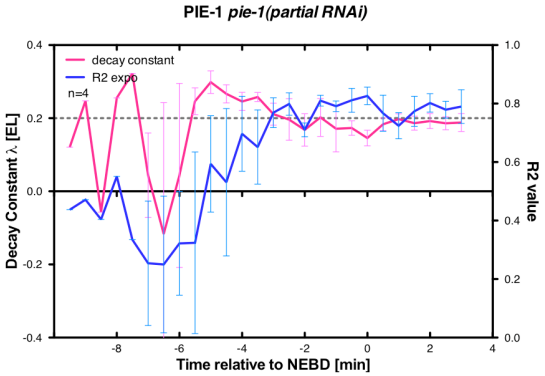

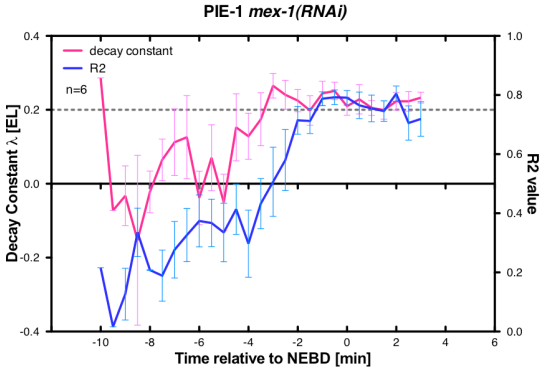

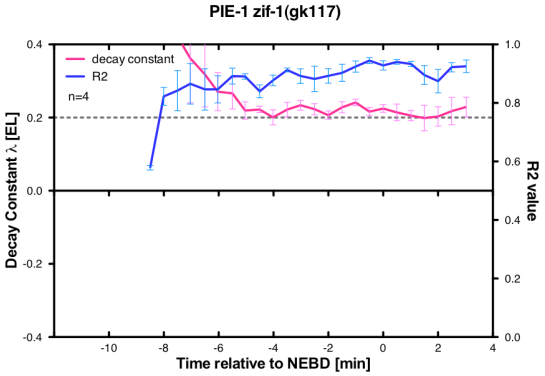

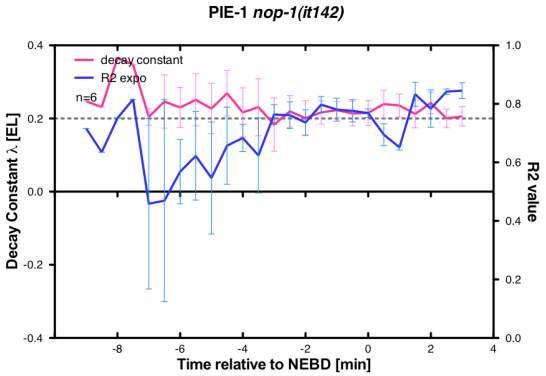

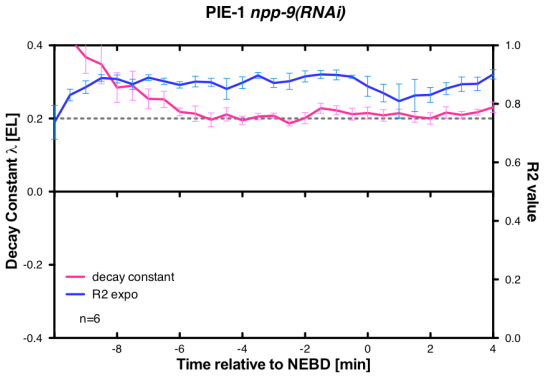

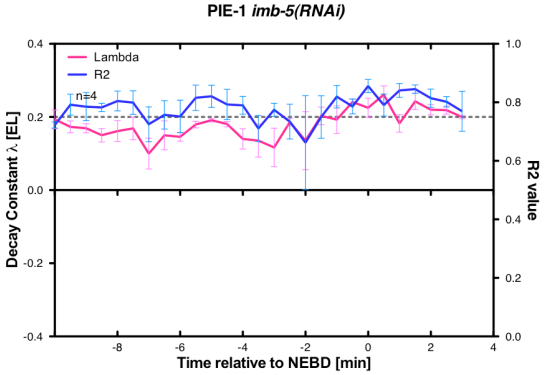

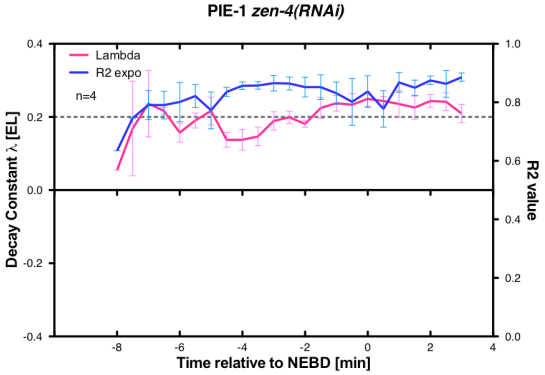

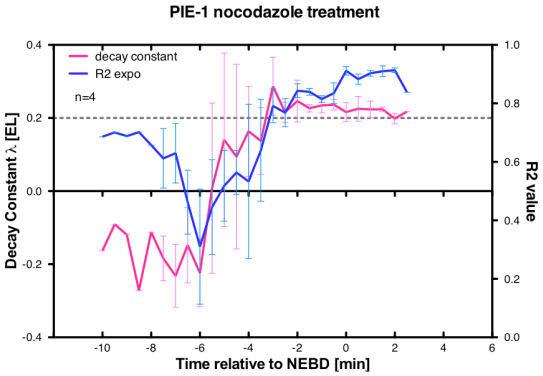
PIE-1 nocodazole treatment
decay constant
R2 expo
n=4
Decay Constant λ [EL]
R2 value
Time relative to NEBD [min]

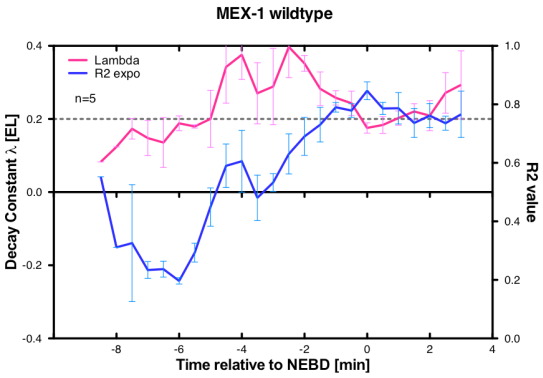
MEX-1 wildtype
Lambda
R2 expo
n=5
Decay Constant λ [EL]
R2 value
Time relative to NEBD [min]

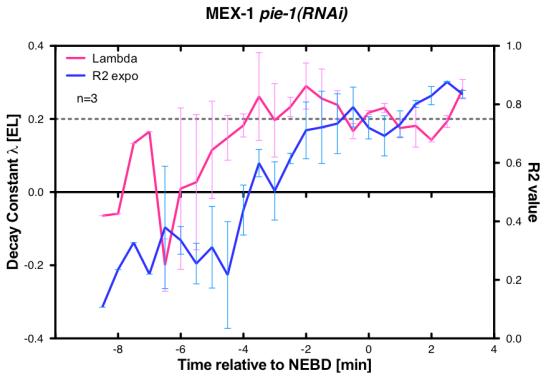
MEX-1 pie-1(RNAi)
Lambda
R2 expo
n=3
Decay Constant λ [EL]
R2 value
Time relative to NEBD [min]

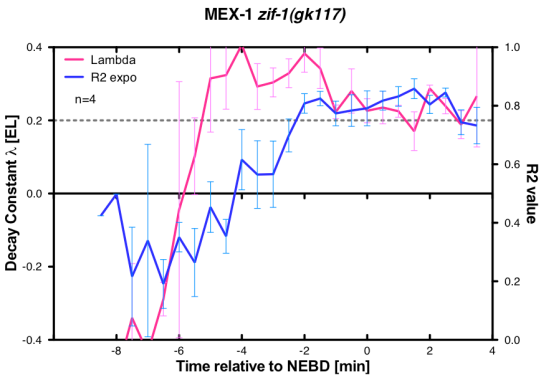
MEX-1 zif-1(gk117)
Lambda
R2 expo
n=4
Decay Constant λ [EL]
R2 value
Time relative to NEBD [min]

6.4.4 P granule size and number

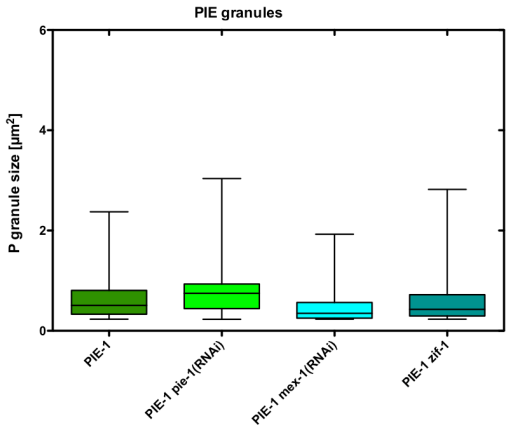

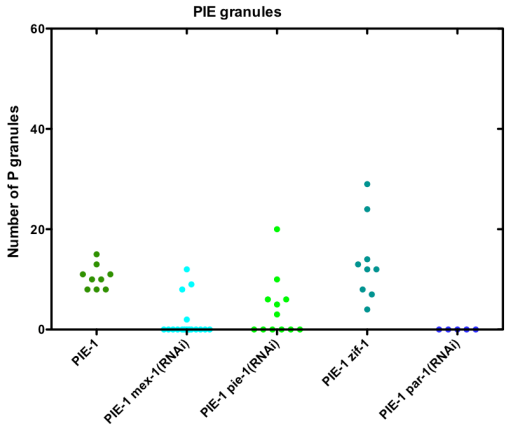

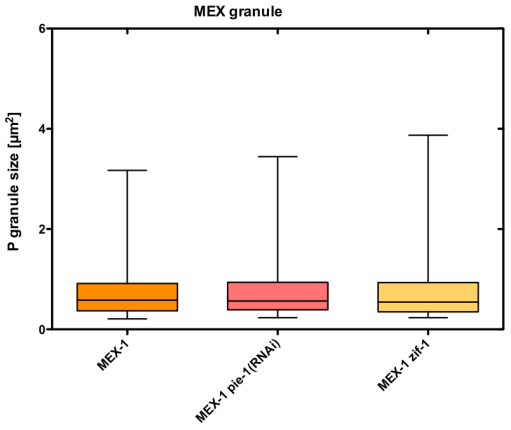

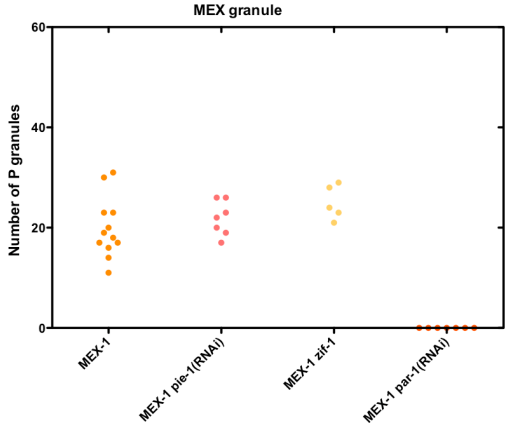

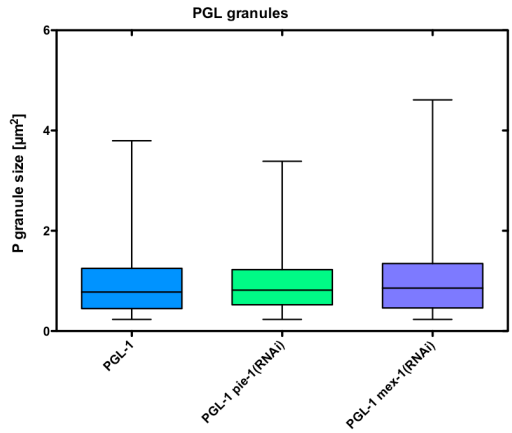

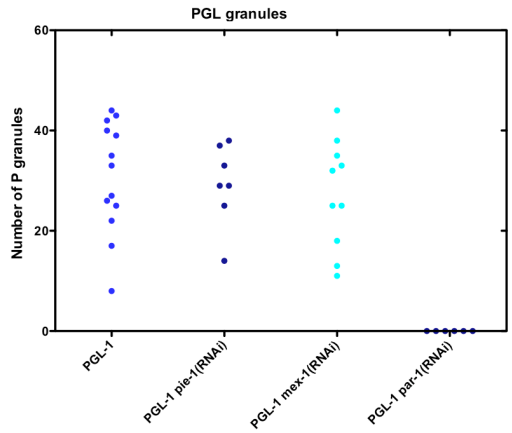

6.4.5 GFP Profiles along the anterior–posterior axis

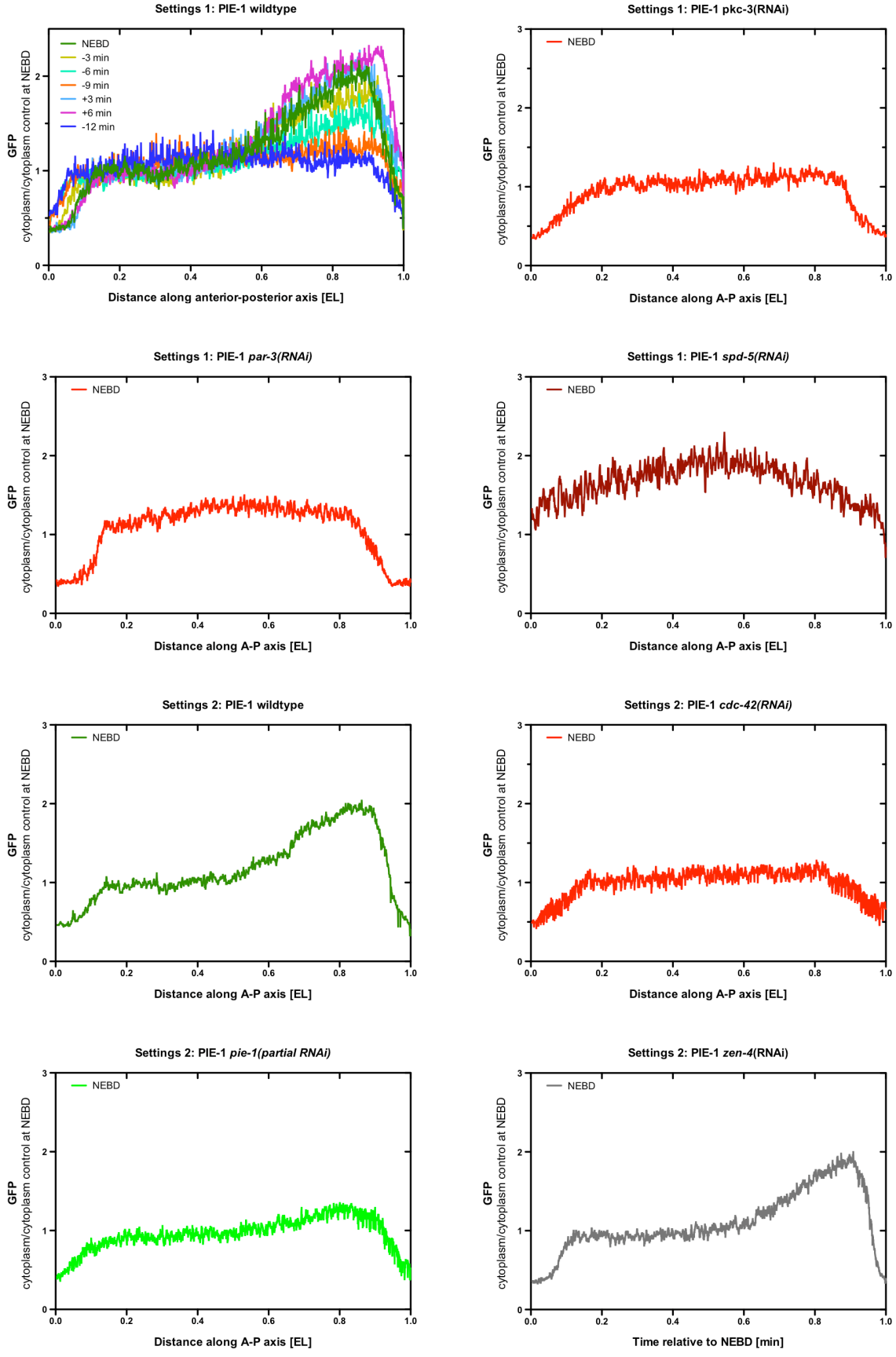

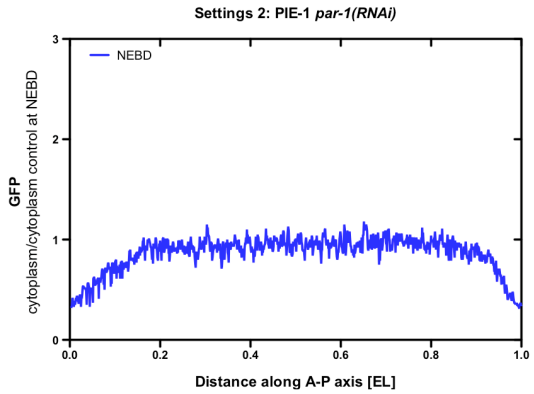
Settings 2: PIE-1 par-1(RNAi)
NEBD
GFP
cytoplasm/cytoplasm control at NEBD
Distance along A-P axis [EL]

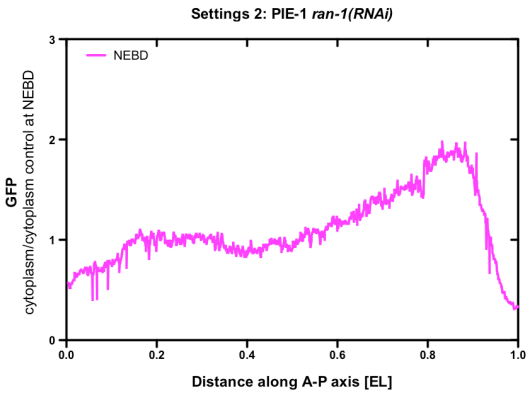
Settings 2: PIE-1 ran-1(RNAi)
NEBD
GFP
cytoplasm/cytoplasm control at NEBD
Distance along A-P axis [EL]

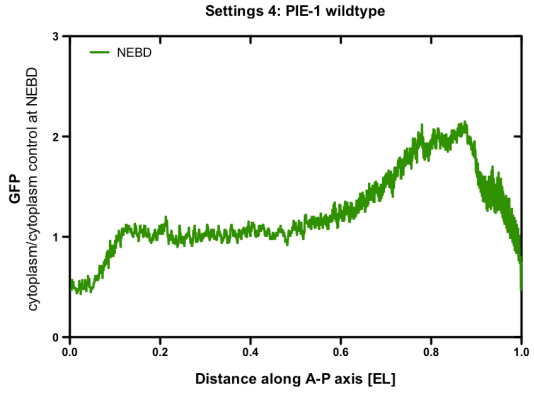
Settings 4: PIE-1 wildtype
NEBD
GFP
cytoplasm/cytoplasm control at NEBD
Distance along A-P axis [EL]

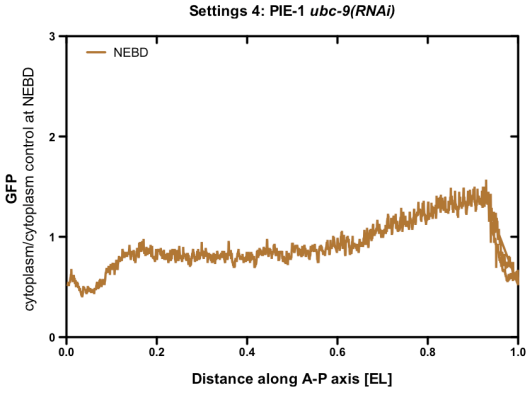
Settings 4: PIE-1 ubc-9(RNAi)
NEBD
GFP
cytoplasm/cytoplasm control at NEBD
Distance along A-P axis [EL]

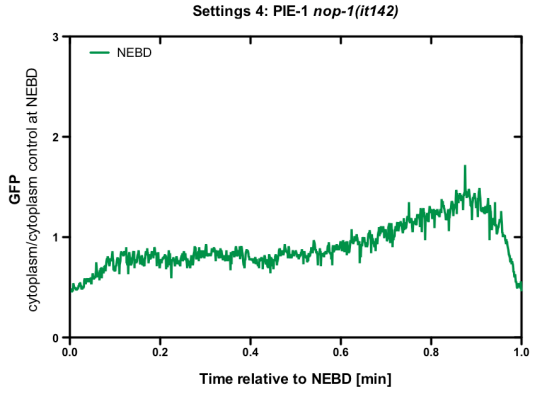
Settings 4: PIE-1 nop-1(it142)
NEBD
GFP
cytoplasm/cytoplasm control at NEBD
Time relative to NEBD [min]

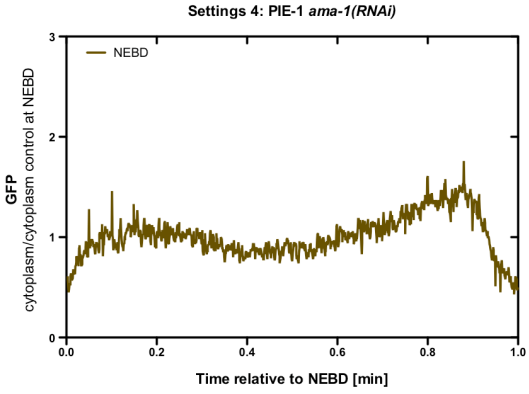
Settings 4: PIE-1 ama-1(RNAi)
NEBD
GFP
cytoplasm/cytoplasm control at NEBD
Time relative to NEBD [min]

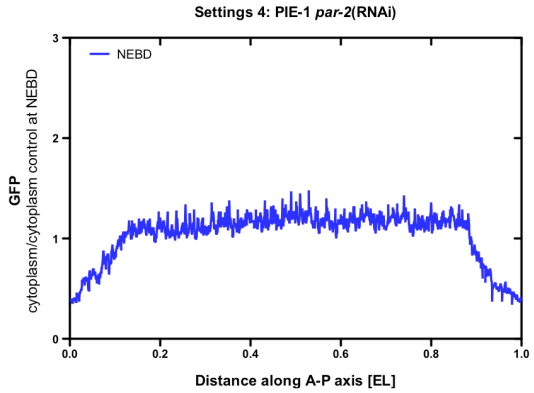
Settings 4: PIE-1 par-2(RNAi)
NEBD
GFP
cytoplasm/cytoplasm control at NEBD
Distance along A-P axis [EL]

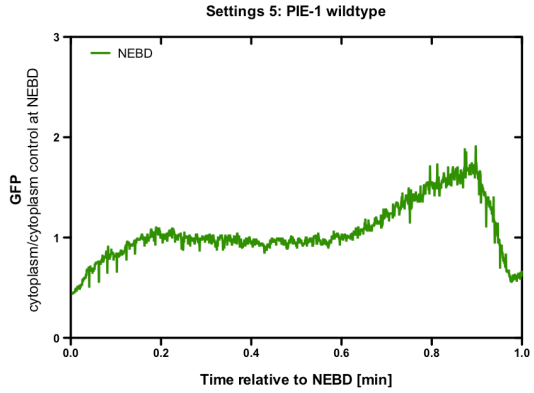
Settings 5: PIE-1 wildtype
NEBD
GFP
cytoplasm/cytoplasm control at NEBD
Time relative to NEBD [min]

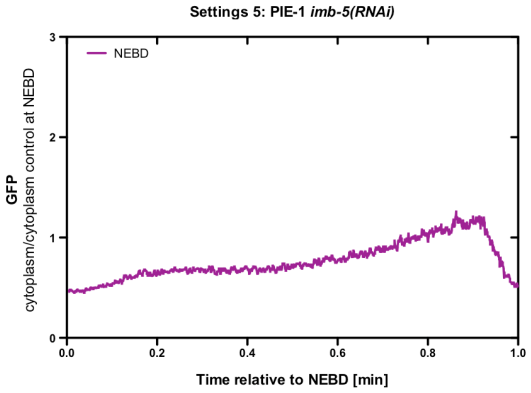
Settings 5: PIE-1 imb-5(RNAi)
NEBD
GFP
cytoplasm/cytoplasm control at NEBD
Time relative to NEBD [min]

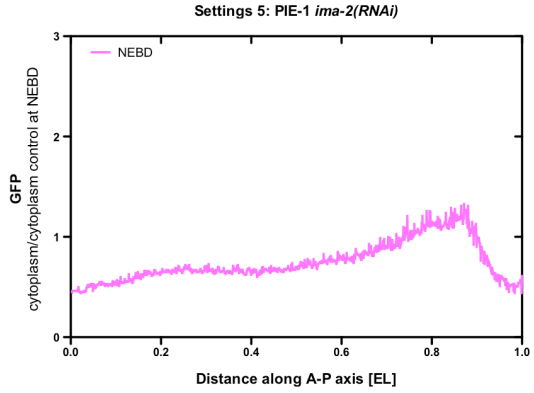
Settings 5: PIE-1 ima-2(RNAi)
NEBD
GFP
cytoplasm/cytoplasm control at NEBD
Distance along A-P axis [EL]

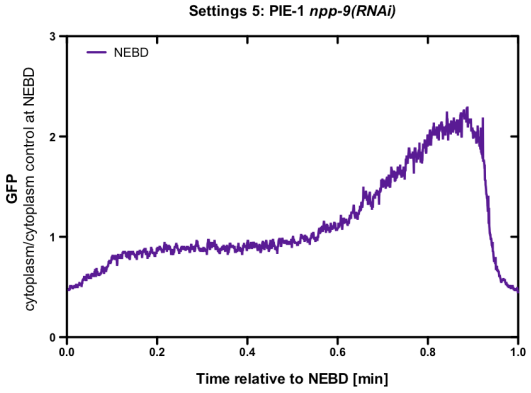
Settings 5: PIE-1 npp-9(RNAi)
NEBD
GFP
cytoplasm/cytoplasm control at NEBD
Time relative to NEBD [min]

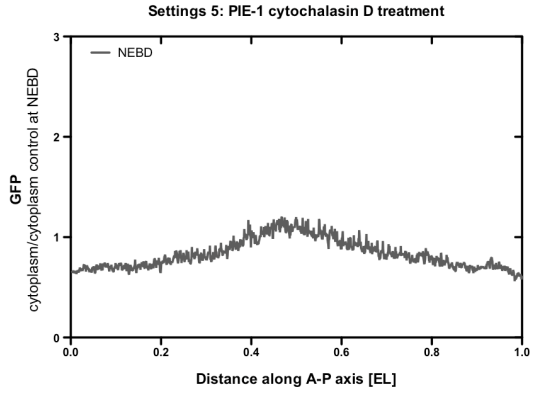
Settings 5: PIE-1 cytochalasin D treatment
NEBD
GFP
cytoplasm/cytoplasm control at NEBD
Distance along A-P axis [EL]

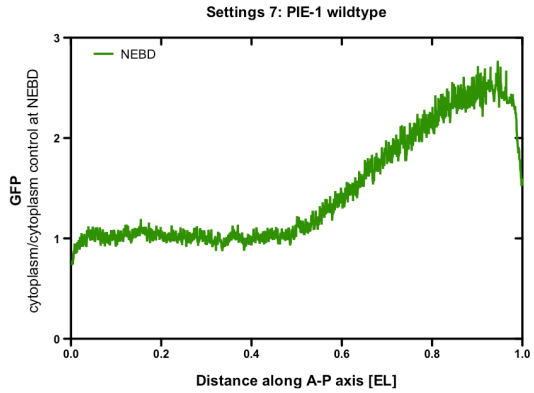
Settings 7: PIE-1 wildtype
NEBD
GFP
cytoplasm/cytoplasm control at NEBD
Distance along A-P axis [EL]

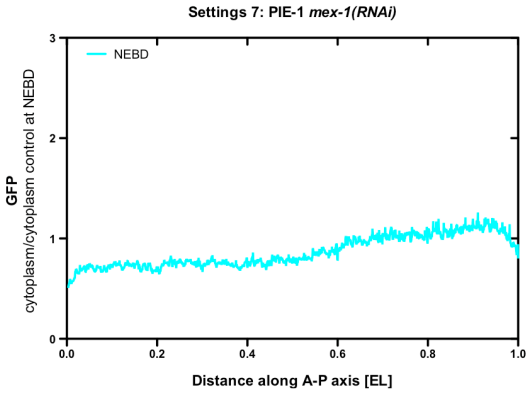
Settings 7: PIE-1 mex-1(RNAi)
NEBD
GFP
cytoplasm/cytoplasm control at NEBD
Distance along A-P axis [EL]

6.4.6 Posterior enrichment

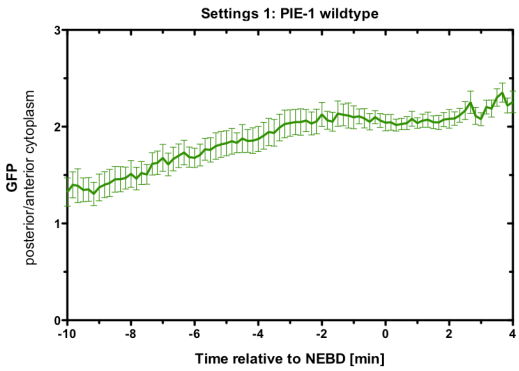

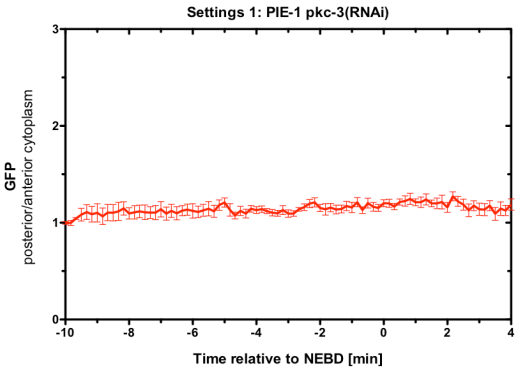

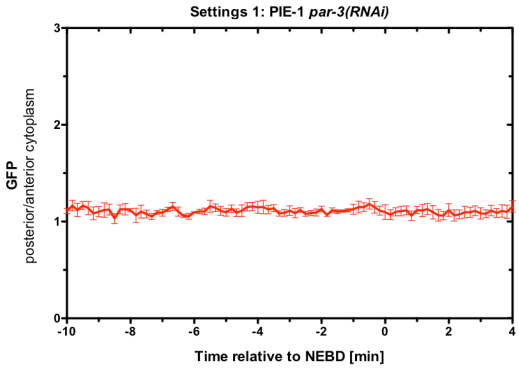

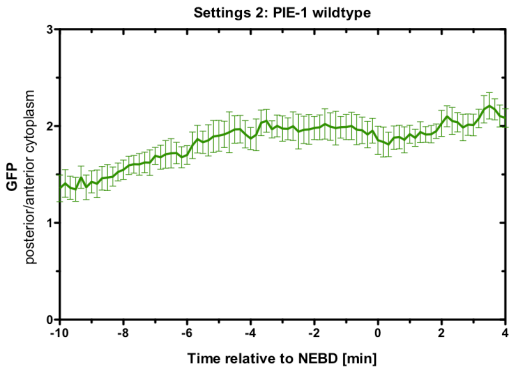

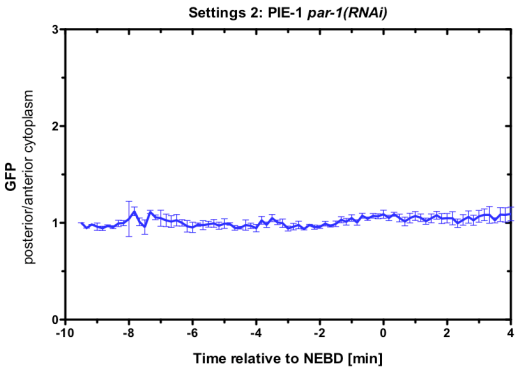

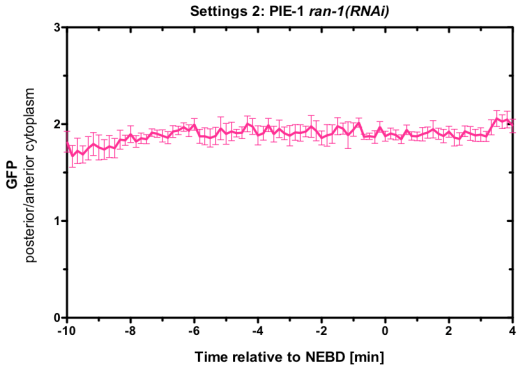

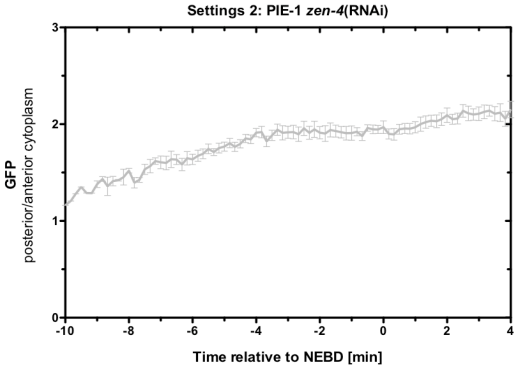

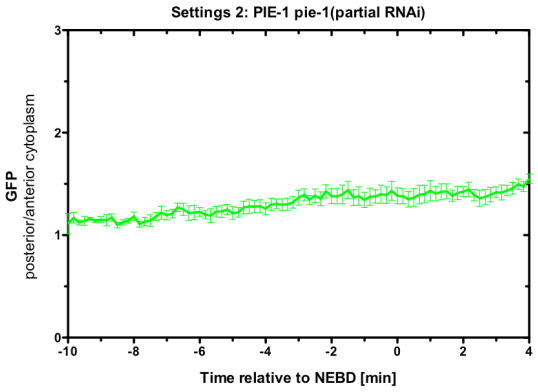
Settings 2: PIE-1 pie-1(partial RNAi)
GFP
posterior/anterior cytoplasm
Time relative to NEBD [min]

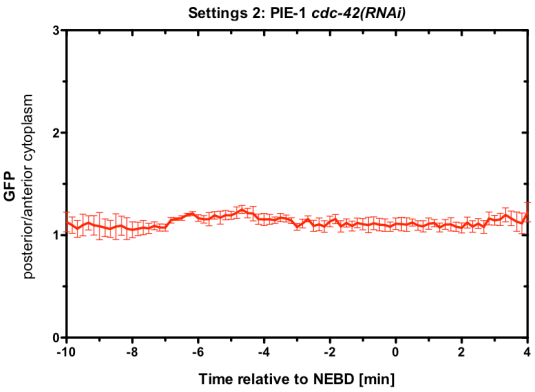
Settings 2: PIE-1 cdc-42(RNAi)
GFP
posterior/anterior cytoplasm
Time relative to NEBD [min]

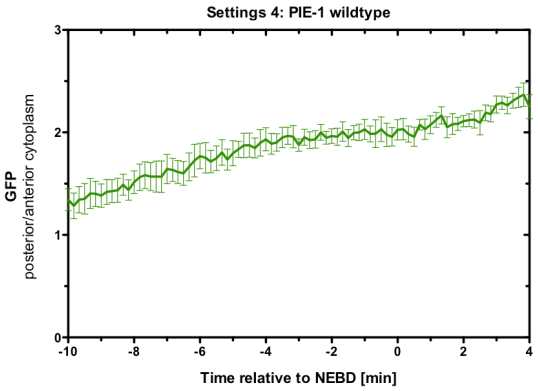
Settings 4: PIE-1 wildtype
GFP
posterior/anterior cytoplasm
Time relative to NEBD [min]

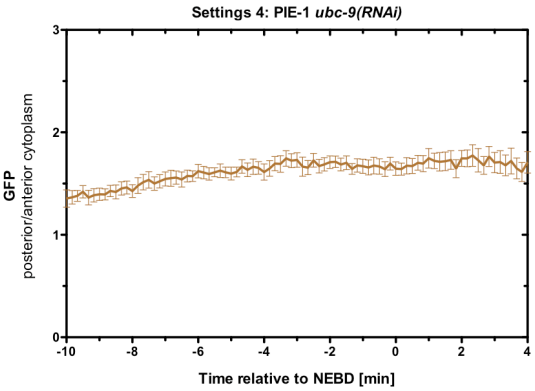
Settings 4: PIE-1 ubc-9(RNAi)
GFP
posterior/anterior cytoplasm
Time relative to NEBD [min]

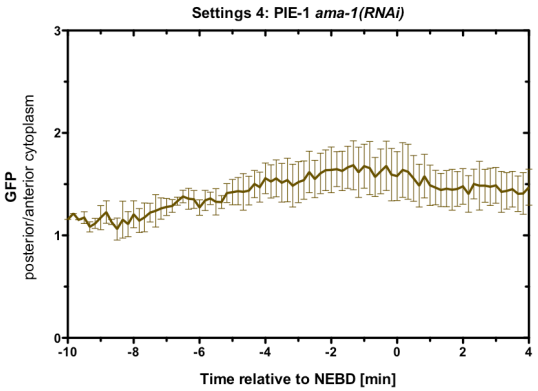
Settings 4: PIE-1 ama-1(RNAi)
GFP
posterior/anterior cytoplasm
Time relative to NEBD [min]

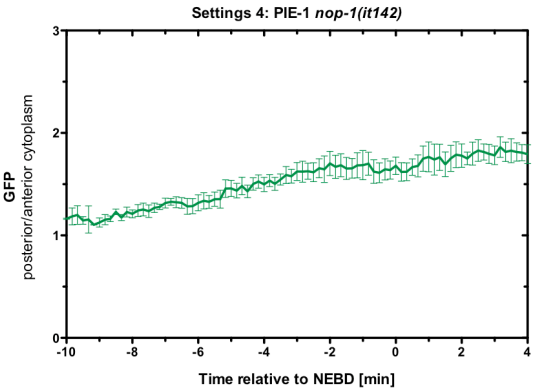
Settings 4: PIE-1 nop-1(it142)
GFP
posterior/anterior cytoplasm
Time relative to NEBD [min]

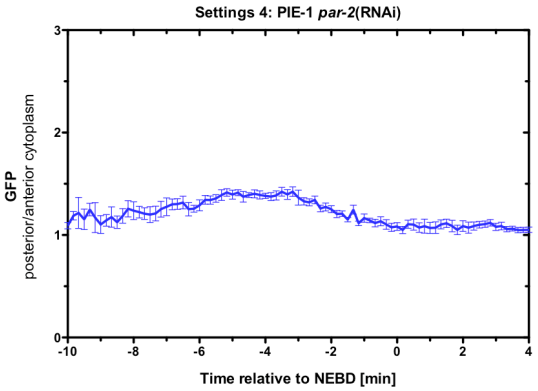
Settings 4: PIE-1 par-2(RNAi)
GFP
posterior/anterior cytoplasm
Time relative to NEBD [min]

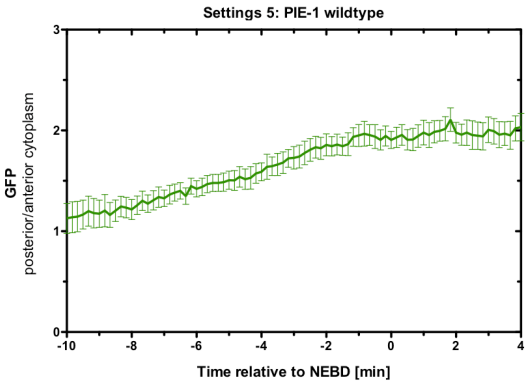
Settings 5: PIE-1 wildtype
GFP
posterior/anterior cytoplasm
Time relative to NEBD [min]

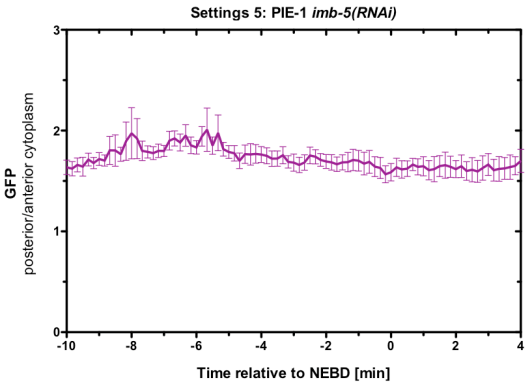
Settings 5: PIE-1 imb-5(RNAi)
GFP
posterior/anterior cytoplasm
Time relative to NEBD [min]

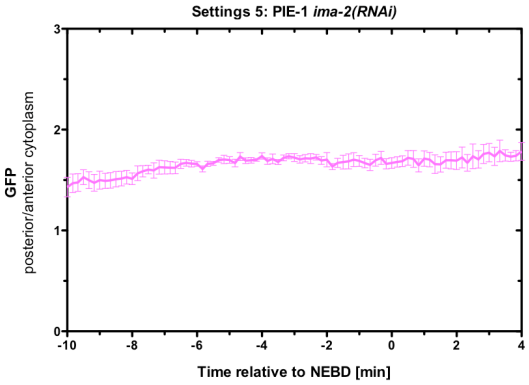
Settings 5: PIE-1 ima-2(RNAi)
GFP
posterior/anterior cytoplasm
Time relative to NEBD [min]

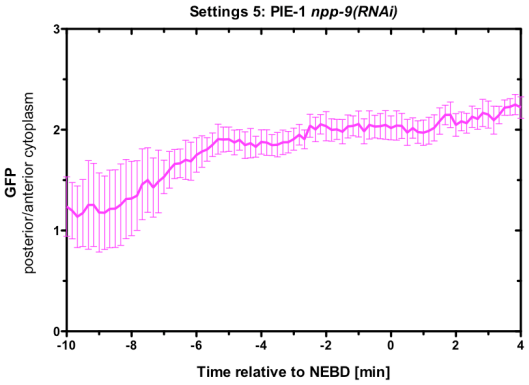
Settings 5: PIE-1 npp-9(RNAi)
GFP
posterior/anterior cytoplasm
Time relative to NEBD [min]

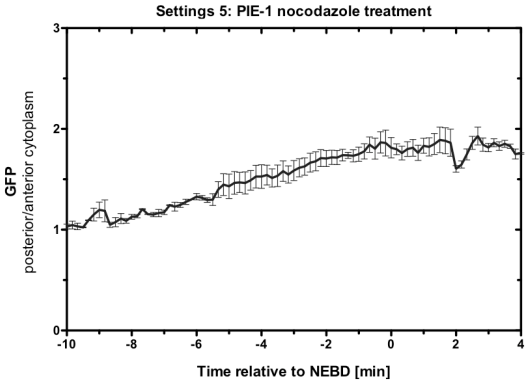
Settings 5: PIE-1 nocodazole treatment
GFP
posterior/anterior cytoplasm
Time relative to NEBD [min]

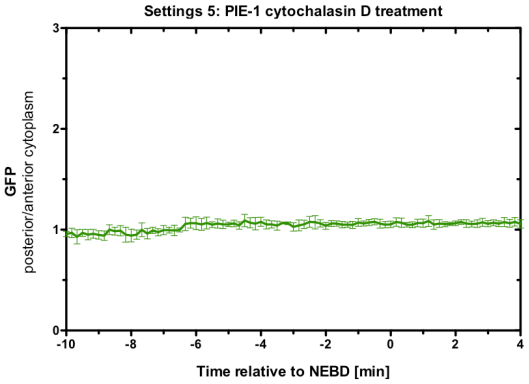
Settings 5: PIE-1 cytochalasin D treatment
GFP
posterior/anterior cytoplasm
Time relative to NEBD [min]

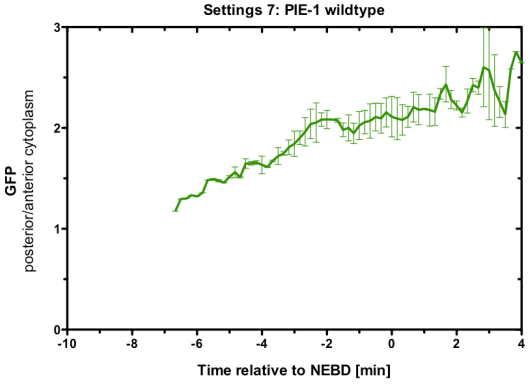
Settings 7: PIE-1 wildtype
GFP
posterior/anterior cytoplasm
Time relative to NEBD [min]

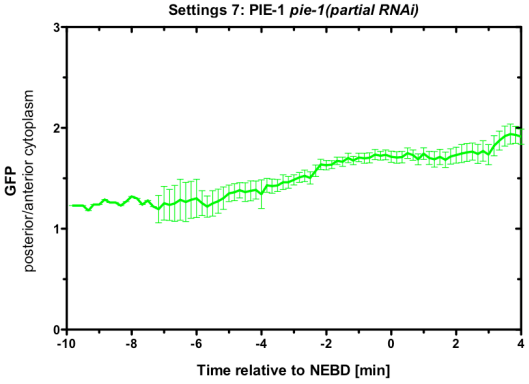
Settings 7: PIE-1 pie-1(partial RNAi)
GFP
posterior/anterior cytoplasm
Time relative to NEBD [min]

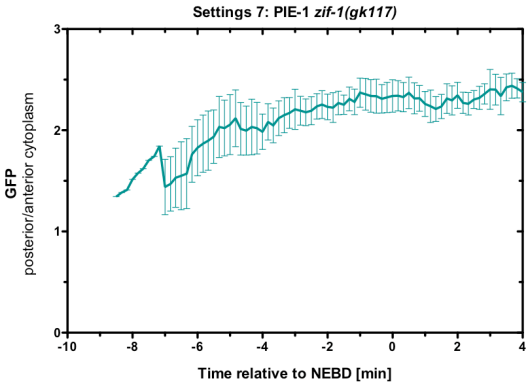
Settings 7: PIE-1 zif-1(gk117)
GFP
posterior/anterior cytoplasm
Time relative to NEBD [min]

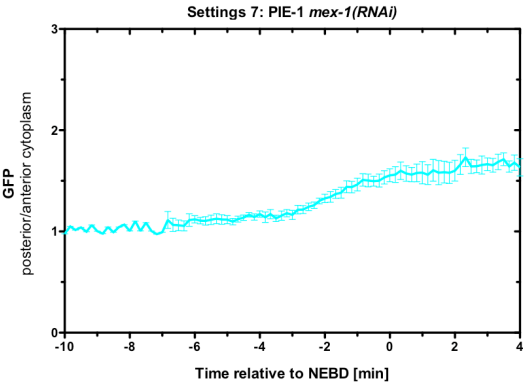
Settings 7: PIE-1 mex-1(RNAi)
GFP
posterior/anterior cytoplasm
Time relative to NEBD [min]

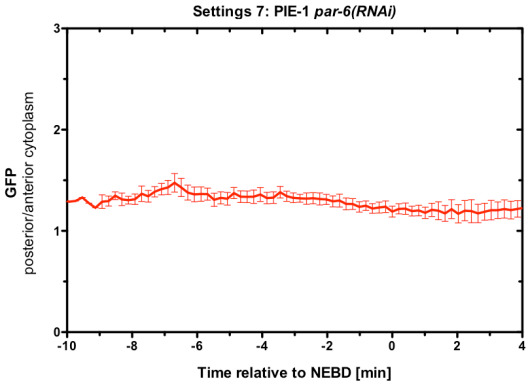
Settings 7: PIE-1 par-6(RNAi)
GFP
posterior/anterior cytoplasm
Time relative to NEBD [min]

6.4.7 Nuclear accumulation

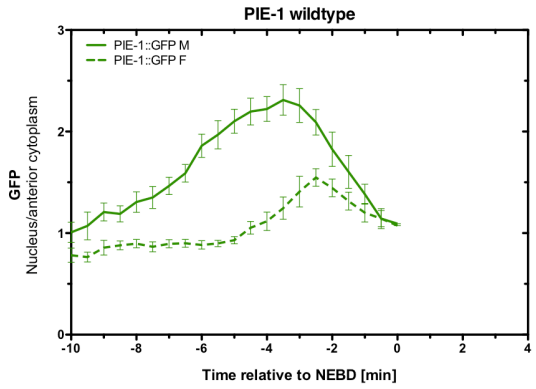

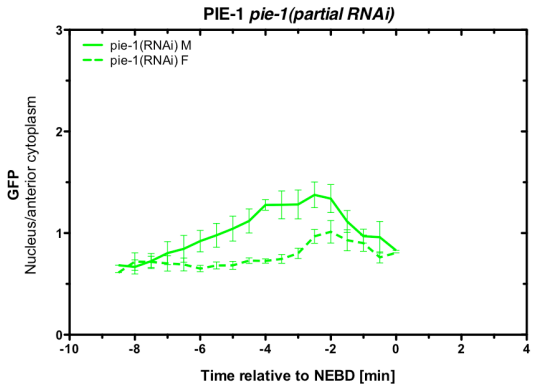

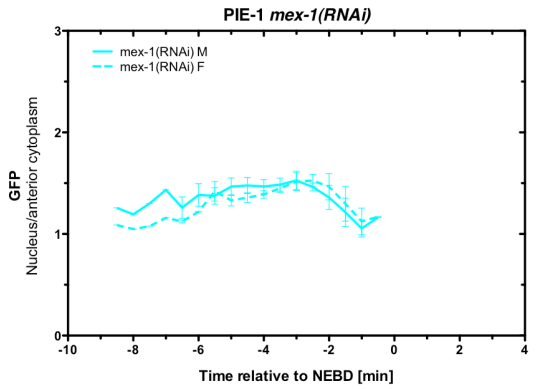

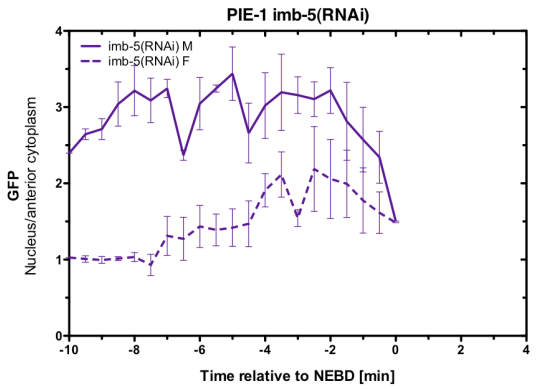

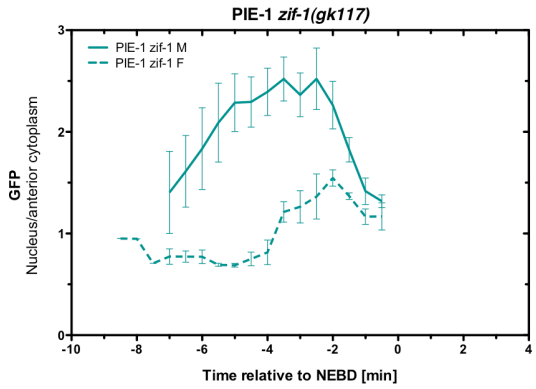

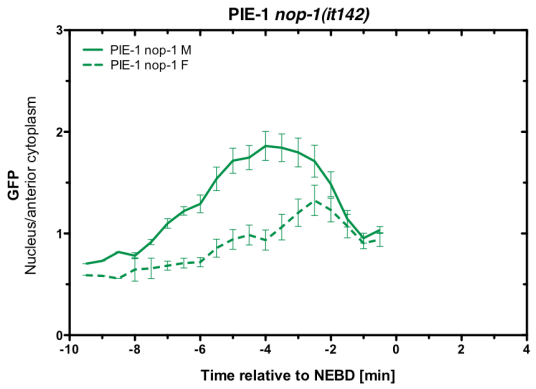

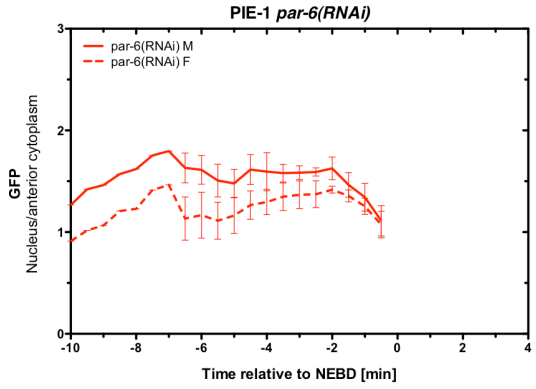

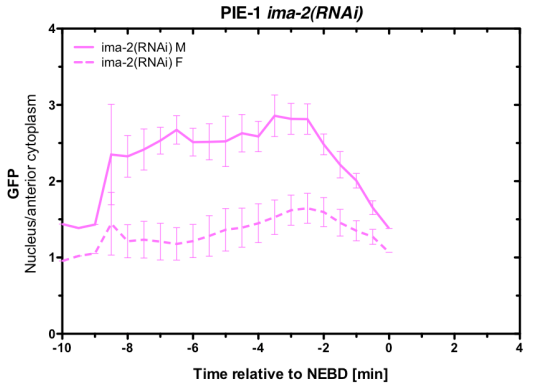

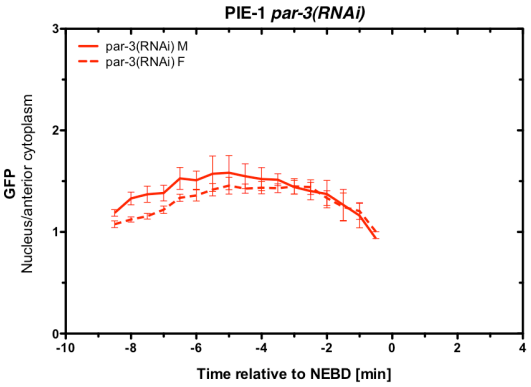
PIE-1 par-3(RNAi)
par-3(RNAi) M
par-3(RNAi) F
GFP
Nucleus/anterior cytoplasm
Time relative to NEBD [min]

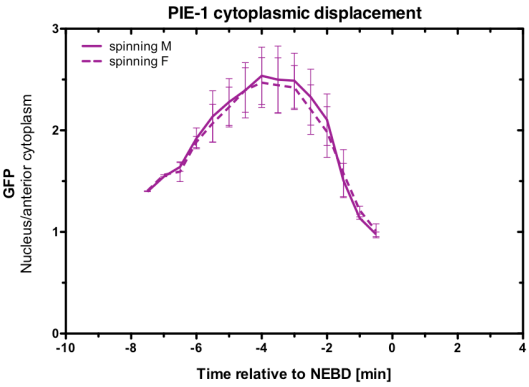
PIE-1 cytoplasmic displacement
spinning M
spinning F
GFP
Nucleus/anterior cytoplasm
Time relative to NEBD [min]

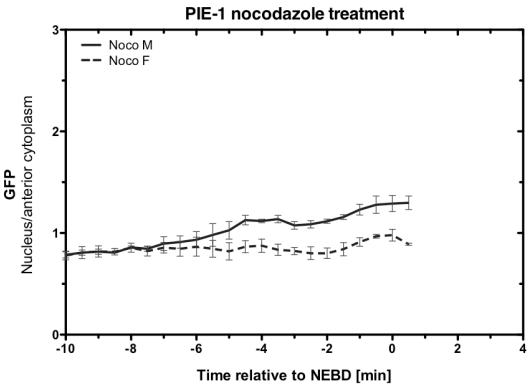
PIE-1 nocodazole treatment
Noco M
Noco F
GFP
Nucleus/anterior cytoplasm
Time relative to NEBD [min]